Sigurdsson, H., Leckie, R.M., Acton, G.D., et al., 1997
Proceedings of the Ocean Drilling Program, Initial Reports, Vol. 165

5. SITE 1000[1]

Shipboard Scientific Party[2]

HOLE 1000A

Position: 16°33.223′N, 79°52.044′W (Nicaraguan Rise)

Date occupied: 0900 hr, 27 January 1996

Date departed: 0330 hr, 29 January 1996

Time on hole: 42.5 hr (1 day, 18 hr, 30 min)

Seafloor depth (drill-pipe measurement from rig floor, mbrf): 927.2

Total depth (drill-pipe measurement from rig floor, mbrf): 1480.4

Distance between rig floor and sea level (m): 11.3

Water depth (drill-pipe measurement from sea level, m): 915.9

Penetration (mbsf): 553.2

Coring totals:

Type: APC; No: 34; Cored: 312.90 m; Recovered: 323.89 m (103.5%)
Type: XCB; No: 25; Cored: 240.30 m; Recovered: 214.39 m (89.2%)
Total: No: 59; Cored: 553.20 m; Recovered: 538.28 m (97.3%)

Formation:

Micritic ooze with foraminifers and nannofossils; micritic nannofossil chalk with foraminifers.

Oldest sediment cored:

Depth (mbsf): 553.2
Nature: Calcareous chalk/limestone with nannofossils
Age: middle Miocene

HOLE 1000B

Position: 16°33.219′N, 79°52.046′W (Nicaraguan Rise)

Date occupied: 0330 hr, 29 January 1996

Date departed: 0315 hr, 1 February 1996

Time on hole: 71.75 hr (2 days, 23 hr, 45 min)

Seafloor depth (drill-pipe measurement from rig floor, mbrf): 927.2

Total depth (drill-pipe measurement from rig floor, mbrf): 1623.1

Distance between rig floor and sea level (m): 11.4

Water depth (drill-pipe measurement from sea level, m): 915.8

Penetration (mbsf): 695.9

Coring totals:

Type: RCB; No: 22; Cored: 211.40 m; Recovered: 142.97 m (67.6%)

Formation:

Limestone with foraminifers and ash layers.

Oldest sediment cored:

Depth (mbsf): 695.9
Nature: Calcareous limestone with foraminifers
Age: early Miocene

Principal results: Site 1000 is located in Pedro Channel, one of a series of channels that dissects the carbonate shelves and isolated carbonate banks that define the east-northeast-trending northern Nicaraguan Rise (NNR). One of our principal objectives at Site 1000 was to reach the top of a carbonate platform and document the onset of the Caribbean Current. Droxler et al. (1991, 1992) have proposed that the NNR was a large carbonate platform during much of the Paleogene that ultimately became segmented because of tectonic activity along the northern Caribbean Plate boundary. The Pedro Channel represents one of the largest segments of the once-contiguous megabank, originally thought to have foundered during middle Miocene time. The carbonate platform proved to be deeper and older than predicted. The thick and continuous 20-m.y. record of pelagic sedimentation cored at Site 1000, however, provides many new insights into the history of Caribbean subthermocline (intermediate) water masses, the segmentation and subsidence history of the NNR, the seismic stratigraphy of the region, and a record of explosive volcanism during the Neogene.

A continuous, fairly homogeneous, and apparently complete lower Miocene–recent section was cored at Site 1000. Hole 1000A was cored with the APC to a depth of 312.9 mbsf (middle Miocene) with 103.5% recovery, and then cored with the XCB to a depth of 553.2 mbsf with 89.2% recovery. Hole 1000A terminated in middle Miocene calcareous limestone with nannofossils after coring mainly periplatform oozes and chalks. Hole 1000B recovered two cores in oozes above 117 mbsf before the hole was drilled ahead to a depth of 503.5 m with the RCB system. Hole 1000B was terminated in lower Miocene limestone at a depth of 695.9 mbsf with recovery averaging 67.6% over the cored interval.

The 696-m-thick sedimentary sequence recovered in two holes at Site 1000 consists dominantly of periplatform sediments and sedimentary rocks, interbedded with volcanic ash layers and intervals of redeposited periplatform/pelagic and neritic carbonate sediments from the slopes and top of adjacent shallow carbonate banks. Two main lithologic units were recognized based mainly on degree of lithification: Unit I comprises mixtures of biogenic and calcareous ooze and chalk, whereas Unit II comprises mixtures of biogenic and calcareous limestone.

Unit I is divided into four subunits: Subunit IA (0.0–50.8 mbsf; recent–upper Pliocene) is characterized by frequent downcore variations in carbonate content and by a turbidite-free sedimentary sequence with only a few rare and thin volcanic ash layers. Subunit IB (50.8–370.5 mbsf; upper Pliocene–upper Miocene) is a thick interval of relatively uniform micritic biogenic ooze, with volcanic ash layers being common throughout, and a few turbidites occurring in the lower half of the subunit. Subunit IC (370.5–486.0 mbsf; upper–middle Miocene) is defined by an interval of lower carbonate content, where detrital clays and quartz reach a maximum for the site. Subunit ID (486.0–513.4 mbsf; middle Miocene) is similar in lithologic characteristics to Subunit IB, although it is turbidite-free.

Unit II is divided into two subunits. Subunit IIA (513.4–591.3 mbsf; middle–lower Miocene) is characterized by relatively high carbonate content. Subunit IIB (591.3–695.9 mbsf; lower Miocene) is characterized by fluctuating carbonate content values and the highest abundance of volcanic ash layers and turbidites of any subunit.

Sedimentation and mass accumulation rates (MARs) decline from values of 37.2 m/m.y. and 3.5–5.0 g/cm^2/k.y. in the upper Miocene to upper Pliocene interval (2.8–9.6 Ma) to an average of 27.3 m/m.y. and 2.4–3.4 g/cm^2/k.y. in the upper Pliocene–Pleistocene interval (0.0–2.8 Ma). A similar pattern was observed at Sites 998 and 999. One notable feature of the Pliocene is the abrupt increase in carbonate MARs at about 4.1–4.2 Ma, which may be related to of the closing of the Central American Seaway.

Lithologic Subunits IC and ID display the highest sedimentation and accumulation rates of the section, averaging 47.0 m/m.y. (4.5–7.5 g/cm^2/k.y.). The most distinctive pattern in this part of the section is the peak in noncar-

[1]Sigurdsson, H., Leckie, R.M., Acton, G.D., et al., 1997. *Proc. ODP, Init. Repts.,* 165: College Station, TX (Ocean Drilling Program).
[2]Shipboard Scientific Party is given in the list preceding the Table of Contents.

bonate MARs associated with the "carbonate crash," a trend also observed at Sites 998 and 999. At Site 1000, this interval is characterized by higher magnetic susceptibility, distinctly lower but highly variable carbonate contents, increased noncarbonate MARs, enrichments of up to 0.8% TOC (in the interval ~360–510 mbsf), and relatively high concentrations of uranium.

Sulfate reduction is more pronounced at Site 1000 than at Sites 998 and 999, with sulfate concentrations approaching zero by 350–400 mbsf (top of the carbonate minimum and hydrocarbon enrichment zones). Paleomagnetic intensities indicate, however, that all but the upper 22.5 m of the section have been severely affected by reduction diagenesis. There are also enrichments of volatile hydrocarbons in the interval from ~400 to 520 mbsf. Migration of hydrocarbons (updip and/or upsection) into the interval of the carbonate minimum is suspected due to the shallow burial and the absence of an anomalously high thermal gradient. In situ generation of thermogenic gases within the hydrocarbon zone is not supported, although bacterial methanogenesis may be a factor for the occurrence of C_1 in this zone given the absence of sulfate at this depth. Increased alkalinity associated with sulfate reduction in the carbonate minimum and hydrocarbon zone may be responsible for the precipitation of carbonate cements along a lithification front represented by the abrupt change from chalk to limestone at about 510 mbsf (lithologic Unit I/II boundary).

Many of the turbidites occurring in Subunit IIB contain redeposited pelagic sediments, but some also contain material derived from the upper reaches or tops of the adjacent carbonate banks. The lower Miocene–lower middle Miocene interval represented by the limestones and interbedded ash layers and turbidites of lithologic Unit II (13.5–20.0 Ma) had an average sedimentation rate of 27.3 m/m.y. with widely varying bulk MARs of 3.5–6.3 g/cm^2/k.y.

The accumulation rate and number of volcanic ash layers (and dispersed ash) during early to middle Miocene time at Site 1000 exhibits a pattern that is remarkably close to that of Site 999, although the magnitudes of these parameters are somewhat higher at the latter site. The combined evidence from Sites 998, 999, and 1000 shows that the Miocene explosive volcanic episode generated a principal fallout axis that trends east from the Central American arc, between Sites 999 and 1000, or very close to the latitude of Site 1000. This is consistent with derivation of the tephra from the ignimbrite-forming volcanism in the Tertiary Igneous Province of Central America. The combined thickness of ash layers observed in the Caribbean sites indicates that this represents one of the major explosive volcanic episodes known. The magnitude of individual eruptive events is on the order of 10^2–10^3 km^3, whereas the fallout of the episode as a whole is certainly in excess of 10^5 and probably greater than 10^6 km^3.

BACKGROUND AND OBJECTIVES

Site 1000 is located on the northern Nicaraguan Rise (NNR), 265 km southwest of Jamaica in 916 m of water (Fig. 1). The NNR extends from Honduras and Nicaragua on the west to the island of Jamaica on the east and is characterized by a series of carbonate shelves and isolated carbonate banks with intervening channels. Site 1000 was cored in the Pedro Channel between Pedro Bank 100 km to the northeast, Rosalind Bank 45 km to the southwest, and Serranilla Bank 50 km to the south (Fig. 2). Site 1000 was cored in the same region where Cesare Emiliani drilled the first long core in 1963 (56.4 m of penetration, 20.7 m of recovered core) as part of his LOCO Project (LOng COres), an early predecessor of the JOIDES Deep Sea Drilling Project (DSDP; Bolli et al., 1968; Emiliani, 1981).

The Pedro Channel is 150 km wide, with maximum depths ranging from 1350 to 1450 m; it is the largest channel crossing the NNR. The tops of the adjacent carbonate banks are submerged 25–45 m below sea level, well within the photic zone. These banks produce a large volume of neritic metastable carbonate sediment (fine-grained biogenic aragonite and magnesian calcite), much of it exported to the deep surroundings of the banks (Zans, 1958; Dolan, 1972; Hallock et al., 1988; Glaser and Droxler, 1991; Triffleman et al., 1992; Schwartz, 1996). Sediments deposited in the intervening seaways, referred to as periplatform sediments or ooze (Schlager and James, 1978), are a mixture of pelagic and bank-derived neritic carbonates, with a minor component of terrigenous sediments brought in by oceanic currents.

The water column at Site 1000, in spite of its relative shallow depth, is just at saturation or slightly oversaturation with respect to aragonite, and is saturated or slightly undersaturated with respect to magnesian calcite (Droxler et al., 1991). In a piston core (CH9204-42) recovered from 3.7 km south of Site 1000 (Fig. 2), Schwartz (1996) demonstrated that variations in the percentage of fine aragonite relative to the total sediment show a strong glacial/interglacial cyclicity (last 0.5 m.y.), with high values during interglacial stages when the bank tops were submerged and low values during glacial stages when the bank tops were exposed (Fig. 7). Similar patterns have been demonstrated in other periplatform environments around the world; for example, in the Bahamas during the late Quaternary (Droxler et al., 1983), in the Maldives (Droxler et al., 1990), in the Walton Basin (Glaser and Droxler, 1993), in New Caledonia (Liu and Cotillon, 1989), and on the Queensland Plateau (Haddad et al., 1993). Variations in the percentage of fine carbonate content relative to the total sediment are also strongly linked to late Quaternary glacial/interglacial cyclicity, with relative low carbonate values occurring during glacial stages (Fig. 7).

Based upon the interpretation of a high-resolution seismic grid and analyses of dredged shallow-water limestones cropping out on the seafloor, the Pedro Channel is interpreted to have formed by the partial foundering of a large carbonate platform, referred to as a megabank, that included the shelves of Honduras and Nicaragua and the island of Jamaica (Droxler et al., 1992). Since its formation, Pedro Channel has been a major pathway for the Caribbean Current and, therefore, for the surface and thermocline return flow of the modern global thermohaline circulation.

A primary objective for Leg 165 was to recover the top of the drowned carbonate bank in the Pedro Channel in order to (1) estimate the timing of the formation of Pedro Channel and, by inference, the initiation of the Caribbean Current; (2) recover a continuous periplatform section overlying the top of the drowned carbonate bank to study the evolution of the Caribbean Current, especially its strengthening through time related to the stepwise closing of the Central American Seaway (Isthmus of Panama) during the Neogene; and (3) recover a complete Neogene sedimentary sequence that will help establish a unique paleoceanographic record in the Caribbean at an intermediate (subthermocline) water depth. Two additional goals introduced during Leg 165 operations were to map the extent and depth range in the water column of the middle/late Miocene carbonate crash further and to determine the spatial distribution and accumulation rate of ash layers from the Miocene volcanic episode. The 20-m.y. periplatform sedimentary section recovered at Site 1000 contains both of these events and appears to be continuous and fairly homogeneous throughout. We also had hoped to core into the drowned carbonate platform, but this goal proved elusive given the time constraints and the underestimated depth to the seismic reflector defining the carbonate platform surface.

SEISMIC STRATIGRAPHY

Site 1000 is located at 16°33.20′N, 79°52.04′W in the Pedro Channel on the NNR, about 45 km east of Rosalind Bank, 50 km north of Serranilla Bank, and 265 km southwest of Jamaica (Fig. 2). The Pedro Channel is flanked by the Cayman Trough to the north, the southern Nicaraguan Rise and Serranilla Bank to the south, the Pedro Bank to the east, and the Rosalind Bank to the west. These three banks, though relatively deeply submerged under 25–45 m of water depth on average, produce large volumes of fine neritic carbonate

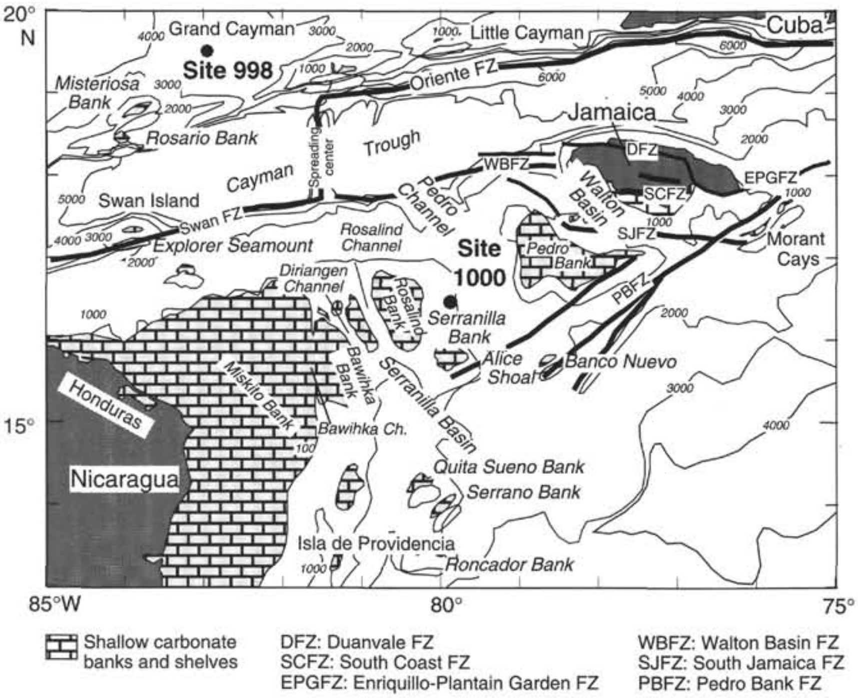

Figure 1. Setting of Site 1000 in the Pedro Channel, a seaway on the northern Nicaraguan Rise (NNR) separating Pedro Bank from Rosalind and Serranilla Banks and the main pathway for the Caribbean Current.

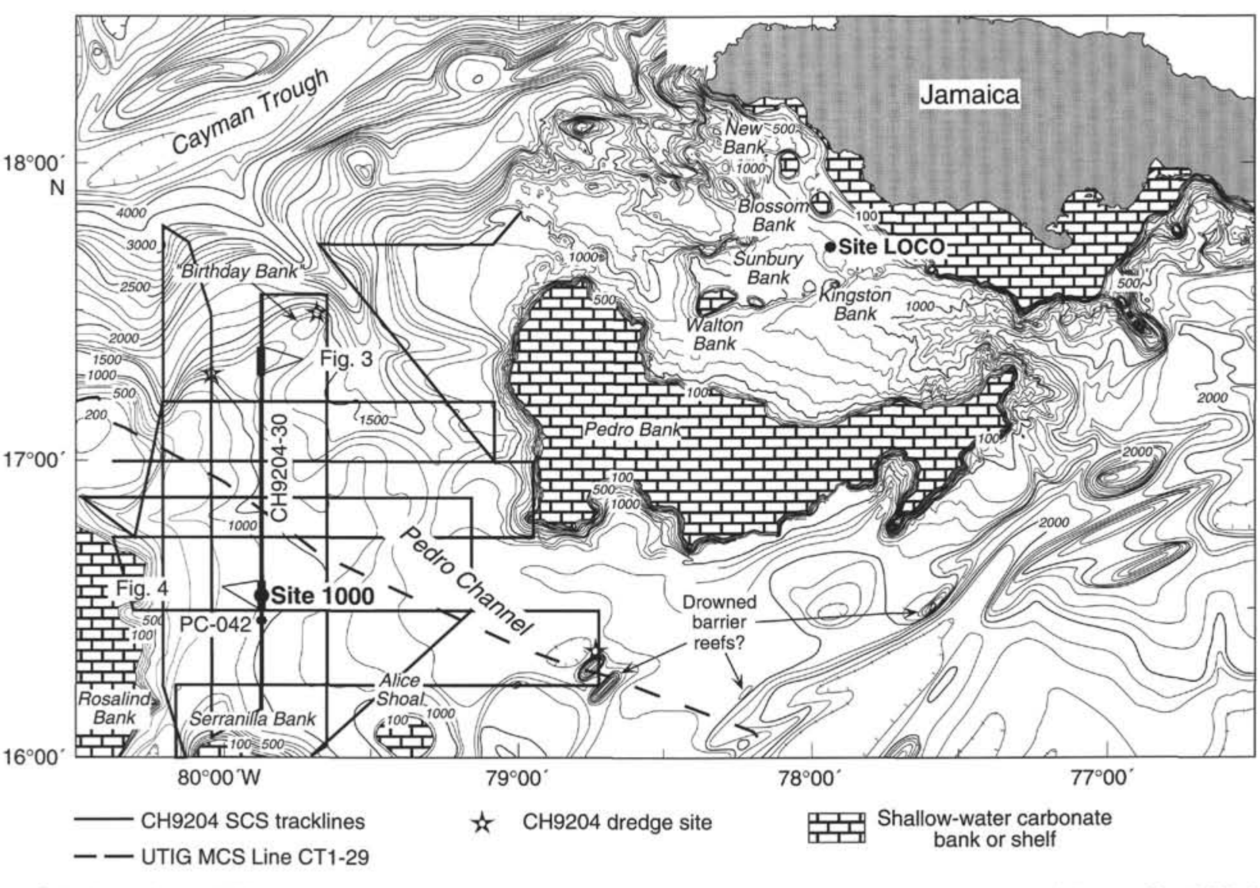

Figure 2. Bathymetric map (100-m contour interval) showing the location of Site 1000 and the major physiographic features of the area. Site 1000 is located on CH9204 SCS Line 30 (solid north-south straight line) and southwest of UTIG MCS Line CT1-29B (dashed line).

sediments when their bank tops are submerged within the photic zone and export them toward their deep surroundings (Zans, 1958; Dolan, 1972; Hallock et al., 1988; Triffleman et al., 1992; Glaser, 1992; Glaser and Droxler, 1991, 1993; Schwartz, 1996). The Pedro Channel, 150 km in width and with maximum depths ranging from 1350 to 1450 m, is the largest and most central seaway on the NNR.

Bathymetry

Examination of the CH9204 3.5-kHz data obtained in the Pedro Channel (see "Explanatory Notes" chapter, this volume) yields new information on topographic features in the Pedro Channel and the Walton Basin. The smooth seafloor topography in previous maps has been replaced in the revised bathymetric map of the Pedro Channel (A.D. Cunningham, unpubl. data) and the Walton Basin (Robinson, 1976) by a somewhat more "blocky," segmented character of the seafloor morphology (Fig. 2). The new map of the Pedro Channel shows two "spurs" that extend from the northern part (Northern Spur) and the eastern slope of the Rosalind Bank (Southern Spur) over 50 km to the northeast into the channel and are interpreted to correspond to two segments of a drowned carbonate bank (Fig. 2). During a recent (end of 1994) limited survey of the Pedro Channel by Hydrosweep on *Maurice Ewing* (see "Explanatory Notes" chapter, this volume), a small drowned bank, called the Birthday Bank, was discovered on the eastern extremity of the Northern Spur (Fig. 2). The small bank is characterized by steep slopes and a tilted top in 900 m of water depth. During the same Hydrosweep survey, an elongated bathymetric feature characterized by a flat top at about 900 m of water depth, interpreted as a drowned barrier reef, was imaged on the southern edge of NNR, just south of the Pedro Channel (Fig. 2). Two similar elongated bathymetric features, already marked in previous bathymetric maps in the same area, are also interpreted as drowned barrier reefs. Moreover, the area north of the Rosalind Bank, a plateau lying in water depths of 225 and 375 m and tilted toward the south, is also interpreted as another segment of a drowned carbonate bank (Hine et al., 1992; Fig. 2). The central portion of the Pedro Channel is dissected by numerous gullies and canyons that merge and eventually drain to the north into the Cayman Trough.

High-Resolution Seismic Reflection Lines

Interpretation of the high-resolution seismic grid acquired in the Pedro Channel suggests that the sub-seafloor of this channel consists of a foundered large carbonate bank, referred to as the "megabank," overlain by a thick periplatform sedimentary cover (Cunningham et al., 1995; Fig. 3). The foundered megabank is evident in most of the seismic lines and is identifiable by high-amplitude, moderate to high continuity, usually subparallel low-frequency reflectors, some of which are folded and faulted by high angle faults. Block faulting and significant erosion of the megabank are the two major factors that have affected the formation of the Pedro Channel. The edge of the megabank appears to have undergone significant erosion in places during the first emplacement of the Caribbean Current. These suspected middle(?) Miocene erosional features may be linked to other middle Miocene erosional events on the central west Florida shelf (Mullins et al., 1980, 1987, 1988), the Straits of Florida (Gomberg, 1974; Mullins and Neumann, 1977, 1979; Austin, Schlager, et al., 1988), and the Blake Plateau (JOIDES, 1965; Popenoe, 1985), and may be explained by the overall strengthening of the Western Boundary Current (Caribbean Current, Loop/Florida Current, and Gulf Stream) in middle to late Miocene times.

A thick sequence of parallel-laminated reflectors, characterized by higher frequency and lower amplitude reflections than from the megabank, covers the foundered megabank, onlaps onto the bank edges, and is interpreted to correspond to a thick sequence of periplatform sediments. The major mode of basin infilling appears to be a combination of pelagic and bank-derived fine sediments with small-scale calcareous turbidites, as during the late Quaternary in the Walton Basin (Bolli et al., 1968; Glaser, 1992; Glaser and Droxler, 1991, 1993) and the Pedro Channel (Schwartz, 1996). Some intervals of the sedimentary basin infill are also expected to be current-winnowed. Only the eastern side of the Pedro Channel shows evidence of megabreccia infilling that characterizes the basin infill in the Rosalind Channel to the west (Hine et al., 1992). Two types of faults have been identified in the Pedro Channel. One set consists of listric normal faults that bottom out within the periplatform cover. The second set penetrates both the megabank and the periplatform sediments. Although some of the faults displace the surface sediments, indicating recent activity, many of the faults terminate within the periplatform cover, indicating inactivity. The location of several major canyons within the Pedro Channel are rooted along these deeper faults.

Dredge Hauls

In several locations within the Pedro Channel, especially along the crest of the Northern Spur in the Pedro Channel, the top of the foundered megabank crops out on the seafloor. This interpretation has been verified by dredging shallow-water fossiliferous reefal limestone blocks along the exposed part of the megabank (Droxler et al., 1992; Cunningham et al., 1995). The dredged limestones consist mostly of corals (*Montastrea costata, Stylophora* cf. *imperatoris,* and *Porites trinitatis;* S.H. Frost, pers. comm., 1992), green algae, and the larger benthic foraminifer *Miogypsina gunteri,* which yields an early Miocene age for these limestones (22–20 Ma; Cole, 1967; Bryan and Huddleston, 1991; E. Robinson, pers. comm., 1992; Robinson, 1994). Based on these dredged neritic limestones, it can be concluded that part of the Northern Spur has undergone a minimum of 900 m of subsidence since the early Miocene. The Birthday Bank on the eastern extremity of the Northern Spur is interpreted to correspond initially to a keep-up bank, which eventually drowned as did several other (barrier?) reefs in the deep area south of the Pedro Bank.

Seismic Stratigraphy

The selection of the Site 1000 location was based on a grid of single-channel seismic (SCS) data (Fig. 2) acquired during a *Cape Hatteras* cruise (CH9204) described in the "Explanatory Notes" chapter (this volume). The site is at a water depth of 916 mbsl and is situated on shotpoint 1495 on the north-trending SCS Line CH9204-30, about 6 km north of the crossing with the SCS Line CH9204-5 (Fig. 4). The line is located approximately 24 km southwest of UTIG multichannel seismic (MCS) Line CT1-29B (Fig. 2).

Examination of SCS Line CH9204-30 around Site 1000 reveals two distinct seismic units (Fig. 4). Seismic Unit A extends from the seafloor at 1235 ms two-way traveltime (TWT) to 1775 ms TWT (Reflector 5). Seismic Unit B extends from 1775 to 2190 ms TWT (Reflector 6) and may be associated with the buried top of the shallow-water carbonate megabank. More precise identification of the base of Unit B at Site 1000 will require a more detailed interpretation of the full high-resolution seismic grid based upon the drilling results of Site 1000 during our post-cruise research, and the integration of our interpretation with existing UTIG and IFP MCS lines in the Pedro Channel.

Seismic Unit A is subdivided into four subunits (A1–A4). Subunit A1 extends from 1235 to 1550 ms TWT (Reflector 2) and is characterized by variably low- to high-amplitude, moderate- to high-frequency, parallel to subparallel, very continuous reflections. Reflector 1 lies within Subunit A1 at 1450 ms TWT and consists of a triplet of very high-amplitude, low-frequency, parallel to subparallel, very continuous reflections. Subunit A2 extends from 1550 to 1600 ms TWT (Reflector 3), and is characterized by very high-frequency, moderate- to high-amplitude, parallel to subparallel, very continuous reflectors.

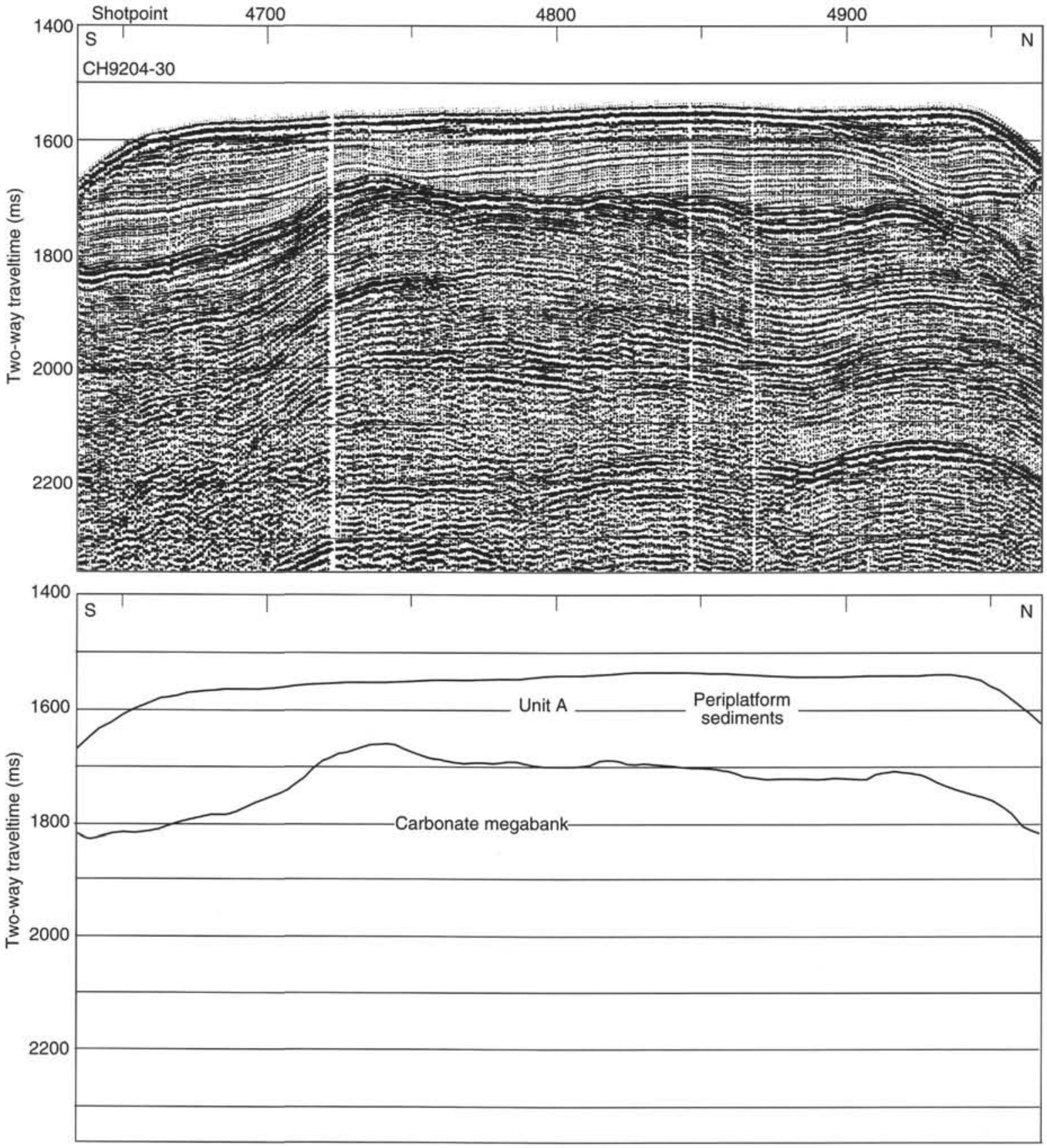

Figure 3. A portion of CH9204 SCS Line 30 over the Northern Spur showing the seismic characters of the megabank and the overlying periplatform sediments, with an interpreted seismic stratigraphic correlation.

Subunit A3 extends from 1600 to 1740 ms TWT (Reflector 4) and contains moderate-amplitude, low-frequency, parallel to subparallel, moderately continuous reflections. Subunit A4 extends from 1740 to 1775 ms TWT (Reflector 5), and consists of very high-frequency, moderate- to high-amplitude, parallel to subparallel, highly continuous reflections.

Seismic Unit B extends from 1775 to 2190 ms TWT (Reflector 6). This reflector is perhaps associated with the buried top of a shallow-water carbonate megabank. It is distinguished from Unit A mainly by its lack of high-frequency reflections. It also consists of several sets of very high-amplitude, parallel to subparallel, continuous reflections, separated by zones of lower amplitude, less continuous reflections. Unlike seismic Unit A, the amplitude of the reflections changes laterally. The reflection characteristics of Unit B are very similar to the characteristics of the seismic unit cropping out on the seafloor along the crest of the Northern Spur in the Pedro Channel, where early Miocene neritic reefal limestones were dredged (Fig. 3). For this reason, Droxler et al. (1991, 1992) predicted before drilling began that the top of the megabank would correspond to Reflector 5, which marks the top of seismic Unit B. Drilling at Site 1000 disproved this interpretation.

Velocity analysis of MCS data from Line CT1-29B provided estimates of interval velocities for seismic units at Site 1000 (Fig. 2). Although MCS Line CT1-29B does not cross Site 1000, estimates of

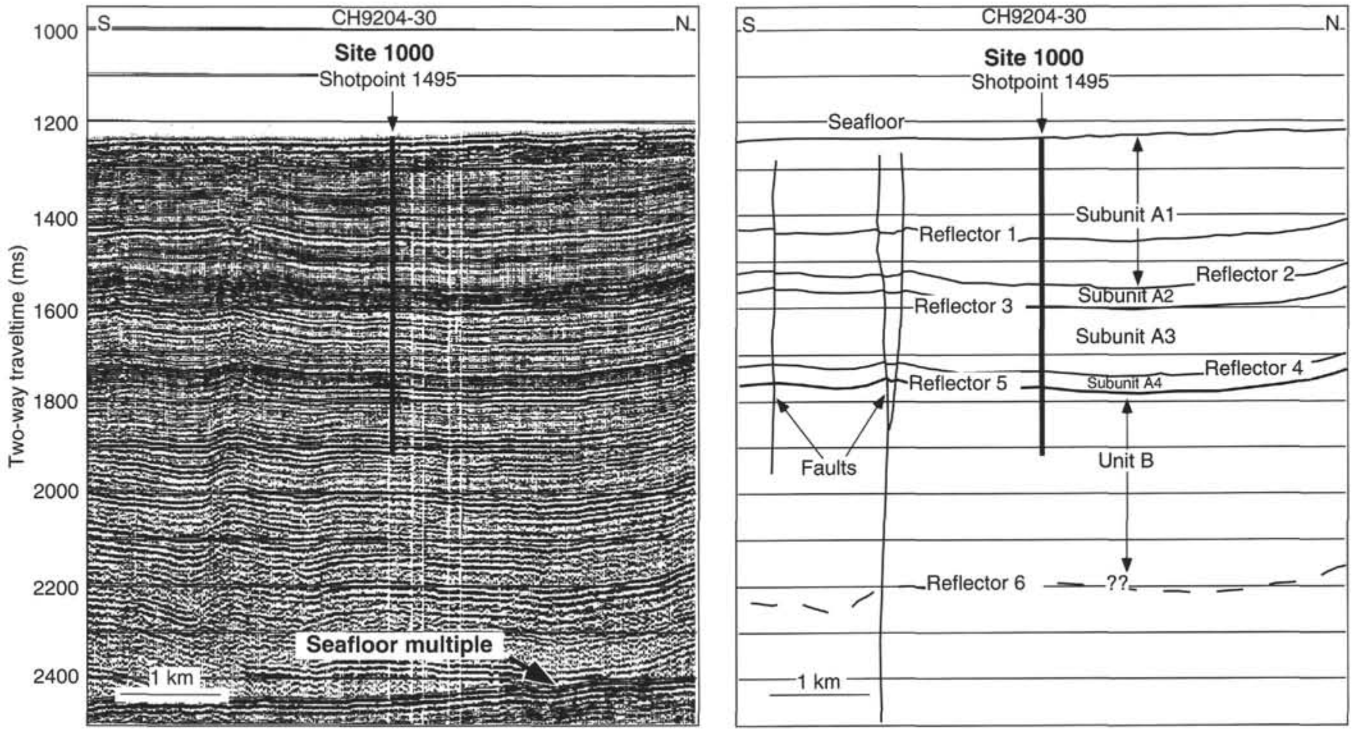

Figure 4. A portion of CH9204 SCS Line 30 showing the location of Site 1000 (shotpoint 1495) and the interpreted seismic stratigraphic correlation.

representative interval velocities were made for the different seismic stratigraphic units based on their lateral correlation. These estimates indicate an interval velocity of approximately 1950 m/s for all of Unit A, which would place the base of Unit A at about 526 mbsf. This depth is in close agreement with changes in lithology from chalk to limestone (see "Lithostratigraphy" section, this chapter) and a major change in many physical properties (see "Physical Properties" section, this chapter). An interval velocity of 2750 m/s is estimated for Unit B, whereas an interval velocity of about 4150 m/s is estimated for the interval below Reflector 6. Coring results at Site 1000 now suggest that the top of the drowned carbonate megabank may correspond to Reflector 6, or perhaps to a set of reflectors within Unit B.

OPERATIONS

Before heading to Site 1000 from Site 999, the ship was docked in Kingston, Jamaica, to take on board a Honduran observer and a scientist from the JOIDES office in Cardiff, to load propulsion motors and freight, and to disembark the Colombian observer/scientist and a Japanese scientist who left for medical reasons. The 550-nmi transit from Kingston to Site 1000 was covered at an average speed of 9.6 kt.

Hole 1000A

Hole 1000A was cored with the APC and XCB systems. Owing to the thick section of unconsolidated and poorly indurated sediments, we were able to recover 34 APC cores, which gave a 103.5% recovery for the interval from 0.0 to 312.9 mbsf. Two cores (165-1000A-10H and 13H) were highly disturbed upon recovery, possibly because the flapper core catcher may not have fully opened, thus forcing the core material to flow past the flapper. These intervals were later recovered successfully with the RCB system in Hole 1000B. The XCB system performed well, with high rates of penetration (ROP) and high recovery (86.5 m/hr with 100% recovery to 400 mbsf; 72.2 m/hr with 100.3% recovery to 500 mbsf; and 49.4 m/hr with 98.6% recovery to 525 mbsf) until a depth of 524 mbsf (Core 165-1000A-56X). Owing to poor recovery and a slow ROP on the following three cores, drilling was halted in Hole 1000A. The site is located on what is considered to be a continental rise. In cooperation with the Pollution Prevention and Safety Panel guidelines, the hole was therefore filled with weighted mud and then cemented with a 60-m-long plug placed in an interval extending from 400 to 340 mbsf.

Hole 1000B

Hole 1000B was spudded about 30 m to the southwest of Hole 1000A with the RCB system. The hole was drilled ahead to 79.3 mbsf and then Core 165-1000B-1R was recovered in roughly the same interval as the disturbed Core 165-1000A-10H. We then drilled ahead to 117.3 mbsf and recovered Core 165-1000B-2R in roughly the same interval as the disturbed Core 165-1000A-13H. The hole was then drilled ahead to 503.5 mbsf where continuous RCB coring was initiated. Core 165-1000B-3R had zero recovery, possibly because of an excessive circulation rate. Good recovery (89%) was achieved on the next core. Overall recovery for Hole 1000B averaged 67.2% (Table 1). Coring ceased at a depth of 695.9 mbsf owing to time constraints. The hole was prepared for logging by circulating a mud pill and conducting a wiper trip. After logging operations were completed (see "Downhole Measurements" section, this chapter), Hole 1000B was also filled with weighted mud and then plugged with cement.

LITHOSTRATIGRAPHY

The 695-m-thick sedimentary sequence recovered in two holes at Site 1000 ranges in age from early Miocene to recent and consists dominantly of periplatform sediments and sedimentary rocks, inter-

Table 1. Coring summary, Site 1000.

Core no.	Date (Jan. 1996)	Time (UTC)	Depth (mbsf)	Cored (m)	Recovered (m)	Recovery (%)
165-1000A-						
1H	27	1615	0.0–3.3	3.3	3.40	103..0
2H	27	1645	3.3–12.8	9.5	9.60	101.0
3H	27	1715	12.8–22.3	9.5	9.46	99.6
4H	27	1740	22.3–31.8	9.5	9.71	102.0
5H	27	1810	31.8–41.3	9.5	9.55	100.0
6H	27	1840	41.3–50.8	9.5	9.87	104.0
7H	27	1900	50.8–60.3	9.5	9.72	102.0
8H	27	1925	60.3–69.8	9.5	9.94	104.0
9H	27	1950	69.8–79.3	9.5	9.82	103.0
10H	27	2015	79.3–88.8	9.5	8.99	94.6
11H	27	2045	88.8–98.3	9.5	9.65	101.0
12H	27	2135	98.3–107.8	9.5	9.33	98.2
13H	27	2215	107.8–117.3	9.5	8.80	92.6
14H	27	2240	117.3–126.8	9.5	10.02	105.5
15H	27	2325	126.8–136.3	9.5	9.84	103.0
16H	28	0010	136.3–145.8	9.5	10.02	105.5
17H	28	0050	145.8–155.3	9.5	9.93	104.0
18H	28	0120	155.3–164.8	9.5	10.01	105.3
19H	28	0145	164.8–174.3	9.5	9.95	105.0
20H	28	0210	174.3–183.8	9.5	10.13	106.6
21H	28	0245	183.8–193.3	9.5	9.95	105.0
22H	28	0315	193.3–202.8	9.5	10.21	107.5
23H	28	0400	202.8–212.3	9.5	10.08	106.1
24H	28	0420	212.3–221.8	9.5	10.13	106.6
25H	28	0455	221.8–231.3	9.5	10.12	106.5
26H	28	0520	231.3–240.8	9.5	10.15	106.8
27H	28	0550	240.8–250.3	9.5	9.98	105.0
28H	28	0620	250.3–259.8	9.5	10.04	105.7
29H	28	0650	259.8–269.3	9.5	9.92	104.0
30H	28	0720	269.3–278.8	9.5	9.97	105.0
31H	28	0745	278.8–288.3	9.5	9.96	105.0
32H	28	0845	288.3–297.8	9.5	10.04	105.7
33H	28	0915	297.8–307.3	9.5	9.97	105.0
34H	28	0945	307.3–312.9	5.6	5.62	100.0
35X	28	1100	312.9–322.5	9.6	9.73	101.0
36X	28	1145	322.5–332.1	9.6	9.48	98.7
37X	28	1205	332.1–341.7	9.6	9.79	102.0
38X	28	1230	341.7–351.3	9.6	9.34	97.3
39X	28	1300	351.3–360.9	9.6	9.74	101.0
40X	28	1320	360.9–370.5	9.6	9.79	102.0
41X	28	1345	370.5–380.1	9.6	9.30	96.9
42X	28	1415	380.1–389.7	9.6	9.73	101.0
43X	28	1445	389.7–399.4	9.7	9.84	101.0
44X	28	1515	399.4–409.0	9.6	9.77	102.0
45X	28	1545	409.0–418.6	9.6	9.67	101.0
46X	28	1700	418.6–428.3	9.7	9.70	100.0
47X	28	1740	428.3–437.9	9.6	9.65	100.0
48X	28	1815	437.9–447.5	9.6	9.84	102.0
49X	28	1845	447.5–457.1	9.6	9.75	101.0
50X	28	1915	457.1–466.7	9.6	9.34	97.3
51X	28	1940	466.7–476.3	9.6	9.91	103.0
52X	28	2030	476.3–486.0	9.7	9.41	97.0
53X	28	2100	486.0–495.6	9.6	9.72	101.0
54X	28	2130	495.6–505.2	9.6	9.18	95.6
55X	28	2205	505.2–514.8	9.6	8.88	92.5
56X	28	2300	514.8–524.4	9.6	8.39	87.4
57X	29	0030	524.4–534.0	9.6	0.34	3.5
58X	29	0200	534.0–543.7	9.7	2.65	27.3
59X	29	0340	543.7–553.2	9.5	1.46	15.3
Coring totals				553.2	538.28	97.3
165-1000B-						
******Drilled from 0.0 to 79.3 mbsf******						
1R	29	1330	79.3–88.8	9.5	8.51	89.6
******Drilled from 88.8 to 107.8 mbsf******						
2R	29	1415	107.8–117.3	9.5	8.05	84.7
******Drilled from 117.3 to 503.5 mbsf******						
3R	30	0005	503.5–513.2	9.7	0.00	0.0
4R	30	0115	513.2–522.8	9.6	8.52	88.7
5R	30	0240	522.8–532.4	9.6	6.77	70.5
6R	30	0355	532.4–541.9	9.5	9.97	105.0
7R	30	0505	541.9–551.6	9.7	8.88	91.5
8R	30	0600	551.6–561.2	9.6	7.34	76.4
9R	30	0645	561.2–570.7	9.5	2.51	26.4
10R	30	0800	570.7–580.4	9.7	1.46	15.0
11R	30	0915	580.4–590.0	9.6	6.96	72.5
12R	30	1020	590.0–599.7	9.7	8.94	92.1
13R	30	1120	599.7–609.3	9.6	7.04	73.3
14R	30	1220	609.3–618.9	9.6	5.20	54.1
15R	30	1330	618.9–628.6	9.7	8.82	90.9
16R	30	1440	628.6–638.2	9.6	8.56	89.1
17R	30	1545	638.2–647.8	9.6	7.84	81.6
18R	30	1700	647.8–657.4	9.6	5.88	61.2
19R	30	1815	657.4–667.0	9.6	5.15	53.6
20R	30	2030	667.0–676.6	9.6	2.36	24.6
21R	30	2230	676.6–686.2	9.6	7.52	78.3
22R	30	2350	686.2–695.9	9.7	5.87	60.5
Coring totals				211.4	142.15	67.2
Drilled				484.5		
Total				695.9		

Note: An expanded version of this coring summary table that includes lengths and depths of sections, location of whole-round samples, and comments on sampling disturbance is included on CD-ROM in the back pocket of this volume.

bedded with volcanic ash layers and intervals of redeposited periplatform/pelagic and neritic carbonate sediments from the slopes and tops of adjacent shallow carbonate banks. Two holes (1000A and 1000B) were drilled at Site 1000. The correlation between the holes is within 70 cm, as illustrated by the occurrence of the same turbidite layer at 78.9 mbsf in Hole 1000A and 79.6 mbsf in Hole 1000B. The excellent overlap of the color reflectance records within the interval of common cored sediment between 513 and 525 mbsf in both holes is another good illustration of the splicing between the two holes (Fig. 5).

The deposition of sediments at Site 1000, dominantly by settling of particles through the water column, shows a persistent fine-grained component in the form of bank-derived, fine (a few to 10–20 µm) aragonite needles and other carbonate particles, observed by smear-slide analyses and referred to here as micrite (sensu lato). The occurrence of aragonite as deep as 464 mbsf confirms that input of fine-grained, bank-derived sediments has been a component of the sediments in Pedro Channel at least since the middle Miocene. Downcore high-resolution measurements (5-cm spacing) of color reflectance (see Appendix tables on CD-ROM, back pocket, this volume) and magnetic susceptibility, in addition to carbonate content and sedimentological observations (percentages of minerals in smear slides, depositional textures, sedimentary structures, and XRD bulk rock analyses), form the basis for dividing the recovered sequence into two main lithologic units (I and II) and six subunits (IA, IB, IC, ID, IIA, and IIB; Fig. 6).

Description of Lithologic Units

Unit I

Intervals: Core 165-1000A-1H through Section 165-1000A-55X-6, 70 cm; Cores 165-1000B-1R and -2R
Age: recent to middle Miocene
Depth: 0.0–513.4 mbsf, Hole 1000A; 79.3–87.7 mbsf, 107.8–115.8 mbsf, Hole 1000B

Unit I contains 513.4 m of sediments, consisting mainly of nannofossil and micritic ooze and chalks to clayey micritic chalks, or periplatform ooze and chalks with variations in the proportions of foraminifers, micrite, and clays. The major lithologies occur as medium- to thick-bedded, homogenous units that are typically separated by gradational contacts. Distinctive thin layers that are interbedded with the major lithologies include volcanic ash layers and redeposited graded beds of foraminiferal sands. The former are produced by eolian transport of material to the site from explosive volcanic eruptions, whereas the latter are interpreted as sediments redeposited by gravity flows.

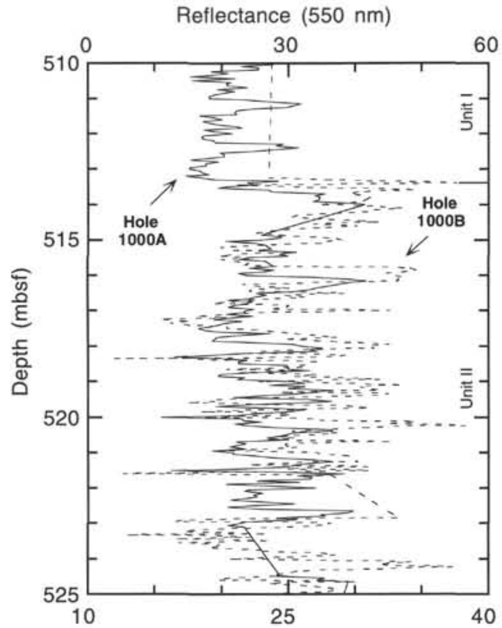

Figure 5. Overlap of color reflectance data within the interval of cored sediment common to Holes 1000A and 1000B illustrates the excellent correlation between the two holes.

Unit I is divided into four subunits based on variations in carbonate content, magnetic susceptibility, and color reflectance data (Fig. 6). Subunit IA is characterized by frequent downcore variations in carbonate content, most likely linked to Pleistocene glacial-interglacial cycles (Figs. 6, 7) and by a turbidite-free sedimentary sequence with only a few rare and thin volcanic ash layers. Subunit IB is a thick interval of relatively uniform lithology, with some small and gradual variations in carbonate content. Volcanic ash layers are common throughout this subunit, and some redeposited foraminiferal sands occur in the lower half of the subunit. Subunit IC is defined by an interval of lower carbonate content, where detrital clays and quartz reach a maximum for the site. In this subunit, the carbonate content gradually decreases up the hole to a minimum at 380 mbsf, before displaying a sudden carbonate increase. This interval is characterized by a pronounced carbonate minimum and appears to be synchronous with the carbonate crash already recognized at Sites 998 and 999 (see discussion below). Subunit ID is similar in characteristics to Subunit IB. However, it is turbidite-free and the occurrence of volcanic ash layers reaches a minimum.

Subunit IA

Intervals: Cores 165-1000A-1H through 6H
Age: recent to late Pliocene
Depth: 0.0–50.8 mbsf, Hole 1000A

Sediments of Subunit IA consist predominantly of light gray micritic ooze with foraminifers and nannofossils, micritic ooze with nannofossils and pteropods, nannofossil micritic ooze with pteropods and foraminifers, nannofossil ooze with foraminifers, micritic nannofossil ooze with foraminifers, micritic foraminiferal ooze, and foraminiferal ooze with nannofossils and micrite. Using a more general term, the sediments in Subunit IA can be referred to as periplatform ooze.

Contacts between the major lithologies are gradational and marked by changes in grain size that reflect variations in the abundance of foraminifers or pteropods and in the proportion of bank-derived fine carbonate particles or micrite. Sediment texture is generally homogenous with moderate bioturbation. Most cores contain common disseminated pyrite and local pyrite concentrations within burrows, giving the core surface a mottled appearance. In addition, the core surface exhibits various shades of dark gray to purple gray in the vicinity of burrows. Some sections in Core 165-1000A-3H contain faint green horizontal color banding with laminae usually less than 1 mm thick.

The major components of Subunit IA are abundant micrite, nannofossils, foraminifers, and pteropods. Aragonite, calcite (<4 mol% of $MgCO_3$), magnesian calcite (>4 mol% of $MgCO_3$), and dolomite, the usual suite of carbonate minerals observed in periplatform ooze, have been identified by XRD bulk-rock analyses (Table 2; Fig. 8). Magnesian calcite is present only within Samples 165-1000A-1H-2, 80–81 cm, and 3H-2, 21–22 cm, from the upper part of Subunit IA, where it is associated with relatively high abundances of aragonite and relatively low abundances of calcite. As a comparison, maximum values of fine magnesian calcite content relative to the bulk sediment in piston Core CH9204-42 range from 14% to 16% in interglacial Stages 5 and 7 and minimum values of 3% to 4% in the middle of Stage 11 (0.44 Ma; Schwartz, 1996). Dolomite is present within all of the intervals sampled, although in relatively small quantities. Minor terrigenous/volcanic constituents include quartz, feldspar, clay minerals, and volcanic glass shards. XRD analyses indicate that the major clay minerals are most likely smectite, kaolinite, and chlorite. The relative abundances of these clay minerals are low. Pyrite is a ubiquitous minor component throughout the subunit and occurs as silt-sized, irregular-shaped grains.

The carbonate content of sediments in Subunit IA ranges from 66% to 90%, with significant variations occurring from core to core (Fig. 6). When compared with the $CaCO_3$ and aragonite variations, in addition to the planktonic oxygen isotope record in nearby piston Core CH9204-42 (J.P. Schwartz, unpubl. data, 1996; see Fig. 2), the cyclical variations of magnetic susceptibility are suggested to be related to cyclic changes of detrital noncarbonate components tied to Quaternary glacial-interglacial climatic fluctuations. A preliminary stratigraphic interpretation using the shipboard nannofossil and paleomagnetic stratigraphies in association with variations in magnetic susceptibility has identified 23 interglacial and glacial stages in the top 25 m of Hole 1000A. The disappearance of *Pseudoemiliania lacunosa* at 13.9 mbsf within Stage 12, the Brunhes/Matuyama boundary at 20.3 mbsf within Stage 19, and the disappearance of *Reticulofenestra asanoi* at 25.05 mbsf within Stage 23 strengthen this preliminary interpretation of the top 25 m of Hole 1000A, based upon the magnetic susceptibility (Fig. 7).

Subunit IB

Intervals: Cores 165-1000A-7H through 40X; Cores 165-1000B-1R and 2R
Age: late Pliocene to late Miocene
Depth: 50.8–370.5 mbsf, Hole 1000A; 79.3–87.7 mbsf, 107.8–115.8 mbsf, Hole 1000B

Subunit IB is distinguished from Subunit IC on the basis of reduced carbonate content variability, higher overall total carbonate content, higher values in color reflectance data, and lower magnetic susceptibility. Sediments in the upper two thirds of Subunit IB, above Core 165-1000A-34X, consist predominantly of light gray to gray, medium- to thick-bedded micritic nannofossil ooze, micritic foraminiferal ooze with nannofossils, micritic nannofossil ooze with foraminifers, and foraminiferal micritic ooze with nannofossils. In the lower third of Subunit IB, there is a subtle transition in lithification to light gray micritic chalk with nannofossils and foraminifers, micritic chalk with clay and foraminifers, and micritic nannofossil chalk. The contacts between major lithologies are in most cases gradational and defined by differences in sediment texture that are controlled by variations in the proportions of foraminifers. The major components of Subunit IB are abundant nannofossils, foraminifers, and micrite, interpreted to reflect mostly bank-derived, fine carbonate particles. Based upon XRD bulk mineral analyses, calcite is a major compo-

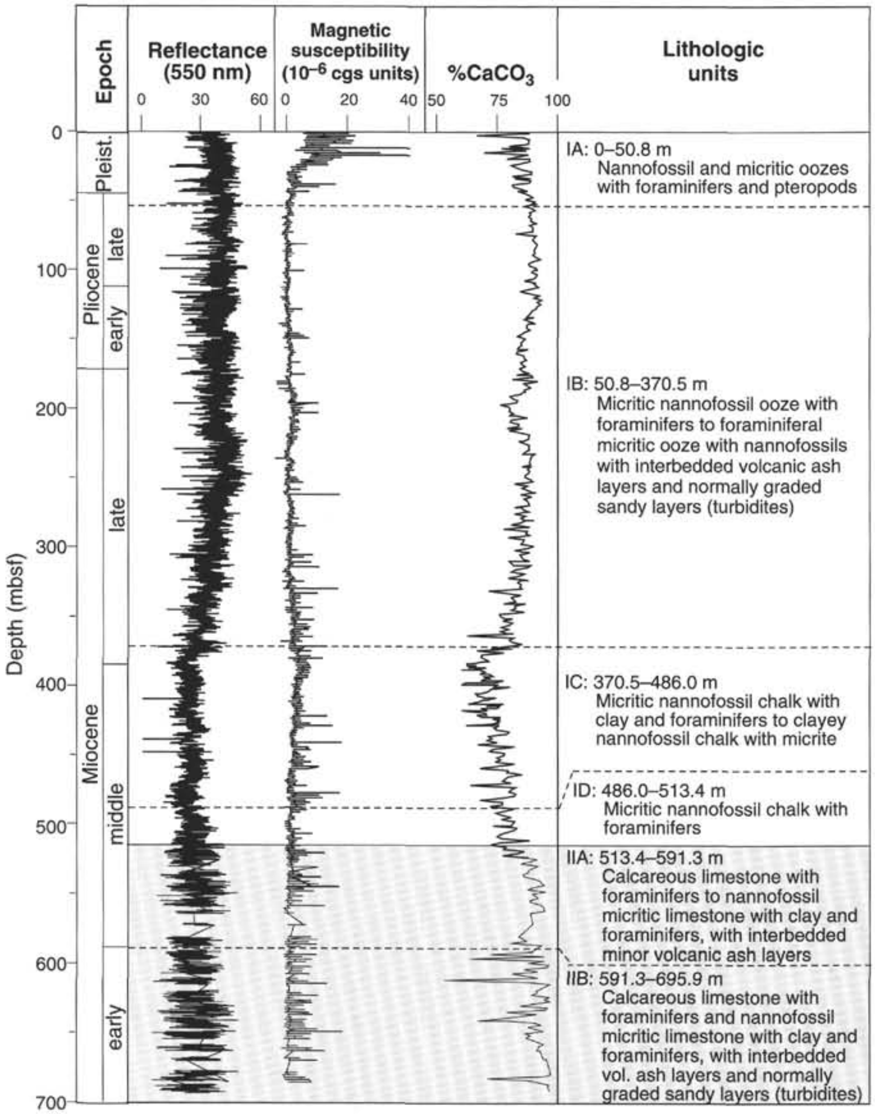

Figure 6. Lithologic units of Site 1000 (Holes 1000A and 1000B) and their relationship to downcore variations in color reflectance, magnetic susceptibility, and %CaCO$_3$.

nent and dolomite is a minor component throughout Subunit IB. Aragonite is clearly observed across two intervals (165-1000A-7H-3 through 15H-4, 54–132 mbsf, and 165-1000A-29H-1 through 39X-3, 260–355 mbsf), but it is absent within the middle part of Subunit IB. Traces of magnesian calcite are detected below 260 mbsf (See Table 2; Fig. 8). The absence of aragonite between 132 and 260 mbsf in the early Pliocene and late Miocene coincides with two intervals of reduced carbonate content (see below). Quartz is present in only relatively minor quantities and in slightly lower amounts than in either Subunits IA or IC. The relative abundance of clay minerals declines slightly below the Subunit IA/IB boundary, and thereafter very low quantities of clay minerals are intermittently present throughout the subunit, most likely paralleling the decline in quartz abundance (Table 2; Fig. 8). Clinoptilolite occurs within and below Core 165-1000A-35X and down into Subunit IC (318–355 mbsf).

Sediment texture within Subunit IB is generally homogenous, with moderate bioturbation. Most cores contain abundant disseminated pyrite and burrows are often infilled with pyrite, giving the core surface a mottled appearance. In addition, the core surface exhibits various shades of dark gray to purple gray in the vicinity of burrows.

Volcanic ash layers form a minor component of Subunit IB and increase in abundance downcore within the unit (see "Igneous Petrology and Volcanology" section, this chapter). The layers are typically thin bedded and dark gray to black; they have sharp bases and bioturbated tops, and they are normally graded (Fig. 9). Most of the layers have suffered extensive alteration, with volcanic glass being converted to smectitic clay and with secondary precipitation of pyrite. At the base of the layers, there are usually less than 10% phenocryst minerals such as feldspar, biotite, or amphibole. However, layers with fresh, clear silicic glass shards occasionally occur.

Coarse foraminiferal sands and silts are a minor component and occur as thin- to medium-bedded, gray to slightly brownish gray layers in the lower half of Subunit IB, beginning at about 245 mbsf downcore (Fig. 10). The layers typically have sharp bases and bioturbated tops, and they exhibit normal grading. Many show parallel and cross-laminations overlying a massive base (Fig. 11). They are interpreted as periplatform sediment redeposited by gravity flows from depths shallower than Site 1000 and are referred to as turbidite layers. The coarse-sized particles appear to be primarily pelagic in origin. A maximum in the frequency of the turbidites (six layers per core, corresponding to a cumulative turbidite thickness of 28 cm per core normalized to core recovery or 3% of the total sediment thickness for the core with the maximum number of turbidite layers) is observed at about 340 mbsf (Fig. 10).

Carbonate contents in Subunit IB range from 77% to 93% and follow the trend of color reflectance and magnetic susceptibility records

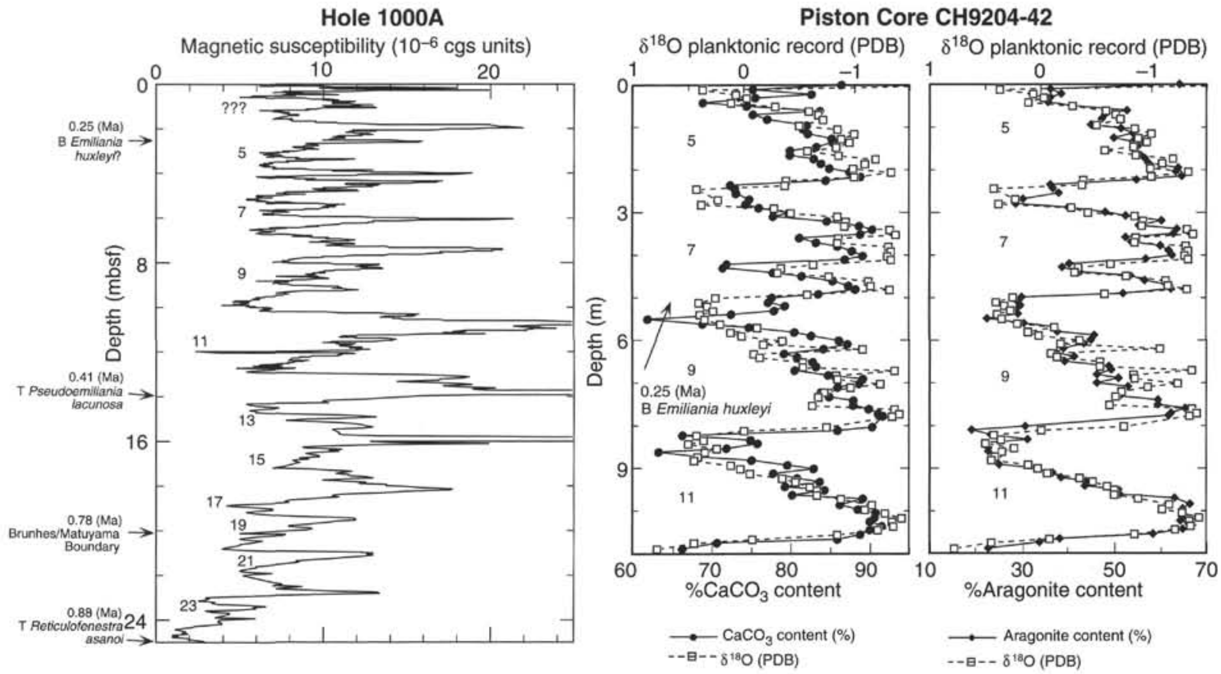

Figure 7. Variations of magnetic susceptibility recorded in the top 25 m of Hole 1000A (Subunit IA). When compared with $CaCO_3$, aragonite, and planktonic $\delta^{18}O$ isotope records from nearby piston Core CH9204-42 (Schwartz, 1996), 23 glacial/interglacial cycles can be tentatively identified at Hole 1000A. This is consistent with the shipboard nannofossil and paleomagnetic stratigraphy.

Table 2. Bulk-rock XRD analyses for Hole 1000A.

			Mineralogy											
										Clays				
Lithologic subunit	Core, section, interval (cm)	Depth (mbsf)	Calcite	High-Mg calcite	Aragonite	Dolomite	Quartz	Feldspar	Zeolites (clinoptilolite?)	Presence/ absence	Chlorite	Kaolinite	Illite	Smectite
IA	1H-2, 80–81	2.30	P	P	P	P	P	Tr		Tr				
	3H-2, 21–22	14.25	P	P	P	P	P			P	Tr	Tr		Tr
	5H-3, 71–73	36.51	P		P	P	P	Tr		P	Tr	Tr		Tr
	6H-3, 70–72	46.00	P		P	P	P			Tr				
IB	7H-3, 69–71	64.49	P		P	P	P	Tr?		Tr				
	9H-3, 119–121	73.99	P		P	P	Tr	Tr?		Tr				
	11H-2, 22–23	90.52	P		P	P	Tr	Tr?						
	14H-1, 123–126	118.53	P		P	P	Tr	Tr?						
	16H-4, 70–71	132.00	P		Tr	Tr?	Tr							
	17H-1, 40–41	146.20	P			P	Tr	Tr?		Tr				
	19H-3, 99–100	168.79	P				Tr							
	21H-5, 20–21	190.00	P			Tr?	P			Tr				
	23H-5, 121–123	210.01	P			P	P			Tr				
	25H-3, 89–91	226.69	P			P	Tr		Tr					
	26H-1, 60–61	231.90	P			Tr?	Tr							
	29H-1, 60–61	260.40	P	Tr?	Tr		Tr			Tr				
	32H-1, 60–61	288.90	P		P	Tr?	Tr			Tr				
	36X-4, 110–112	318.50	P	Tr?	P	P	P		P	Tr?			Tr?	
	37X-1, 60–61	332.70	P	Tr?	Tr?	P	Tr		P					
	39X-3, 70–71	366.00	P		P		P		Tr	Tr				
IC	42X-1, 57–58	380.67	P	Tr?	Tr		P		Tr	Tr			Tr?	
	42X-3, 61–62	383.71	P	Tr?	P		P		Tr	Tr				
	42X-5, 56–59	386.66	P	Tr?	P		P		Tr	Tr				
	43X-1, 57–58	390.27	P	Tr?	Tr	P	P		Tr	Tr				
	43X-3, 58–59	393.28	P	Tr?	P	P	P		Tr	Tr	Tr?	Tr?		
	43X-5, 60–61	396.30	P	Tr?	P	P	P		Tr	Tr				
	44X-1, 57–59	399.97	P	Tr?	Tr	P	Tr		Tr	Tr				
	44X-4, 57–59	404.47	P	Tr?	P	Tr?	P		Tr	Tr				
	45X-5, 93–94	416.93	P	Tr?	P		P		P	Tr				
	46X-1, 68–69	419.28	P	Tr?	P		P		P	P				

Note: P = present, Tr = trace quantities, and Tr? = presence of mineral uncertain.

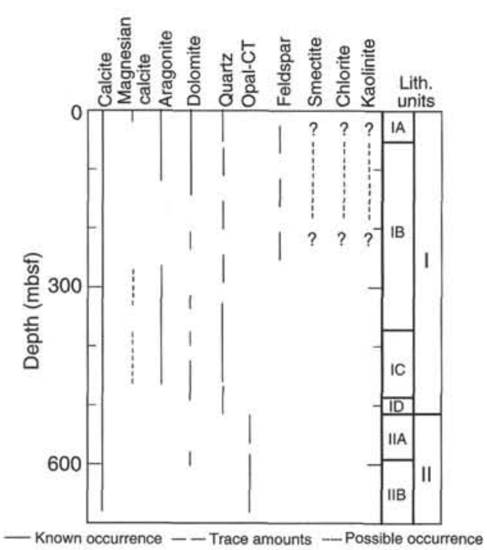

Figure 8. Downcore variations of major minerals in sediments from Site 1000 based on XRD bulk sediment analyses.

(Fig. 6). The subunit is distinguished from Subunit IA by broad wavelength and low-amplitude variability in the carbonate record. Two intervals of lower carbonate content, lower color reflectance, and high magnetic susceptibility occur between 130 and 160 mbsf and between 180 and 230 mbsf (Fig. 5). These intervals occur over a period of approximately 4–6 Ma and could be synchronous with relatively low carbonate intervals at Sites 998 and 999.

Subunit IC

Intervals: Cores 165-1000A-41X through 52X
Age: late to middle Miocene
Depth: 370.5–486.0 mbsf, Hole 1000A

Subunit IC is distinguished by an abrupt drop in carbonate content at the Subunit IB/IC boundary, by increased magnetic susceptibility, a decrease in color reflectance (550 nm), and by overall low carbonate contents relative to the overlying Subunit IB and the underlying Subunit ID (Figs. 6, 12). This interval of lower carbonate content, especially in the upper half of Subunit IC at the end of nannofossil Zone CN5 and the beginning of Zone CN6, appears to be synchronous with the interval of extremely low carbonate values observed in both deeper Sites 998 and 999 at the middle/late Miocene boundary, and referred to as the carbonate crash (Fig. 12). The major lithologies include micritic nannofossil chalk with foraminifers, micritic nannofossil chalk with foraminifers and clays, nannofossil chalk with clays and micrite, clayey nannofossil chalk with micrite, clayey micritic chalk with nannofossils, and micritic nannofossil chalk with clays. They occur as medium- to thick-bedded units with gradational contacts. The dominant components include nannofossils, foraminifer fragments, micrite, and clay. Bulk rock XRD analyses show variable quantities of aragonite throughout Subunit IC, intermittent occurrences of dolomite, and possible traces of magnesian calcite. The relative abundance of quartz, based upon XRD whole-rock analyses, appears to increase across the Subunit IB/IC boundary. Thereafter, the quartz content is persistently high throughout Subunit IC, but declines rapidly across the Subunit IC/ID boundary. Minor quantities of clay minerals are present throughout the subunit, but peak intensities are too low to determine clay types. Throughout Subunit IC minor quantities of zeolites (clinoptilolite) are also identified. Bioturbation is moderate and many burrows are infilled with fine-grained pyrite. Disseminated pyrite also occurs commonly throughout the sections, giving the cores a mottled appearance.

As in Subunit IA, volcanic ash layers form a very minor component of Subunit IC. The layers are typically thin bedded and dark gray

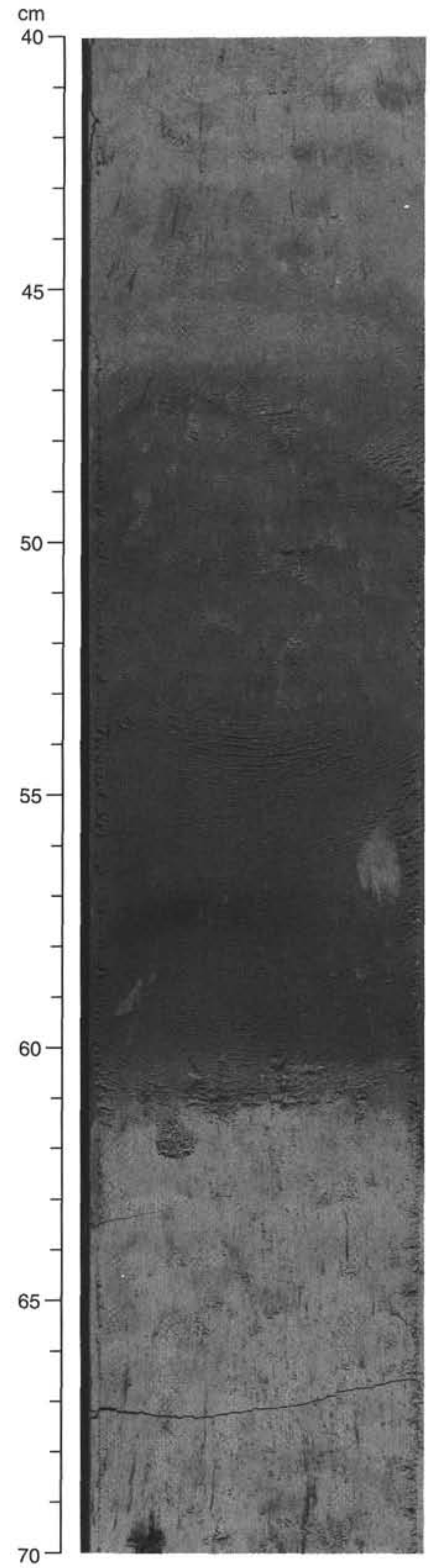

Figure 9. Core photograph of an upper Miocene volcanic ash layer (interval 165-1000A-22H-2, 40–70 cm), showing extensive bioturbation of the upper part and a burrow in the interior of the ash layer. The layer is dominantly composed of relatively coarse, clear, and fresh glass shards of rhyolitic composition.

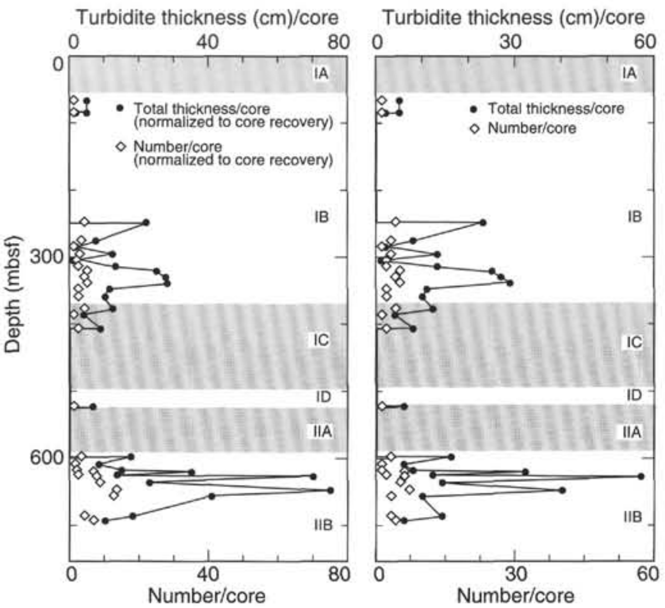

Figure 10. Downcore distribution of foraminiferal sands (turbidite deposits) at Site 1000 showing total thickness per core and number per core. The left diagram shows both data sets normalized for core recovery. Note the intermittent occurrence of turbidites at Site 1000. Turbidite layers occur in two specific intervals: (1) in the lower half of Subunit IB and the upper 30 m of Subunit IC from 260 to 400 mbsf during the early late Miocene, and (2) in the lower two thirds of Unit II from 590 to 700 mbsf during the late early Miocene.

to black; they have sharp bases and bioturbated tops, and are normally graded. Most of the layers have suffered extensive alteration, with volcanic glass being converted to smectitic clay and with secondary precipitation of pyrite. At the base of the layers, there is usually <10% phenocryst minerals such as feldspar, biotite, or amphibole. Some layers have been extensively burrowed by benthic organisms (Fig. 13).

A few coarse foraminiferal sands and silts occur in the upper 30 m of Subunit IC as thin- to medium-bedded, gray to slightly brownish gray layers (Fig. 10). The layers typically have sharp bases and bioturbated tops, and they exhibit normal grading. Many show parallel and cross-laminations overlying a massive base, and are interpreted as gravity-flow deposits with abundant reworked planktonic foraminifers in their coarse-sized sediment base. Overall, turbidite layers in Subunit IC represent a very minor sediment component, as they occur only in the upper 30 m of the subunit with a maximum of three layers per core, corresponding to a cumulative turbidite thickness of 12 cm per core normalized to core recovery or 1% of the total sediment thickness for this specific core. Cores 165-1000A-49X to 55X, from the bases of Subunits IC and ID, gave off a distinctive hydrocarbon smell when split. Analysis of these hydrocarbons is discussed in the "Organic Geochemistry" section (this chapter).

Subunit ID

Intervals: Core 165-1000A-53X through Section 165-1000A-55X-6, 70 cm
Age: middle Miocene
Depth: 486.0–513.4 mbsf, Hole 1000A

Subunit ID is distinguished from Subunit IC by higher carbonate content, lower magnetic susceptibility, and higher reflectance values (Fig. 6). The dominant lithology is olive gray to light olive gray, micritic nannofossil chalk with foraminifers. It occurs as thick-bedded, massive units that are moderately bioturbated. Interbedded within the

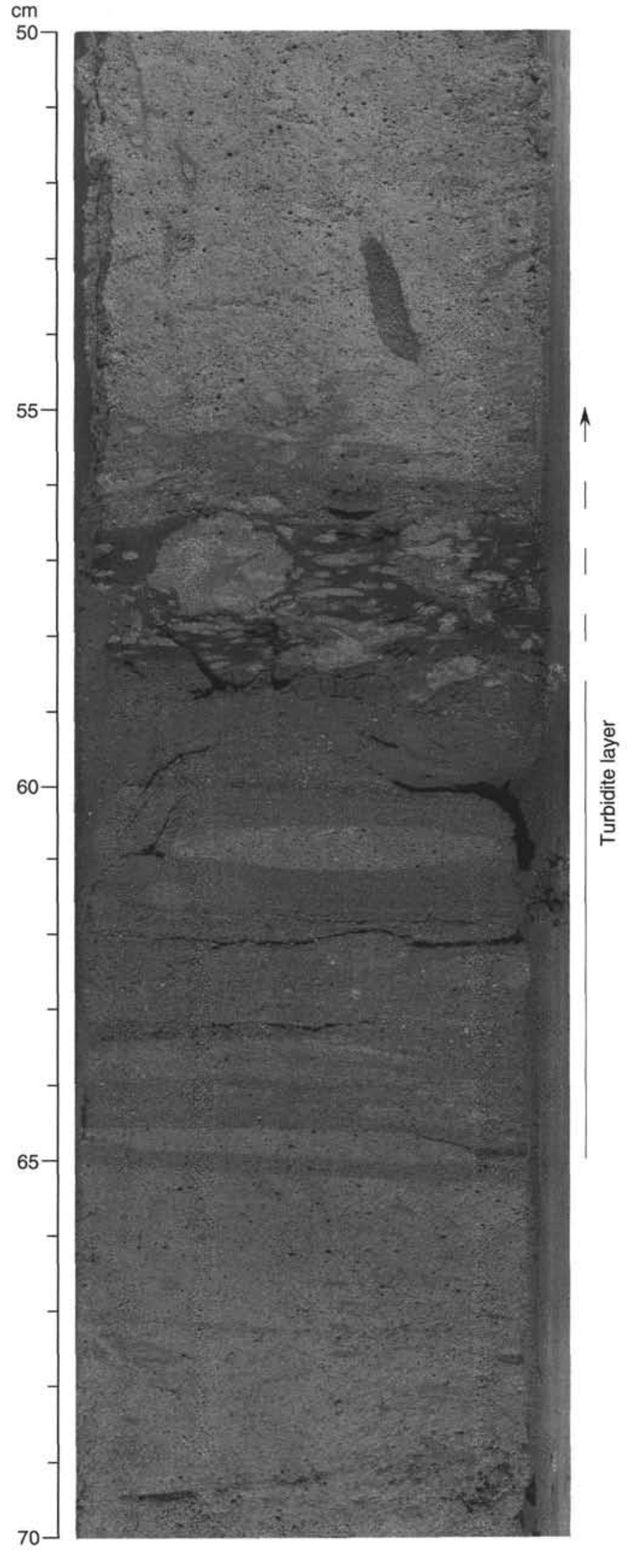

Figure 11. Foraminiferal sand layer in Subunit IB (interval 165-1000A-36X-4, 50–70 cm). Note parallel laminations at the base, normal grading, and fine-grained bioturbated top.

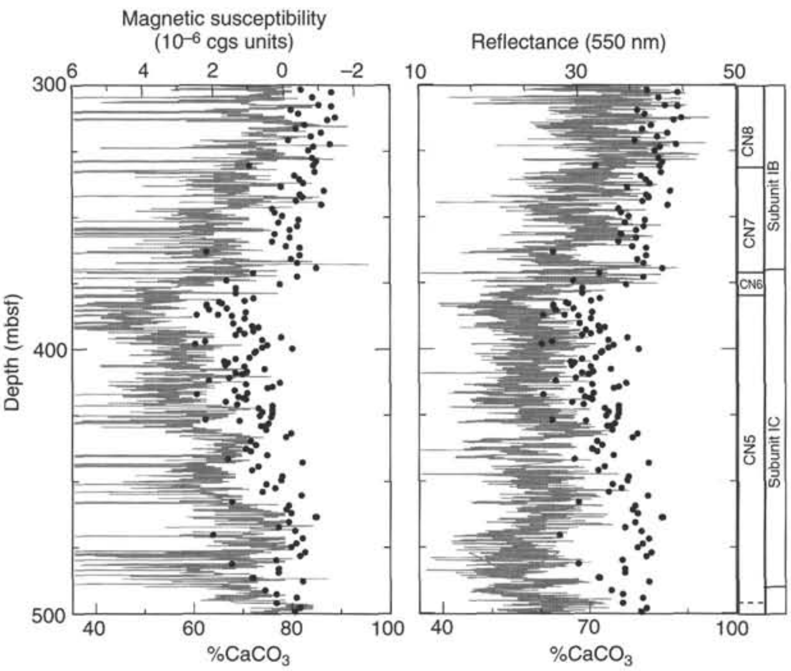

Figure 12. Variations in carbonate content (solid circles), magnetic susceptibility (shaded solid line), and color reflectance (shaded solid line) in Subunit IC. Nannofossil and foraminifer biostratigraphic zones are also shown. The occurrence of carbonate low values in the upper half of CN5 and the beginning of CN6 is synchronous with the interval characterized by extreme low carbonate values, referred to as the carbonate crash, observed at Sites 998 and 999 at the middle Miocene/late Miocene boundary interval.

major lithology are dark gray to black, altered volcanic ash layers with sharp bases and bioturbated upper contacts. Many of the ash layers contain abundant pyrite. The lithologic characteristics of Subunit ID are most similar to Subunit IB. Mineralogical components identified in Subunit ID by bulk-rock XRD analyses include calcite, some minor concentrations of dolomite, and traces of quartz and clinoptilolite. Aragonite and magnesian calcite are absent. Also, possible traces of opal CT are observed, which may be a precursor of its precipitation within Unit II.

Unit II

Intervals: Section 165-1000A-55X-6, 70 cm, through Core 165-1000A-59X; Sections 165-1000B-4R-1, 20 cm, through 22R-CC
Age: middle to early Miocene
Depth: 513.4–544.8 mbsf, Hole 1000A; 513.4–695.9 mbsf, Hole 1000B

Unit II consists of 146.5 m of well-lithified sediments composed mainly of calcareous nannofossil limestones with foraminifers and nannofossil micritic limestones with clay and foraminifers. The boundary between overlying Unit I and Unit II is based on the sharp downcore increase in the degree of lithification from chalks to limestones. The first appearance and downcore continuous occurrence thereafter of opal CT coincides with the transition from chalks in Unit I to limestones in Unit II. This lithologic boundary occurs approximately at the depth where Hole 1000A, drilled by APC/XCB, had to be abandoned and where Hole 1000B was drilled by RCB. The major lithologies occur as medium- to thick-bedded, homogenous units that are typically separated by gradational contacts. Distinctive layers, interbedded with the major lithologies, include volcanic ash layers and redeposited graded beds of foraminiferal sands. The former are produced by eolian transport of material to the site from explosive volcanic eruptions, whereas the latter are interpreted as sediments redeposited by gravity flows. Unit II is characterized by relatively large fluctuations of bulk carbonate content, with high values similar to those observed in Subunits IB and low values similar to the ones observed in Subunit IA and the upper part of Subunit IC. Fluctuation of the carbonate values display higher amplitudes in the lower two thirds of Unit II and could be related to the variable amount of dispersed volcanic ashes within the background sediment.

Unit II is divided into two subunits based on variations in carbonate content, variations in the volcanic ash layers, and the presence or absence of turbidite layers (Figs. 5, 10). Subunit IIA is characterized by relatively high carbonate values with a wide range of carbonate fluctuations. Although Subunit IIB displays some high carbonate values, the amplitudes of carbonate fluctuation in this lowest subunit are clearly higher than in the overlying Subunit IIA. The frequency and thickness of volcanic ash layers, though higher in Subunit IIB than in Subunit IIA, are not the basis for dividing Unit II in two subsections as the deposition of ash layers does not reflect changes in the depositional system. Instead, the absence or presence of turbidite layers is used to divide Unit II into two subunits. Subunit IIA is characterized by the absence of turbidite layers, whereas Subunit IIB has the highest frequency of turbidites in the entire cored section (a maximum of 14 layers per core, corresponding to a cumulative turbidite thickness of 75 cm per core normalized to core recovery or less than 7% of the total sediment thickness for the core with the maximum number of turbidites).

Subunit IIA

Intervals: Sections 165-1000B-4R-1, 20 cm, through 12R-1, 130 cm
Age: middle to early Miocene
Depth: 513.4–591.3 mbsf, Hole 1000B

Subunit IIA is composed of medium to very thick bedded gray, light gray, and grayish white calcareous nannofossil limestones with foraminifers; and gray, light greenish gray, light olive gray, and olive gray nannofossil micritic limestones with clay and foraminifers. It is distinguished from Unit I by an abrupt downcore increase in the degree of lithification. With increasing depth, the limestones gradually grade into grayish brown and light brownish gray interbeds of nannofossil micritic limestones with clay and foraminifers (Cores 165-1000B-9R and 11R to 12R).

The sediments are well indurated and moderately bioturbated; they have transitional boundaries, denoted by gradual color changes. Many of the burrows are somewhat flattened as a result of compaction. Major components include fine-grained carbonate grains, foraminifers, and clay minerals. Carbonate contents in Subunit IIA range from 80% to 90% (Fig. 7). The mineralogical character of Subunit IIA differs substantially from that of Unit I. Based upon bulk-rock

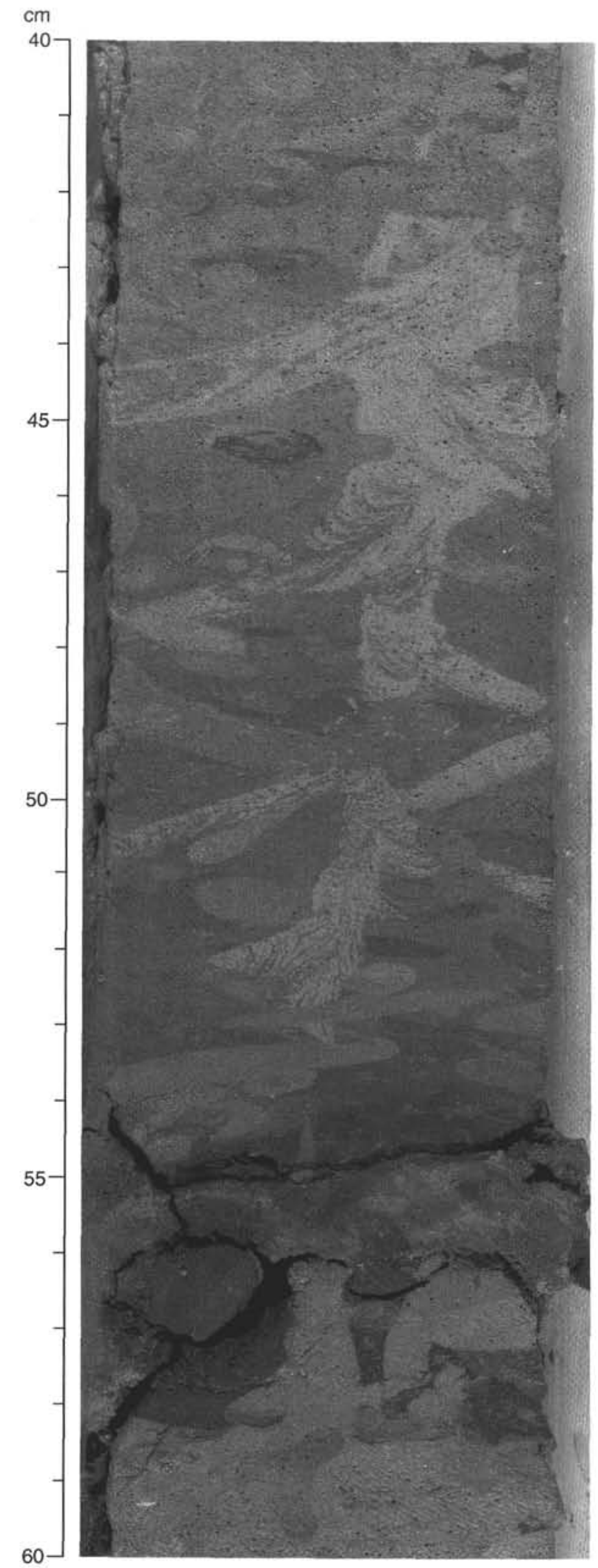

Figure 13. Extensively bioturbated volcanic ash layer from Subunit IC (interval 165-1000A-48X-2, 40–60 cm). Note the penetration of the central burrow through the entire thickness of the layer.

XRD analyses, calcite and diagenetic opal-CT dominate, and aragonite and magnesian calcite are absent (Fig. 8). Minor quantities of dolomite and rare clinoptilolite are also present. Pyrite is intermittently observed within burrow structures, and within Section 165-1000B-7R-6 reaction rims are present around several burrows. Elsewhere, well-developed *Zoophycos* burrows are frequently observed.

Volcanic ash layers form a minor component of Subunit IIA. Many layers are dark gray, and are normally graded with sharp bases and bioturbated tops. The majority are highly altered, with glass shards replaced by smectitic clay. At the bases of some layers, concentrations of phenocryst minerals such as feldspar and biotite are common. The frequency of ash layers increases across the Subunit ID/IIA boundary (see "Igneous Petrology and Volcanology" section, this chapter). The absence of redeposited sand- to silt-sized coarse sediment layers is also a characteristic of Subunit IIA.

Subunit IIB

Intervals: Section 165-1000B-12R-1, 130 cm, through Core 165-1000B-22R
Age: early Miocene
Depth: 591.3–695.9 mbsf, Hole 1000B

Subunit IIA consists of 104.6 m of light gray calcareous limestone with foraminifers and light brownish gray nannofossil micritic limestone with clay and foraminifers. The two lithologies alternate at the decimeter scale and are separated by gradational contacts, marked by changes in color. Carbonate contents in Subunit IIB range from 60% to 95% (Fig. 6) and display higher amplitude variations than in the overlying Subunit IIA. Numerous turbidite layers occur in Subunit IIB, where the highest frequency and cumulative thickness of turbidite layers for the entire Site 1000 is observed. This contrasts with the overlying turbidite-free Subunit IIA.

Major components include fine-grained carbonate grains and foraminifers. Bulk-rock XRD analysis shows these limestones to be dominated by calcite and opal CT. Aragonite and magnesian calcite are absent. Possible trace quantities of quartz (and clay?) are also present, together with minor clinoptilolite. Some dolomite is observed at the top of the subunit. Disseminated pyrite occurs within the background sediment and is often concentrated within burrows. Many of the burrows are flattened because of compaction.

The occurrence and abundance of normally graded sandy layers, interpreted to be turbidites, is a characteristic of Subunit IIB (Fig. 10). The beds typically have sharp and erosive basal contacts (Fig. 14) and gradational upper boundaries overprinted by bioturbation (Fig. 15). Sand- to silt-sized bases are generally massive or parallel laminated, and grade upward into clay-sized particles. The transition between the basal silt/sand and the upper clayey part may be gradational or sharp. The upper clayey part is typically moderately bioturbated. These layers range in thickness from 2 to 8 cm, but can reach up to 18 cm. Thin-section observations from the basal part of a turbidite from Sample 165-1000B-17R-5, 141–143 cm, show that the basal silt/sand units consist of both reworked planktonic foraminifers and larger benthic foraminifers derived from adjacent carbonate bank tops (Fig. 16).

Volcanic ash layers occur most frequently in Subunit IIB and correspond to the prominent Miocene peak in explosive volcanism that was documented at both Sites 998 and 999. The ash layers are typically thicker and coarser grained in Subunit IIB than in any other of the recovered sections. In Core 165-1000B-16R, there is a distinctive 30-cm-thick, dark gray volcanic ash layer (Fig. 17). The base is in sharp contact with the underlying sediment and shows normal grading with sand-sized phenocrysts of feldspar and biotite concentrated at the bottom. About 5 cm above the base of the layers, there are a series of concaving-upward structures that may be associated with dewatering of the layer during deposition. Above these structures is a 2-cm-thick zone of coarse pyrite, followed by the fine-grained top of

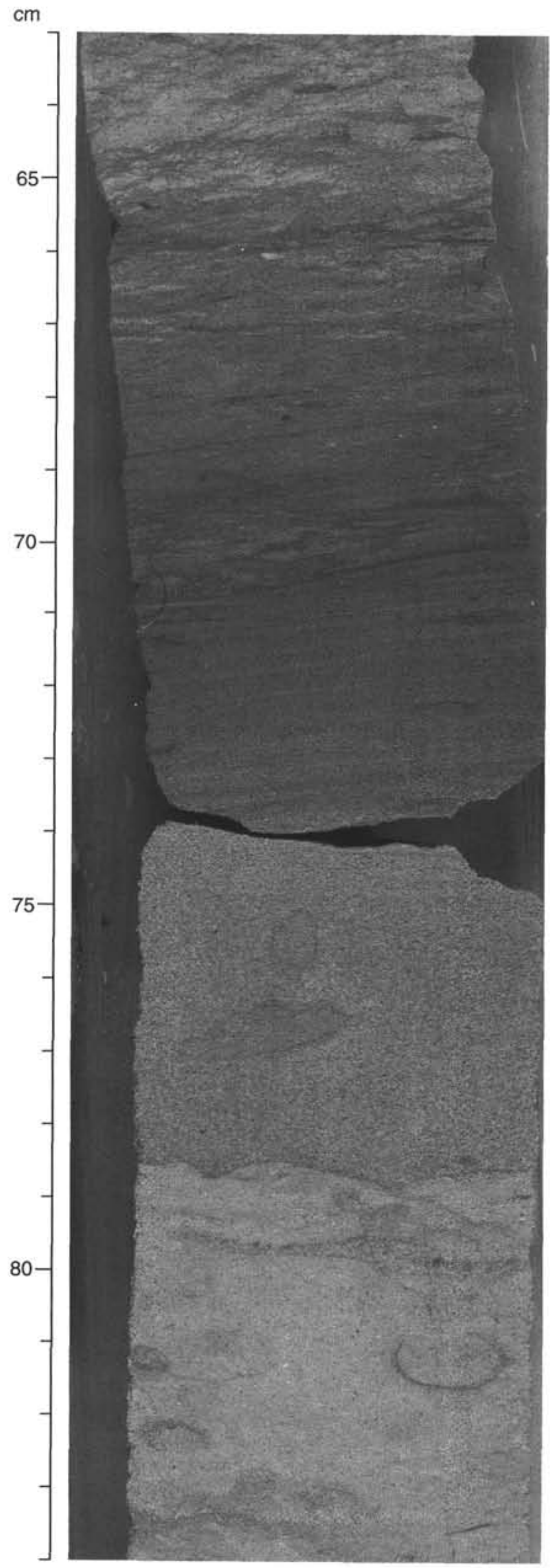

Figure 14. Foraminiferal sand layer in Subunit IIB (interval 165-1000B-17R-2, 63–84 cm). Note the erosive base, normal grading, and fine-grained bioturbated top.

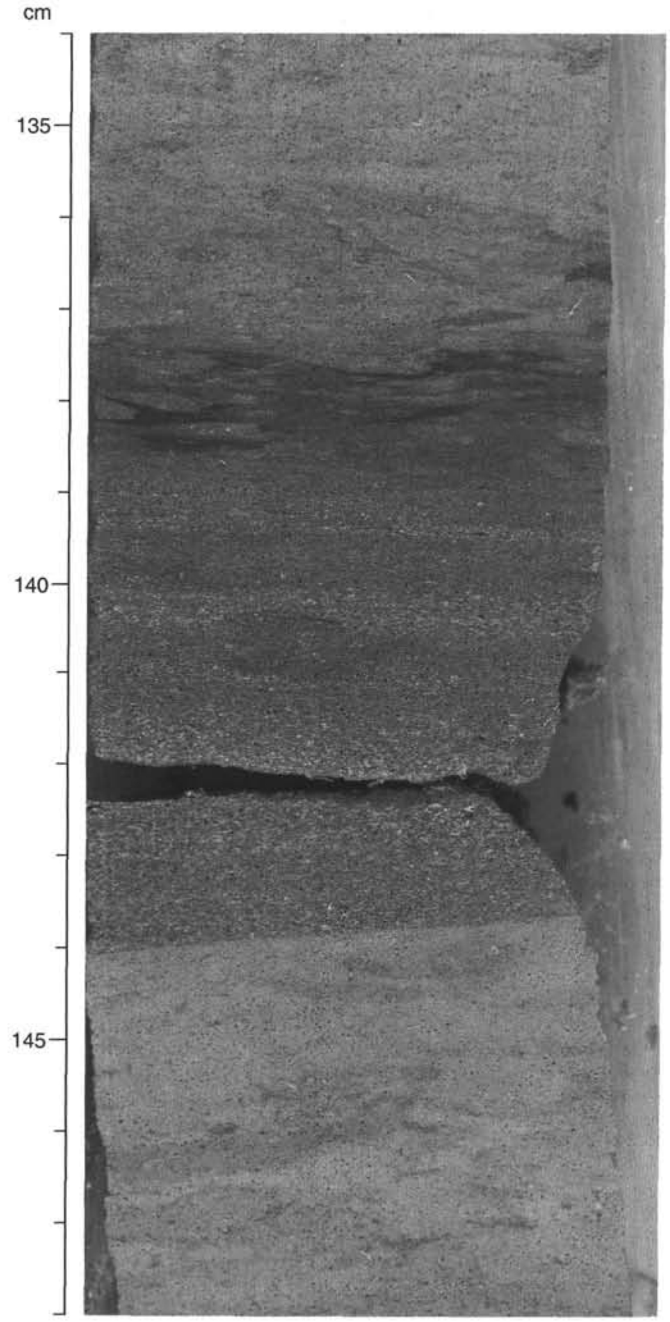

Figure 15. Foraminiferal sand layer in Subunit IIB (interval 165-1000B-17R-5, 134–148 cm). Note the sharp base, normal grading, and fine-grained bioturbated top. Thin section in turbidite between 141 and 143 cm is illustrated in Figure 16.

the layer. All of the glass in this layer is completely altered, with only the phenocrysts still preserved.

Discussion

A 695-m-thick, continuous, lower Miocene to recent sedimentary sequence was drilled at Site 1000 in the Pedro Channel on the NNR. This Neogene periplatform sequence consists mainly of nannofossil micritic oozes, chalks, and limestones with intermittent foraminifers and clays, deposited at relatively constant sedimentation rates of

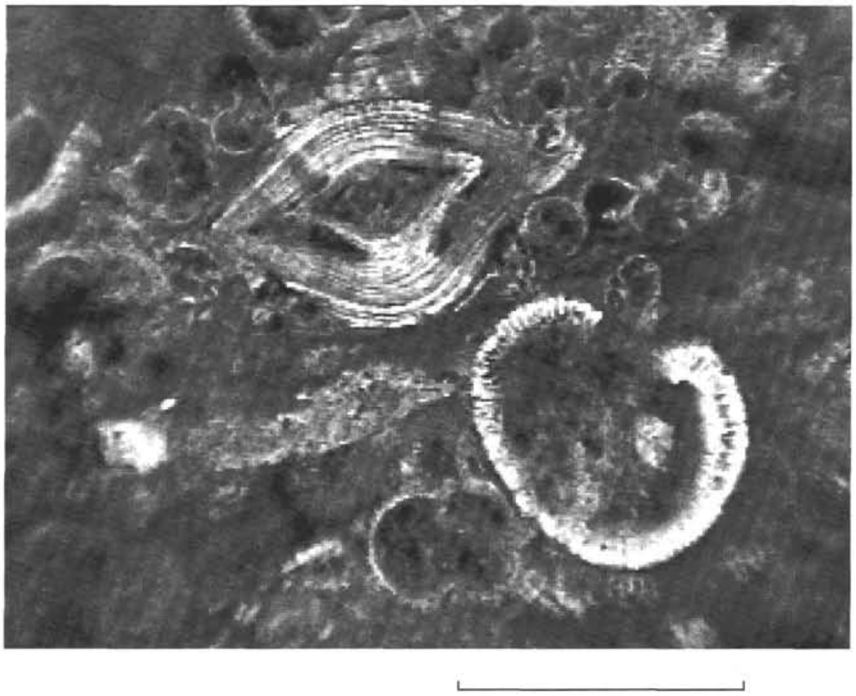

Figure 16. Scanned image of a thin section from the base of a turbidite in Sample 165-1000B-17R-5, 141–143 cm (illustrated in Fig. 15). Note the occurrence of larger foraminifers and echinoderm fragments, in addition to planktonic foraminifers.

nearly 35 m/m.y. for the past 20 m.y. (see "Sedimentation and Mass Accumulation Rates" section, this chapter).

Much of the periplatform sequence is turbidite-free and thus was deposited by settling through the water column of pelagic biogenic grains and fine bank-derived neritic carbonate particles. The latter originally were primarily aragonite and magnesian calcite, which have been subsequently altered through burial diagenesis into fine calcitic micrite. Although aragonite is absent from the upper part of the upper Miocene and lower part of the Pliocene, aragonite and possible traces of magnesian calcite, usual primary minerals for bank-derived carbonate, have been detected as deep as 470 mbsf in middle Miocene chalks. The Pedro Channel is surrounded by several isolated shallow carbonate banks with no source of siliciclastic sediment in close proximity, so fine detrital noncarbonate (quartz and clays), a secondary component in these periplatform sediments, must be brought laterally into Pedro Channel by oceanic currents and by atmospheric dust transport. Non-$CaCO_3$ mass accumulation rates seem to reach an overall maximum at the middle/upper Miocene boundary interval.

Based on visual core descriptions, only 84 turbidite layers have been recognized in the 695 m of recovered periplatform ooze, chalk, and limestone at Site 1000, reaching a cumulative thickness of 5.3 m (normalized for core recovery; Fig. 10). Although material redeposited as turbidites makes up only 0.7% of the total thickness of the sedimentary sequence at Site 1000, these layers, especially the ones with neritic components in Subunit IIB, will provide important information about the shallow-water environments (carbonate bank tops) adjacent to the Pedro Channel. The total thickness and the number of turbidite layers vary significantly downcore. Two intervals with turbidites occur in the lower part of Subunit IB (upper Miocene) and in Subunit IIB (lower Miocene). Both intervals are characterized by a similar number of events per core, if not normalized to take into account the core recovery. When recovery is factored in, however, the overall thickness of the turbidites in the lower Miocene interval was clearly much larger than for the upper Miocene interval (Fig. 10).

Volcanic ash layers are a minor component in most of the sedimentary sequence at Site 1000. Volcanic ash layers occur more frequently in Subunit IIB and are typically thicker and coarser grained than in the other units. They correspond to the prominent Miocene peak in explosive volcanism that was documented at both Sites 998 and 999 between 18 and 19 m.y. (see "Igneous Petrology and Volcanology" section, this chapter).

The oldest sedimentary rocks recovered at Site 1000 are well-lithified, periplatform limestones of early Miocene to early middle Miocene age (Subunits IIB and IIA). Before Leg 165 began, the seismic facies image of these limestones was interpreted to represent a drowned shallow carbonate bank that would have been part of a carbonate megabank that stretched on the crest of the Nicaragua Rise from the shelves of Honduras and Nicaragua to the island of Jamaica and would have hampered the development of the Caribbean Current as well as facilitate the interoceanic flow between the low latitudes of the North Atlantic and the eastern Pacific. Drilling results and revised velocity estimates now place the top of the drowned bank to as much as 100 m below the Site 1000 TD in the subseafloor of the Pedro Channel. The presence of the drowned bank top at 800–1000 mbsf in the Pedro Channel is also imaged by high-amplitude, low-frequency seismic facies on the high-resolution seismic crossing at Site 1000 (see "Seismic Stratigraphy" section, this chapter). Its age is considerably older than predicted prior to drilling, but presumably would correspond to the age of dredged reefal limestones from the same seismic facies cropping out on the seafloor in several areas of the Pedro Channel (Droxler et al., 1992). The first occurrence of several turbidite layers with redeposited neritic carbonate grains in the lower 100 m of Site 1000 (Subunit IIB) is also an indication that the source for this shallow-water carbonate material was becoming more proximal.

In contrast with the late early Miocene (20–16 Ma), the middle Miocene (16–11 Ma) periplatform chalks and limestones are devoid of turbidites. Periplatform chalks of the middle Miocene still include aragonite and traces of magnesian calcite, which is rather exceptional when the age of the chalks and burial depth to as much as 470 mbsf are considered.

Carbonate accumulation rates seem to reach a maximum at about 12–13 Ma and decrease sharply through the middle to late Miocene boundary interval to reach rates that remain constant for most of the

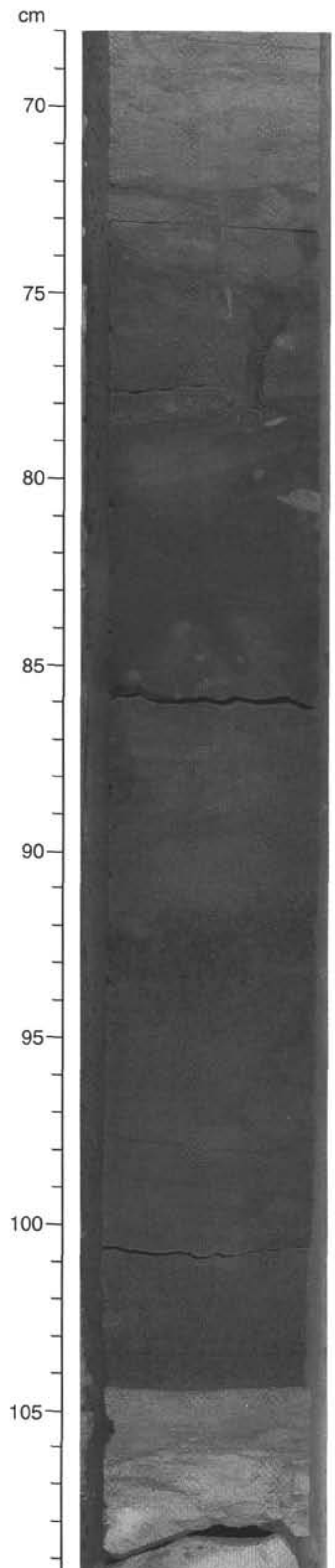

Figure 17. Volcanic ash layer with characteristic sharp base and bioturbated top (interval 165-1000B-16R-4, 68–110 cm). Note the pyrite-rich layer at 92–93 cm.

late Miocene (see "Sedimentation and Mass Accumulation Rates" section, this chapter). The middle Miocene interval is also characterized by a gradual decrease of the carbonate content values from a maximum of 90% in Subunit IIA to a well defined carbonate minimum (60%) at the middle/upper Miocene boundary interval. This gradual decrease in carbonate values seems to display also some cyclic character and appears to correspond to a gradual increase of the noncarbonate accumulation rates.

The well-defined carbonate minimum at the very beginning of the late Miocene (end of nannofossil Biozone CN5 and beginning of CN6) corresponds to the lowest accumulation rate of $CaCO_3$ (average 3–4 g/cm^2/k.y.) in the Miocene and to the highest accumulation rates of non-$CaCO_3$ for the entire Neogene section of Site 1000. This event appears to be synchronous with a pronounced decrease in carbonate deposition or the carbonate crash at Site 999 in the Colombian Basin and at Site 998 on the Cayman Rise (Fig. 18). In these two deep sites on both the south and north side of the Nicaraguan Rise, a substantial reduction in carbonate accumulation rates and the poor preservation of calcareous microfossils in smear slides and washed paleontology samples suggest that carbonate-dissolution and a shoaling of the lysocline and carbonate compensation depth (CCD) are responsible for the observed patterns. It is difficult to envisage a similar scenario at Site 1000 because its paleowater depth had to be as deep as today, or possibly even shallower, well above the calcite lysocline. Moreover, preservation of calcareous nannofossils and planktonic foraminifers in Site 1000 did not appear to have decreased during that interval. However, the water column at Site 1000, in spite of its relative shallow depth, is just at saturation or slightly oversaturated with respect to aragonite, and at saturation or slightly undersaturated with respect to magnesian calcite (Droxler et al., 1991). It is conceivable, therefore, that the late/middle Miocene, bank-derived, fine aragonite and magnesian calcite suffer some maximum seafloor dissolution at the time of the carbonate crash. Dissolution of bank-derived aragonite and magnesian calcite is observed intermittently during the late Quaternary in the Pedro Channel, in the Walton Basin, and in the Lesser Antilles at water depths comparable with the depth of Site 1000 and especially deeper than 1100 m (Schwartz, 1996; Haddad, 1994; Glaser and Droxler, 1993; Schlager et al., 1994; Reid et al., 1996). Moreover, during the late Quaternary, intervals of known enhanced dissolution of aragonite and magnesian calcite at relatively shallow depths between 1100 and 1800 m in the periplatform oozes of the Pedro Channel, the Walton Basin, and the Lesser Antilles (e.g., Holocene, Stage 5e, first half of Stage 6, and the mid-Brunhes dissolution maximum 0.4 Ma) correspond to intervals of major dissolution of calcite-bearing ooze in the deep Venezuelan Basin and Colombian Basin (Haddad, 1994; Schwartz, 1996; Reid et al., 1996; Cofer-Shabica, 1987; Prell, Gardner, et al., 1982). The subthermocline water depth of Site 1000 will allow us to study the carbonate crash at the time of the middle to late Miocene boundary interval in a range from intermediate- to deep-water masses.

The noncarbonate accumulation rates peak at the time of the carbonate crash in the three Caribbean sites, particularly at Site 999 in the Colombian Basin and at Site 1000 on the NNR. The major global fall in sea level at 10.5 Ma (Haq et al., 1987) appears to be synchronous with the timing of the carbonate crash and could explain the high accumulation rates of noncarbonate components at that time. This increase of noncarbonate input into the ocean due to exposure of continental shelves would have enhanced by dilution the effect of the carbonate crash. Further shore-based studies of this interval in Sites 998, 999, and 1000, and comparisons with sites elsewhere that record this profound change in the carbonate system (e.g., Leg 138 sites in the eastern equatorial Pacific; Lyle et al., 1995), should help to develop a scenario to understand the origins of the middle/late Miocene carbonate crash.

The periplatform oozes for the last 8 Ma at Site 1000 are very homogenous, and the upper 300 m of this periplatform section were

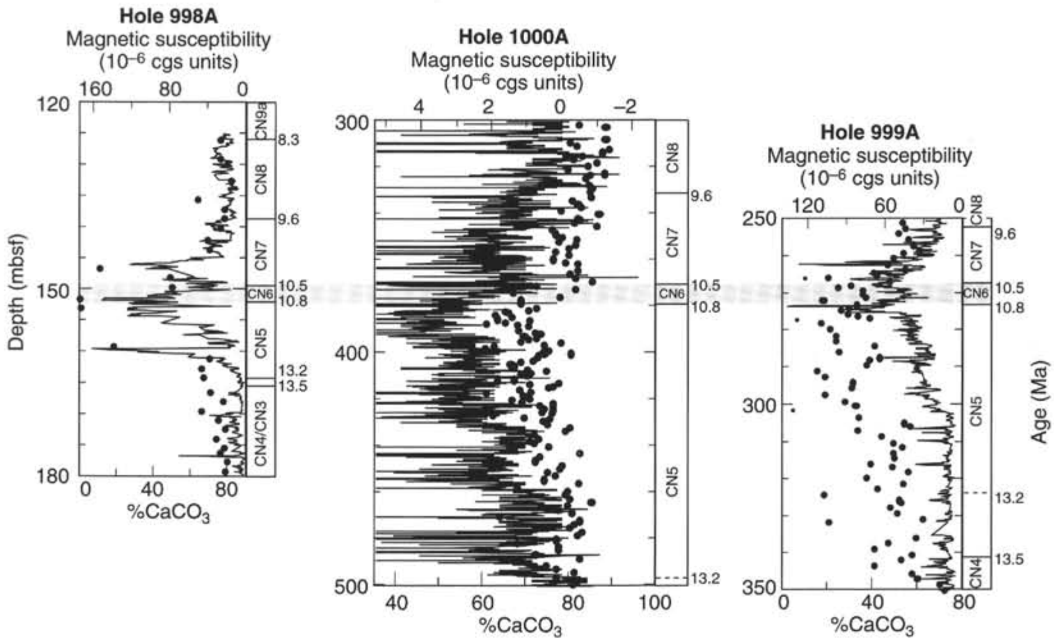

Figure 18. Comparison of Site 998 on the Cayman Ridge (Yucatan Basin), Site 1000 in the Pedro Channel (northern Nicaraguan Rise), and Site 999 on the Kogi Rise (Colombian Basin), illustrating the Caribbean carbonate crash.

cored by APC, providing material ideal to conduct a post-cruise high-resolution stratigraphy to address pertinent questions on the Caribbean paleoceanography before, during, and after the closure of the Isthmus of Panama at a subthermocline water depth. The late Miocene and Pliocene periplatform oozes (Subunit IB) are distinguished by their higher overall total carbonate content and the general lack of redeposited material, with the exception in the early part of the late Miocene when a few small turbidite layers with reworked planktonic foraminifers were deposited. The absence of aragonite in the middle part of Subunit IB (6.5–4.5 Ma), during an interval including the uppermost Miocene and the basal Pliocene, corresponds to a time characterized by relatively lower carbonate accumulation rates. The late part of the Pliocene and the Pleistocene (roughly Subunit IA) is characterized by the lowest carbonate accumulation rates, following a sharp decrease of the rates from 3 to 4 g/cm^2/k.y. between 3 and 2.7 Ma. The variations in magnetic susceptibility of the periplatform oozes in the past 1 Ma, when compared with existing carbonate and planktonic oxygen isotope records from existing piston cores, can be interpreted as cyclic changes of detrital noncarbonate components related to the Quaternary glacial-interglacial climatic fluctuations.

BIOSTRATIGRAPHY

Calcareous Nannofossils

Standard smear slides were prepared at a frequency of one per section, and standard nannofossil datums (see Table 2, "Explanatory Notes" chapter, this volume) were determined as precisely as possible based on the approximately 250 slides examined. Theoretically, depth uncertainty is about 1.5 m throughout Holes 1000A and 1000B. This uncertainty increases significantly as preservation deteriorates in the lower part of the section. The nannofossil datums determined at Site 1000 are compiled in Table 3, and the zonal boundaries of Okada and Bukry (1980) are illustrated in Figures 53 and 54.

Nannofossil preservation is generally good to excellent from the Pleistocene through the Pliocene (Cores 165-1000A-1H to 19H), good to moderate in the upper Miocene (Cores 165-1000A-20H to 42X), moderate deteriorating downward to poor in the middle Miocene (Cores 165-1000A-43X to 165-1000B-10R), and generally poor in the lower Miocene (Cores 165-1000B-11R to 22R). In the latter interval, specimens are heavily overgrown, moderately etched, and fragmented. Short-term abundance and preservational fluctuations are seen throughout the section, but are most prominent in the Pliocene and Pleistocene. Here, individual samples are characterized by significant amounts of overgrowth, and others by dilution with fine-fraction aragonite needles, presumably transported off the Pedro Bank.

The tropical location of Site 1000 resulted in a diverse nannofossil assemblage where preservation is good, in much of the upper Miocene to Pleistocene interval. The Neogene section was deposited at moderately high sedimentation rates, averaging 25 m/m.y. in the Pleistocene and uppermost Pliocene, increasing to an average of 37 m/m.y. in the lower upper Pliocene to lower Miocene. The sequence appears to be complete to within biostratigraphic resolution. Most of the Cenozoic zones and subzones of Okada and Bukry (1980) can be recognized (Table 3; Figs. 53, 54). Minor reworking is observed sporadically through the section. The presence of *Cyclicargolithus floridanus,* large (~8 μm) specimens of *Reticulofenestra pseudoumbilicus,* and *Sphenolithus heteromorphus* in samples of Pliocene and Pleistocene age indicates that this reworking is from an early to middle Miocene source.

Pleistocene

A continuous Pleistocene section was recovered from Hole 1000A (Table 3). Sedimentation rates are approximately 25 m/m.y., although preliminary biostratigraphy indicates that these rates varied significantly (see "Sedimentation and Mass Accumulation Rates" section, this chapter). All of the Pleistocene nannofossil zones and subzones of Okada and Bukry (1980) can be defined in the uppermost part of Hole 1000A (Table 3; Fig. 53). Most of the additional Pleistocene nannofossil datums of Takayama and Sato (1987) and Sato et al. (1991) can be detected also. *Reticulofenestra asanoi* was observed in Samples 165-1000A-4H-3, 50 cm, and 4H-4, 50 cm. Samples 165-

Table 3. Nannofossil datums, absolute ages, and depths at Site 1000.

Event	Zone (base)	Age (Ma)	Core, section, interval (cm)	Depth (mbsf)
Hole 1000A:				
B *Emiliania huxleyi*	CN15	0.248	1H-2, 50, to 1H-3, 50	2.55
T *Pseudoemiliania lacunosa*	CN14b	0.408	3H-1, 50, to 3H-2, 50	13.92
T *Reticulofenestra asanoi*		0.88	4H-2, 50, to 4H-3, 50	25.05
B *Gephyrocapsa parallela*	CN14a	0.94	4H-3, 50, to 4H-4, 50	26.55
B *Reticulofenestra asanoi*		1.17	4H-4, 50, to 4H-5, 50	28.05
T large *Gephyrocapsa* spp.		1.23	4H-6, 50, to 4H-CC	32.01
T *Helicosphaera sellii*		1.26	5H-3, 50, to 5H-4, 50	36.05
B large *Gephyrocapsa* spp.		1.48	5H-5, 50, to 5H-6, 50	39.05
B *Gephyrocapsa oceanica*		1.64	5H-6, 130, to 5H-CC	40.98
T *Calcidiscus macintyrei*		1.64	5H-6, 130, to 5H-CC	40.98
B *Gephyrocapsa caribbeanica*	CN13b	1.71	6H-2, 50, to 6H-3, 50	44.05
T *Discoaster brouweri*	CN13a	1.95	7H-1, 50, to 7H-2, 50	52.05
T *Discoaster pentaradiatus*	CN12d	2.36	8H-1, 50, to 8H-2, 50	61.55
T *Discoaster surculus*	CN12c	2.51	8H-5, 50, to 8H-6, 50	67.55
T *Discoaster tamalis*	CN12b	2.82	9H-5, 50, to 9H-6, 50	77.05
T *Sphenolithus* spp.		3.62	13H-1, 60, to 13H-2, 60[a]	109.15
T *R. pseudoumbilicus*	CN12a	3.83	14H-2, 50, to 14H-3, 50	120.05
T *Amaurolithus* spp.	CN11	4.50	17H-2, 50, to 17H-3, 50	148.55
B *Ceratolithus rugosus*	CN10c	5.046	17H-4, 50, to 17H-5, 50	151.55
T *Ceratolithus acutus*		5.046	17H-5, 50, to 17H-6, 50	153.05
B *Ceratolithus acutus*	CN10b	5.089	19H-1, 50, to 19H-2, 50	166.05
T *Discoaster quinqueramus*	CN10a	5.537	19H-7, 50, to 19H-CC	174.53
B *Amaurolithus* spp.	CN9b	7.392	27H-CC to 28H-1, 50	250.79
B *Discoaster berggrenii*	CN9a	8.281	31H-5, 50, to 31H-6, 50	286.05
T *Discoaster hamatus*	CN8a	9.635	36X-6, 50, to 36X-CC	331.11
B *Discoaster hamatus*	CN7	10.476	40X-6, 50, to 40X-CC	369.70
B *Catinaster coalitus*	CN6	10.794	41X-5, 50, to 41X-6, 50	377.25
T *Cyclicargolithus floridanus*		13.23	54X-2, 50, to 54X-3, 50	498.35
T *Sphenolithus heteromorphus*	CN5a	13.523	55X-6, 50, to 55X-CC	513.64
T *Helicosphaera ampliaperta*	CN4	15.6	Below base of section	
Hole 1000B:				
T *Helicosphaera ampliaperta*	CN4	15.6	8R-4, 50, to 8R-5, 50	557.35
B *Sphenolithus heteromorphus*	CN3	18.2	17R-4, 50, to 17R-5, 50	642.30
T *Sphenolithus belemnos*		18.3	17R-4, 50, to 17R-5, 50	642.30
B *Sphenolithus belemnos*	CN2	19.2	20R-2, 42, to 20R-CC	668.90

Notes: T = top of species range (last appearance datum), B = base of species range (first appearance datum). This entire table also appears on CD-ROM (back pocket). [a]Event lies in disturbed core.

1000A-4H-CC through 5H-5, 50 cm, contain specimens of large *Gephyrocapsa.* The last occurrence (LO) of *Helicosphaera sellii* is placed between Samples 165-1000A-5H-3, 50 cm, and 5H-4, 50 cm.

Pliocene

The Pliocene/Pleistocene boundary, which lies close to the boundary of Subzones CN13b/CN13a at the first occurrence (FO) of *Gephyrocapsa caribbeanica,* is placed between Samples 165-1000A-6H-2, 50 cm, and 6H-3, 50 cm. This corresponds to the base of medium-sized (>4 µm) *Gephyrocapsa* defined by Raffi et al. (1993). Sedimentation rates average 25 m/m.y. in the uppermost Pliocene and 37 m/m.y. in the remainder of this series. All of the Pliocene zones and subzones of Okada and Bukry (1980) can be defined at Site 1000 (Table 3; Fig. 53). Because of the rarity of discoasters in some samples and significant overgrowth in others, we had some difficulty in determining the LO of *Discoaster pentaradiatus, D. tamalis,* and particularly *D. surculus.* The LO of *Sphenolithus* spp. (*S. abies* and *S. moriformis*) lies in Core 165-1000A-13H, between Samples 165-1000A-13H-1, 60 cm, and 13H-2, 60 cm (two specimens were observed in Sample 165-1000A-12H-6, 50 cm, but they occur with *S. heteromorphus* and are thought to be reworked from the Miocene). Core 165-1000A-13H is sedimentologically disturbed and has a significant water content. Our samples were taken in more cohesive intervals and show a consistent increase in the relative abundance of *Sphenolithus* spp. below its last occurrence. The identical depth interval was cored in Hole 1000B (Core 195-1000B-2R) and we observed the LO of *Sphenolithus* spp. at an equivalent depth (between Samples 165-1000B-2R-1, 50 cm, and 2R-2, 50 cm); however, we note that in samples below this event, the increase in the relative abundance (a more precise method of correlation; e.g., Backman and Shackleton, 1983) of *Sphenolithus* spp. occurs at a lower depth level (by over 1 m) in Hole 1000B than in Hole 1000A. *Sphenolithus* spp. becomes abundant (more than 10 specimens observed in each field of view) between Samples 165-1000A-13H-4, 50 cm, and 13H-5, 50 cm. However, this taxon is not abundant in Core 165-1000B-2R, including the core catcher. Thus, we postulate that the equivalent depth interval in Core 165-1000B-2R is marginally younger than that in Core 165-1000A-13H. The LO of *Reticulofenestra pseudoumbilicus* lies between Samples 165-1000A-14H-2, 50 cm, and 14H-3, 50 cm. Only a few specimens of this species, which is differentiated from other species of *Reticulofenestra* by having a diameter greater than 5 µm (e.g., Young, 1990), have been observed in Samples 165-1000A-14H-3, 50 cm, and 14H-5, 50 cm. These specimens are mostly 6–7 µm in diameter and therefore could be reworked from older horizons. The abundance of *R. pseudoumbilicus* increases in Sample 165-1000A-14H-6, 50 cm, and below, and smaller specimens are common in these intervals. Markers in the lower Pliocene, *Amaurolithus* spp., *Ceratolithus rugosus,* and *C. acutus* are rare, and more detailed study is required to confirm these datums.

Miocene

The Miocene/Pliocene boundary is placed between the LO of *Discoaster quinqueramus* and the FO of *Ceratolithus acutus* between Samples 165-1000A-19H-CC and 19H-1, 50 cm. Sedimentation rates in the upper Miocene and upper part of the middle Miocene average about 37 m/m.y. and decrease to 20 m/m.y. in the Zone CN6 interval of the carbonate crash. Rates average ~27 m/m.y. for the lower part of the middle Miocene and the early part of that epoch. Most of the Miocene zones and subzones of Okada and Bukry (1980) can be delineated (Table 3; Fig. 53). We found that *Discoaster berggrenii* becomes very rare toward the end of its range, with the central knob reduced in size, and difficult to observe due to overgrowth; thus, the FO of this species, which defines the base of Zone CN9, is somewhat tentative. We did not observe *Discoaster loeblichii,* the FO of which defines the base of Subzone CN8b, and therefore cannot divide Subzones CN8a and CN8b in Hole 1000A. The base of Subzone CN5b cannot be determined precisely due to the rarity of the marker taxon, *Discoaster kugleri,* and its resemblance to other taxa when overgrown and fragmented. Thus, Samples 165-1000A-41X-6, 50 cm, down to 55X-CC are placed in Zone CN5 based on the absence of *Catinaster coalitus* and *Sphenolithus heteromorphus. Helicosphaera ampliaperta,* the LO of which defines the base of Zone CN4, is observed in and below Sample 165-1000B-8R-5, 50 cm. The top of the acme of *Discoaster deflandrei* lies between Samples 165-1000B-9R-CC and 10R-CC; thus, we tentatively place the early/middle Miocene boundary between these points. The FO of *Sphenolithus heteromorphus* is placed between Samples 165-1000B-17R-4, 50 cm, and 17R-5, 50 cm. Some specimens with small spines were observed in the latter sample. The LO of *S. belemnos* is tentatively placed between the same samples. However, specimens in the upper part of the range of this species have smaller spines than are usual for this species. A number of specimens that possess column structures identical to those of *S. belemnos* were observed in these samples, and it is possible that the spines of these specimens have been broken. Specimens in the lower part of the range of this species have extended spines typical of this species. The base of *S. belemnos* is placed between Samples 165-1000B-20R-2, 42 cm, and 20R-CC. Isolated specimens of *S. delphix* have been observed in samples from Cores 165-1000B-20R to 22R confirming that the base of the section is within lowermost Miocene Zone CN1.

Planktonic Foraminifers

Site 1000 is located in 916 m water depth on the NNR. Stratigraphic ranges of planktonic foraminifers at this site to a large extent resemble those found at other Leg 165 sites and those found at deeper pelagic sites in the western tropical Atlantic on Leg 154 (Curry, Shackleton, Richter, et al., 1995; Chaisson and Pearson, in press). The shallowness of the seafloor at this site improves the quality of preservation over that of previous Leg 165 sites, and some Miocene zone bases and datums are found at Site 1000 that could not be recognized at the earlier sites (Table 4).

Pleistocene–Pliocene

Pliocene–Pleistocene Zones N22 through N19 were problematic in Hole 1000A because of the irregular stratigraphic distributions of marker species. The base of Zone N22 is marked by the FO of *Truncorotalia truncatulinoides* between Samples 165-1000A-4H-CC and 5H-CC. Compared to Sites 998 and 999, this datum is in a relatively high position, which suggests that sediment has been removed from this site during the Pleistocene, that sedimentation rates were low, or that *T. truncatulinoides* appears late (<2.0 Ma) at this site. The LOs of *Globigerinoides fistulosus* (1.7 Ma) and *Menardella exilis* (2.2 Ma) are also between Samples 165-1000A-4H-CC and 5H-CC. However, in the western tropical Atlantic (Curry, Shackleton, Richter, et al., 1995; Chaisson and Pearson, in press) *Menardella exilis* ranged higher than the level associated with the age assigned to this datum by Berggren et al. (1985). The LO of *Menardella miocenica* (2.3 Ma) is between Samples 165-1000A-6H-CC and 7H-CC. In contrast to *M. exilis,* the age of this datum (Berggren et al., 1985) is upheld in the western tropical Atlantic and it more likely represents a reliable datum at this Caribbean site. Additional credence is given to the *M. miocenica* datum by its association with the Atlantic reappearance of *Pulleniatina obliquiloculata* (2.3 Ma) and the LO of *Menardella pertenuis* (2.6 Ma) between Samples 165-1000A-6H-CC and 7H-CC. There is no sedimentological evidence for turbidites or unconformities in Cores 165-1000A-5H, 6H, or 7H (see "Lithostratigraphy" section, this chapter).

The LOs of *Menardella multicamerata* and *Dentoglobigerina altispira* (3.0 Ma) are between Samples 165-1000A-10H-CC and 11H-CC. These datums were reliable and within one section of each other at Leg 154 sites in the western tropical Atlantic (Curry, Shackleton, Richter, et al., 1995; Chaisson and Pearson, in press).

Pliocene sediments were disturbed by coring operations in Hole 1000A and, while washing down to the lower Miocene to begin rotary coring in Hole 1000B, two cores were recovered in the Pliocene to replace the disturbed Hole 1000A material. The core catcher of Core 165-1000B-1R was found to be equivalent in age to that of Core 165-1000A-11H. However, the quality of sediment differed; although the preservation of planktonic foraminifers was comparable with that found in Sample 165-1000A-11H-CC, Sample 165-1000B-1R-CC did not disaggregate readily and included more benthic foraminifers. The assemblage of this sample was attributable to the top of Zone N19, but it also included significant numbers of *Paragloborotalia mayeri,* a species restricted to the section below the base of Zone N15. Further evidence of reworking in Sample 165-1000B-1R-CC is given by numerous specimens of *Globigerinoides trilobus* and rare specimens of *Globoturborotalita nepenthes* of a preservational state and morphological type similar to those found in the upper Miocene sediments of Hole 1000A.

Miocene

The "*pachyderma* event" identified at Site 999 is present in possibly truncated form at Site 1000. The interval of dextrally coiling *Neogloboquadrina pachyderma* found at the top of the event at Site 999 is not present at Site 1000, based on the preliminary shipboard core-catcher analysis. The numbers of sinistrally coiling *N. pachyderma* are not as great at the Nicaraguan Rise as they are at the Kogi Rise.

The base of Zone N19 approximating the Miocene/Pliocene boundary is indicated by the FO of *Sphaeroidinella dehiscens* between Samples 165-1000A-23H-CC and 24H-CC. Examination of other datums (see Table 4) suggests that this event is too low in the section to represent the 5.6 Ma age given by Berggren et al. (1985). Interpolation between the LO of *Hirsutella cibaoensis* (5.0 Ma) between Samples 165-1000A-16H-CC and 17H-CC and the FO of *Hirsutella margaritae* (6.0 Ma) between Samples 165-1000A-25H-CC and 26H-CC suggests that the Miocene/Pliocene boundary should be in Core 165-1000A-21H. The apparent diachroneity of the *S. dehiscens* datum at Site 1000 may be ascribable to the relatively shallow water at the site, which will be investigated in post-cruise studies.

As at Sites 998 and 999, the stratigraphic record of *Globorotalia tumida* is too poorly developed at Site 1000 to define the base of Zone N18 accurately. Consequently, Zone N18 was combined with Zone N17, as it was at previous sites. The base of the combined Zone N17/N18 is defined by the FO of *Globorotalia plesiotumida* between Samples 165-1000A-35X-CC and 36X-CC. The FO of *Globigerinoides conglobatus,* between Samples 165-1000A-22H-CC and 23H-CC, seems to be high at this site; it is above the FO of *Hirsutella margaritae* in sediments attributable to Zone N19. The FO of *Candeina nitida* is difficult to constrain at Site 1000 because of the presence of specimens that may be attributable to *Candeina nitida praenitida* (Blow, 1969) in Samples 165-1000A-36X-CC and 37X-CC. Kennett and Srinivasan (1983) do not distinguish between these two morphotypes, but it is unclear whether the Berggren et al. (1995) datum is based on the fully developed form. The *praenitida* specimens have narrow, delicate bullae lining the sutures, which show their descent from *Globigerinita parkerae* (Blow, 1969), and the sutural supplementary apertures characteristic of *C. nitida* are not well developed. Their presence at this site may be due to the superior preserva-

Table 4. Planktonic foraminifer datums, absolute ages, and depths at Site 1000.

Event	Zone (base)	Age (Ma)	Core, section, interval (cm)	Depth (mbsf)
Hole 1000A:				
LO *Globigerinoides fistulosus*		1.7	4H-CC to 5H-CC	36.55
FO *Truncorotalia truncatulinoides*	N22	2.0	4H-CC to 5H-CC	36.55
LO *Menardella exilis*		2.2	4H-CC to 5H-CC	36.55
LO *Menardella miocenica*		2.3	6H-CC to 7H-CC	55.55
Reappearance of *Pulleniatina* (Atlantic)		2.3	6H-CC to 7H-CC	55.55
LO *Menardella pertenuis*		2.6	6H-CC to 7H-CC	55.55
LO *Menardella multicamerata*		3.0	10H-CC to 11H-CC	93.55
LO *Dentoglobigerina altispira*		3.0	10H-CC to 11H-CC	93.55
FO *Menardella miocenica*	N21/N20	3.6	12H-CC to 13H-CC	112.55
LO *Hirsutella margaritae*		3.6	13H-CC to 14H-CC	122.05
LO *Globorotalia plesiotumida*		4.4	12H-CC to 13H-CC	112.55
FO *Menardella exilis*		4.5	15H-CC to 16H-CC	141.05
FO *Truncorotalia crassaformis*		4.7	15H-CC to 16H-CC	141.05
LO *Hirsutella cibaoensis*		5.0	16H-CC to 17H-CC	150.55
FO *Sphaeroidinella dehiscens*	N19	5.6	23H-CC to 24H-CC	217.05
FO *Hirsutella margaritae*		6.0	25H-CC to 26H-CC	236.05
FO *Globigerinoides conglobatus*		6.2	22H-CC to 23H-CC	207.55
FO *Hirsutella cibaoensis*		7.7	39X-CC to 40X-CC	365.70
FO *Globigerinoides extremus*		8.1	32H-CC to 33H-CC	302.55
FO *Candeina nitida*		8.1	32H-CC to 33H-CC	302.55
FO *Globorotalia plesiotumida*	N18/N17	8.2	35X-CC to 36X-CC	327.30
FO *Neogloboquadrina acostaensis*	N16	10.0	38X-CC to 39X-CC	356.30
LO *Paragloborotalia mayeri*	N15	10.3	39X-CC to 40X-CC	365.70
FO *Globoturborotalita nepenthes*	N14	11.4	41X-CC to 42X-CC	384.90
LO *Fohsella fohsi*	N13	11.8	42X-CC to 43X-CC	394.55
FO *Fohsella fohsi robusta*		12.3	45X-CC to 46X-CC	423.45
FO *Fohsella fohsi*	N12	12.7	50X-CC to 51X-CC	471.50
FO *Fohsella praefohsi*	N11	14.0	54X-CC to 55X-CC	510.00
Hole 1000B:				
FO *Fohsella peripheroacuta*	N10	14.8	4R-CC to 5R-CC	527.60
FO *Orbulina suturalis*	N9	15.1	4R-CC to 5R-CC	527.60
FO *Praeorbulina circularis*		16.0	5R-CC to 6R-CC	537.15
FO *Praeorbulina glomerosa*		16.1	6R-CC to 7R-CC	546.75
FO *Praeorbulina sicana*	N8	16.4	10R-CC to 12R-CC	590.05
LO *Catapsydrax dissimilis*	N7	17.3	15R-CC to 16R-CC	633.40

Notes: FO = first occurrence, LO = last occurrence. This entire table also appears on CD-ROM (back pocket).

tion of these delicate specimens at this shallow depth, to ecological factors related to the shallow depth, or merely to aliasing by the coarse resolution of shipboard biostratigraphy.

Samples 165-1000A-36X-CC and 37X-CC are attributable to upper Miocene Zone N16, but they also include elements of Zone N14. As in Sample 165-1000B-1R-CC described above, the sediment is difficult to disaggregate and includes numerous benthic foraminifers. In addition, the reworked planktonic foraminifers (mostly *Paragloborotalia mayeri*) seem well preserved.

Because of the high sedimentation rates and generally good foraminiferal preservation, identification of the remaining Miocene zones was refreshingly straightforward at Site 1000. The base of Zone N16 is marked by the FO of *Neogloboquadrina acostaensis* between Samples 165-1000A-38X-CC and 39X-CC. The base of Zone N15 is marked by the LO of *Paragloborotalia mayeri* between Samples 165-1000A-39X-CC and 40X-CC. The base of Zone N14 is below the FO of *Globorotalites nepenthes* between Samples 165-1000A-41X-CC and 42X-CC. It was not possible to delimit the bases of Zones N16 and N14 at Sites 998 and 999.

The evolutionary history of the *Fohsella* group is well represented in the relatively expanded section at Site 1000, but their stratigraphic interval is divided between Holes 1000A and 1000B. Zones N10 through N13 were readily documented. The LO of *Fohsella fohsi* places the base of Zone N13 between Samples 165-1000A-42X-CC and 43X-CC. One result of the good preservation and high middle Miocene sedimentation accumulation rates at Site 1000 is the delimitation of the FO of *Fohsella fohsi robusta* datum between Samples 165-1000A-45X-CC and 46X-CC with Zone N12. The base of Zone N12 is marked by the FO of *F. fohsi* between Samples 165-1000A-50X-CC and 51X-CC. The base of Zone N11 is located between Samples 165-1000A-54X-CC and 55X-CC at the FO of *Fohsella praefohsi.* Finally, the FO of *Fohsella peripheroacuta* marks the base of Zone N10 between Samples 165-1000B-4R-CC and 5R-CC.

The FO of *Orbulina suturalis* places the base of Zone N9 between Samples 165-1000B-4R-CC and 5R-CC. At Sites 998 and 999, *Orbulina* first occurred in the *Fohsella* interval. Its relatively deeper occurrence suggests that the high "first" occurrences at the other sites were caused by poorer preservation at greater water and sediment burial depths. High sediment accumulation rates at Site 1000 make the subdivision of Zone N8 with successive praeorbuline events possible. The FO of *Praeorbulina sicana* defines the base of Zone N8 as between Samples 165-1000B-10R-CC and 12R-CC. The base of Zone N7 is marked by the LO of *Catapsydrax dissimilis* between Samples 165-1000B-15R-CC and 16R-CC. The remainder of the recovered record at Hole 1000B was assigned to Zone N6/N5 because *Globigerinatella insueta* s.s. ranged to the base of the hole and *Paragloborotalia kugleri* was not found.

PALEOMAGNETISM

Whole- and Split-Core Measurements

The remanent magnetization of the archive-half sections of APC and XCB cores from Hole 1000A and RCB cores from Hole 1000B were measured using the pass-through cryogenic magnetometer at 10-cm intervals. After measuring the natural remanent magnetization (NRM), the sections were partially demagnetized in peak alternating fields (AF) of either 15 mT for the interval 0–270 mbsf, or 20 mT for the interval 270–692 mbsf.

The NRM inclinations are strongly biased toward high positive inclinations (50°–80°), and are inconsistent with both the present-day geomagnetic field inclination (46°) and the expected axial dipole inclination (29°) for the latitude of the site. The observed directions indicate that a strong drilling-induced magnetization is present, as previously identified at Sites 998 and 999. The AF demagnetization removes a significant portion of the secondary overprint, but the overprint is only sufficiently removed to provide interpretable directional data in the interval 0.0–22.5 mbsf. Only one polarity transition, the C1n to C1r transition at 20.39 mbsf, is clearly recorded in this interval. The assignment of this chron boundary is consistent with its occurrence in the equivalent of $\delta^{18}O$ Stage 19, which has been identified in the magnetic susceptibility record (Fig. 7).

The NRM intensities (Fig. 19) range from 10 to 37 mA/m within the top 20 mbsf and decrease abruptly at ~22.5 mbsf to values of 2–3 mA/m. Intensity values of less than 5 mA/m characterize the rest of the section, with the exception of discrete ash layers that have values of up to 40 mA/m. Below 545 mbsf, even discrete ash layers have intensities of less than 10 mA/m and are highly pyritized.

Reductive Diagenesis

The magnetic record of Site 1000 represents a textbook example of reductive diagenesis in which a ferrimagnetic iron oxide (i.e., Fe_3O_4, magnetite) is reduced to a nonmagnetic iron sulfide (i.e., FeS_2, pyrite) during the oxidation of organic matter by microorganisms. For example, both the intensity of magnetization and the low-field susceptibility decrease abruptly at ~22.5 mbsf in an interval where the concentration of pore-water sulfate is also rapidly decreasing (Fig. 19). Previous studies (Channell and Hawthorn, 1990; Leslie et al., 1990) have shown that an abrupt decrease in indicators of magnetic mineral concentration (in this case, intensity of magnetization and low-field susceptibility), in conjunction with a similar decrease in pore-water sulfate concentrations, are strong indicators of the process of reductive diagenesis. In addition, Robinson (1990) has shown that reductive diagenesis can be detected using a scatter plot of susceptibility vs. percent carbonate.

A strong inverse relationship between susceptibility and percent carbonate can usually be found in carbonate-rich sediments that are not subject to reductive diagenesis, whereas low to negative susceptibility values and the absence of a significant inverse relationship characterize sediments that have undergone reductive diagenesis (Robinson, 1990). The scatter plot of susceptibility vs. percent carbonate for Site 1000 (Fig. 20) shows two distinct regimes: (1) an interval not subject to reductive diagenesis from 0 to 20 mbsf and (2) an interval that has undergone reductive diagenesis below 20 mbsf. The step in the susceptibility profile observed at ~22.5 mbsf reflects the pyritization of ferrimagnetic iron oxides and should not be interpreted as a change in either terrigenous clay or ash flux in Site 1000.

Discrete ash layers, which provided reliable paleomagnetic results from Site 999 (see "Paleomagnetism" section, "Site 999" chapter, this volume) in intervals where the background lithology was not as reliable, are severely reduced in Site 1000, and will not produce reliable paleomagnetic results in shore-based studies.

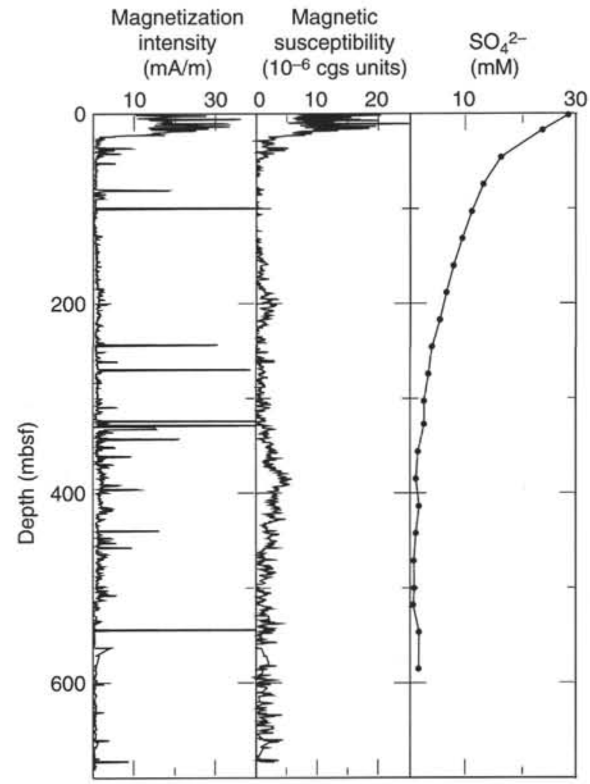

Figure 19. NRM intensity, magnetic susceptibility, and pore-water sulfate concentration profiles for Site 1000.

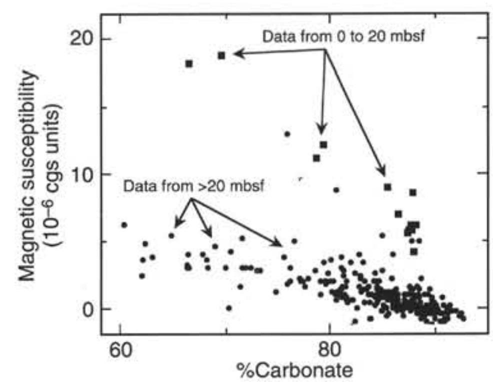

Figure 20. Comparison of magnetic susceptibility to percent carbonate for Site 1000.

SEDIMENTATION AND MASS ACCUMULATION RATES

Discrepancies between the nannofossil and planktonic foraminifer biostratigraphic schemes made determination of sedimentation rates more problematic at Site 1000 than at previous Leg 165 sites. The age vs. depth relationships in the planktonic foraminifer datum events are not as internally consistent as those of the nannofossil events. This may be because certain foraminiferal datums are diachronous between Site 1000 and other sections, or more likely because the foraminiferal biostratigraphy is only based on one sample per core. We decided to calculate sedimentation rates based on age vs. depth relationships for nannofossil datums only (Fig. 21).

To compare Site 1000 results with Sites 998 and 999, the same nannofossils datums have been used as break points in the curve at all sites (Fig. 22). Sedimentation rates are greatest (~47 m/m.y.) at Site 1000 between 9.6 and 13.5 Ma in the Miocene; moderate (~37 m/m.y.) between 2.8 and 9.6 Ma in the mid-Pliocene and late Miocene; and low (~27 m/m.y.) in the late Pliocene–Pleistocene and in the early to middle Miocene.

The nannofossil data suggest three breaks in slope to yield four segments of essentially constant sedimentation rate (Fig. 22). Between 0 and 77 mbsf, the sedimentation rate averages 27.3 m/m.y. This interval includes the Pleistocene and upper Pliocene, and it is delimited at the bottom by the last occurrence of *Discoaster tamalis* (2.8 Ma). The second segment, which spans the mid-Pliocene to the upper Miocene, has an average sedimentation rate of 37.2 m/m.y. The bottom of this interval is delimited by the top of the range of *Discoaster hamatus* (9.6 Ma) at 311 mbsf.

The third segment extends through the middle Miocene and includes the carbonate crash. Its average sedimentation rate, 47.0 m/m.y., is the highest recorded at Site 1000. The base of this interval is marked by the top of the range of *Sphenolithus heteromorphus* (13.5

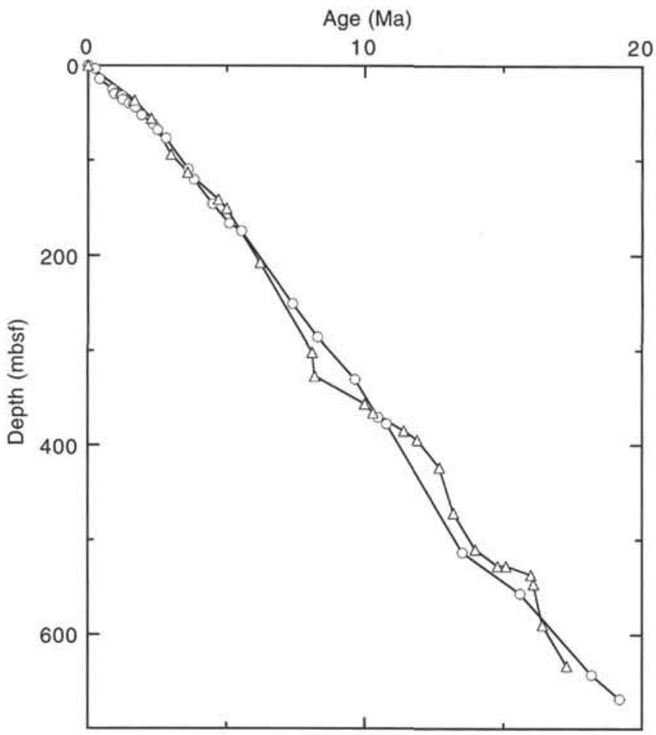

Figure 21. Age vs. depth relationships for planktonic foraminifer (triangles) and nannofossil (open circles) datums at Site 1000.

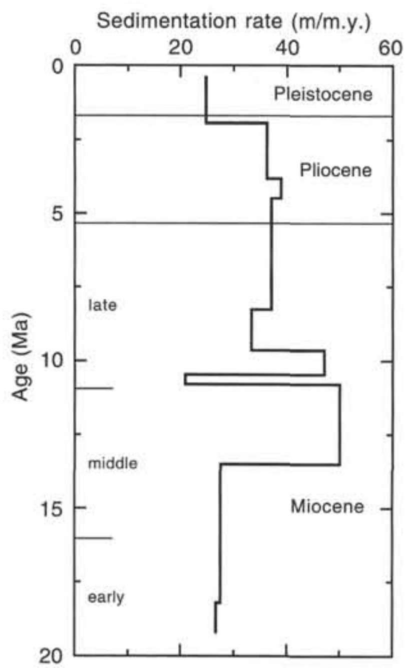

Figure 22. Sedimentation rates vs. age at Site 1000, using the same nannofossil datums that were used at Sites 998 and 999.

Ma) at 513 mbsf. Finally, the fourth segment has an average sedimentation rate of 27.3 m/m.y. and extends down into the lower Miocene to the base of the range of *Sphenolithus belemnos* (19.2 Ma) at 669 mbsf.

The average sedimentation rates that were calculated through the above intervals are used to derive mass accumulation rates (MARs) of carbonate, noncarbonate, and bulk sediments vs. depth (Figs. 23–26; Table 5). Noncarbonate MARs at Site 1000 (Figs. 24, 26) in-

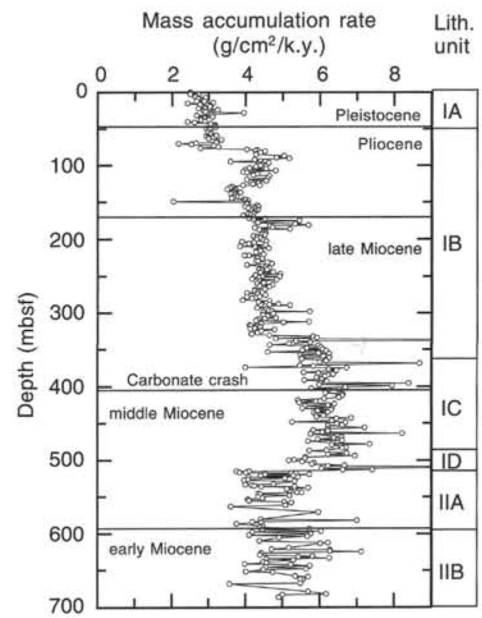

Figure 23. Bulk sediment mass accumulation rates vs. depth at Site 1000. Lithologic unit boundaries are shown on the right (see "Lithostratigraphy" section, this chapter).

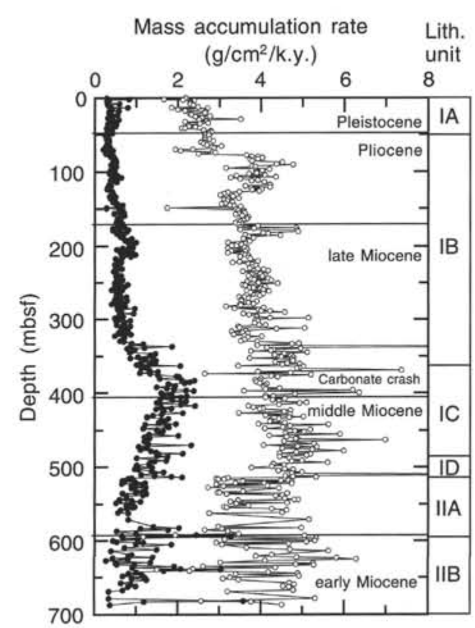

Figure 24. Mass accumulation rates of carbonate (open circles) and noncarbonate (solid circles) components vs. depth at Site 1000. Lithologic unit boundaries are shown on the right (see "Lithostratigraphy" section, this chapter).

crease steadily from the bottom of the section to a peak at ~380 mbsf (~11 Ma), which corresponds to the level that has been labeled the carbonate crash at this and other Leg 165 sites. Noncarbonate MARs then decline upsection to a low at ~230 mbsf (~6.5 Ma). After a brief reversal between 230 and 200 mbsf, noncarbonate MARs generally decline to the top of the section.

Carbonate MARs essentially parallel the record of noncarbonate MARs, except in three intervals. Between 450 and 380 mbsf (12.8–10.8 Ma), the two records gradually converge, culminating in the carbonate crash. Higher in the section, there are two episodes of increased carbonate MARs that have no counterpart in the noncarbon-

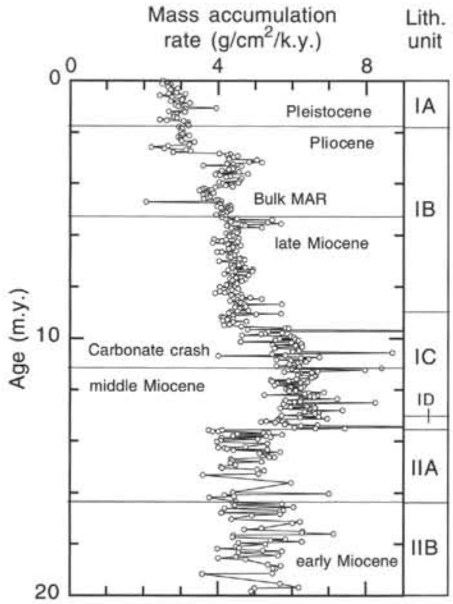

Figure 25. Bulk sediment mass accumulation rates (MAR) vs. age at Site 1000.

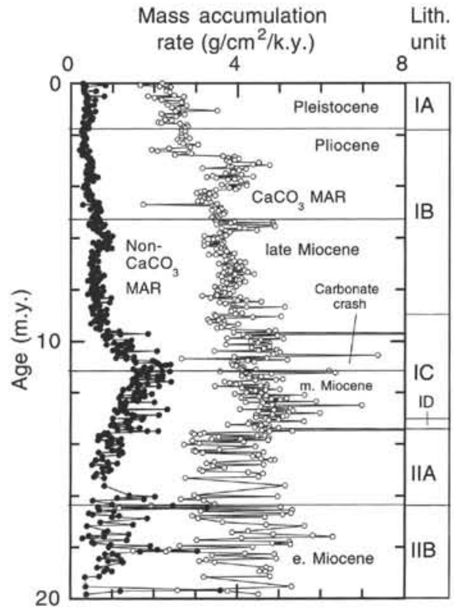

Figure 26. Mass accumulation rates (MAR) of carbonate (open circles) and noncarbonate (solid circles) fraction vs. age at Site 1000.

ate record. There is a sharp peak in carbonate MARs centered at ~180 mbsf in the uppermost Miocene section (~5.5 Ma) and a broader peak in the Pliocene centered at 100 mbsf (~3.5 Ma). The bulk MAR record (Fig. 23) is dominated by the carbonate component, and largely follows the trends of carbonate MARs. The bulk MAR record illustrates well the gradual decrease upsection in the amplitude of sample-to-sample variation.

ORGANIC GEOCHEMISTRY

Introduction

Concentrations of inorganic carbon ($CaCO_3$) were measured at a frequency of typically one sample per section for each core collected in Holes 1000A and 1000B. Departures from this sampling protocol occurred at intervals of critical interest, including the middle/late Miocene carbonate minimum, where two to three samples were analyzed per section. Values of total organic carbon (TOC) were determined for approximately one sample per core for the upper and lower portions of Hole 1000A. At intermediate depths and for all of Hole 1000B, samples were analyzed from approximately every other core. Concentrations of total nitrogen (N_T) and total sulfur (S_T) were generated in conjunction with the analysis of total carbon. Rock-Eval pyrolysis was performed on a selected suite of samples to constrain further the character of the organic fraction. Finally, in compliance with drilling safety requirements, headspace gases were analyzed at a rate of one sample per core. Analytical details are discussed in the "Organic Geochemistry" section of the "Explanatory Notes" chapter (this volume).

Despite gross similarities between the diagenetic profiles of Site 1000 and those of Sites 998 and 999, the sediments at Site 1000 are characterized by anomalous enrichments in organic carbon, including an interval spanning approximately 400–500 mbsf that yielded TOC values approaching 0.8 wt% and headspace gases containing C_1–C_5 hydrocarbons at concentrations that range up to several tens of parts per million (ppm). This zone of enrichment is coincident with the carbonate minimum and marks the transition from chalky sediment to well-lithified limestone (carbonate crash; see "Lithostratigraphy" section, this chapter). We hypothesize that the externally derived organic compounds result from updip and upsection migration of thermogenic hydrocarbons. The elevated clay content of the carbonate minimum may serve to inhibit further upward migration. The zone of hydrocarbon enrichment is characterized by enhanced redox diagenesis, including significant sulfate reduction. The concomitant increase in alkalinity associated with anaerobic respiration may facilitate precipitation of the carbonate cements that define the transition from chalk to limestone.

Concentrations of Inorganic and Organic Carbon, Total Nitrogen, and Total Sulfur

Results of $CaCO_3$, TOC, N_T, and S_T analysis are provided in Table 6 (see also Figs. 27, 28). The genetic implications of the $CaCO_3$ data, particularly with regard to the Miocene carbonate minimum, are discussed in detail in the "Lithostratigraphy" section of this chapter. Additional details are provided in the site chapters for Sites 998 and 999. The upper 170 mbsf at Site 1000 are characterized by extreme depletions in organic carbon, with the majority of the data falling at or below analytical resolution (Fig. 27). However, the sediments below 170 mbsf in Hole 1000A show pronounced enrichments in TOC, with the suggestion of an overall downcore increase that extends to ~400 mbsf and values that remain comparatively high to ~550 mbsf. The mean TOC value over this interval is 0.35 ± 0.22 wt%, with maximum values approaching 0.8 wt%. Corrections for the effects of carbonate dilution do not change significantly the overall downcore trend for TOC, which reflects, in part, the consistently very carbonate-rich nature of these sediments. Trends for TOC below 500 mbsf in Hole 1000B show relatively high values that extend downcore to approximately 550 mbsf (Table 6). With the exception of an apparent enrichment at ~650 mbsf, TOC values below 550 mbsf are on the order of 0.1 wt% or less. The concentrations of TOC at Site 1000 for the interval ranging from ~200 to 550 mbsf are elevated relative to those typical of Sites 998 and 999. These TOC "enrichments" are consistent with the comparatively high uranium concentrations inferred from downhole natural gamma-ray measurements (see "Downhole Measurements" section, this chapter).

The patterns of TOC distribution displayed in Figure 27 suggest a possible relationship between deposition of organic matter and bulk detrital sediment. Specifically, TOC values are elevated within the

Table 5. Interpolated ages and mass accumulation rate data from Site 1000.

Core, section, interval (cm)	Depth (mbsf)	Age (Ma)	DBD (g/cm^3)	LSR (cm/k.y.)	Bulk MAR ($g/cm^2/k.y.$)	$CaCO_3$ (wt%)	$CaCO_3$ MAR ($g/cm^2/k.y.$)	Noncarbonate MAR ($g/cm^2/k.y.$)
165-1000A-								
1H-1, 32–34	0.30	0.01	0.91	2.73	2.50	87.88	2.19	0.30
1H-2, 32–34	1.80	0.07	0.92	2.73	2.51	66.47	1.67	0.84
1H-3, 32–34	2.93	0.11	0.91	2.73	2.49	85.47	2.13	0.36
2H-1, 32–34	3.59	0.13	0.99	2.73	2.71	88.21	2.39	0.32
2H-2, 32–34	5.10	0.19	0.97	2.73	2.65	87.47	2.32	0.33
2H-3, 32–34	6.60	0.24	0.96	2.73	2.63	87.71	2.30	0.32
2H-4, 32–34	8.10	0.30	1.06	2.73	2.90	79.38	2.30	0.60
2H-5, 32–34	9.61	0.35	0.99	2.73	2.70	87.80	2.37	0.33
2H-7, 32–34	12.61	0.46	1.05	2.73	2.87	86.55	2.48	0.39
3H-1, 32–34	13.10	0.48	0.98	2.73	2.66	69.56	1.85	0.81

Notes: DBD = dry-bulk density, LSR = linear sedimentation rate, MAR = mass accumulation rate.

Only part of this table is produced here. The entire table appears on CD-ROM (back pocket).

Table 6. Concentrations of inorganic carbon, calcium carbonate, total carbon, total organic carbon, total nitrogen, and total sulfur, Holes 1000A and 1000B.

Core, section, interval (cm)	Depth (mbsf)	C_{inorg} (wt%)	$CaCO_3$ (wt%)	Total C (wt%)	TOC (wt%)	Total N (wt%)	Total S (wt%)
165-1000A-							
1H-1, 30–31	0.30	10.55	87.9				
1H-2, 30–31	1.80	7.98	66.5				
1H-3, 31–32	2.93	10.26	85.5	10.14	0.00	0.08	0.13
2H-1, 29–30	3.59	10.59	88.2				
2H-2, 30–31	5.10	10.50	87.5				
2H-3, 30–31	6.60	10.53	87.7	10.49	0.00	0.10	0.05
2H-4, 30–31	8.10	9.53	79.4				
2H-5, 31–33	9.61	10.54	87.8				
2H-6, 31–32	11.11	9.19	76.6				
2H-7, 31–32	12.61	10.39	86.5				

Notes: Data are reported as weight percent (wt%). C_{inorg} = inorganic carbon, $CaCO_3$ = calcium carbonate, TOC = total organic carbon.

Only part of this table is produced here. The entire table appears on CD-ROM (back pocket).

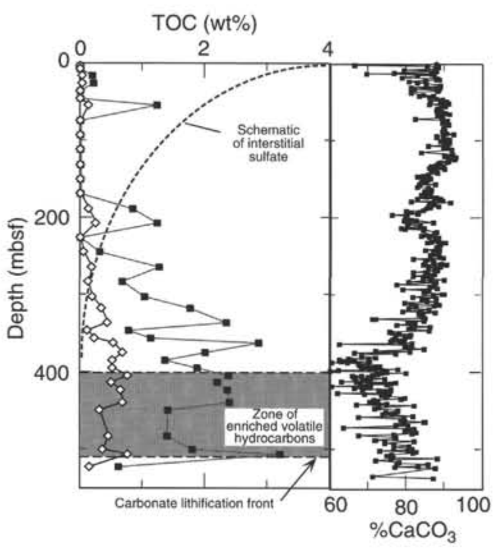

Figure 27. Downcore distribution of total organic carbon (TOC) for Hole 1000A reported as weight percent on a total sediment basis (open diamonds) and as a percentage of the noncarbonate fraction (solid squares). A schematic of the interstitial sulfate profile has been included for comparison (see Fig. 30 for the actual profile). Concentrations of calcium carbonate ($CaCO_3$) over the same interval and the stratigraphic position of the hydrocarbon-enriched zone are also included (see text for discussion).

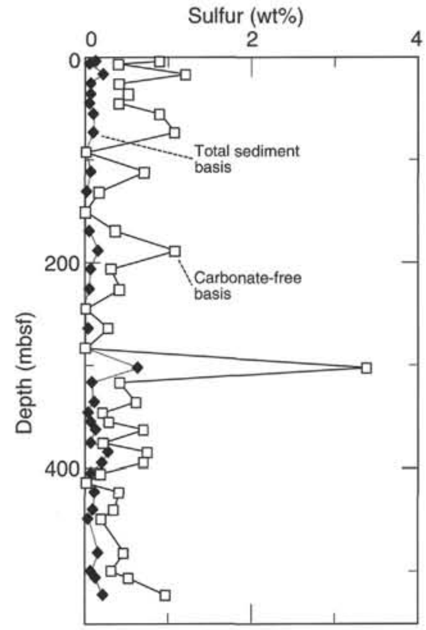

Figure 28. Downcore distribution of total sulfur concentrations for Hole 1000A reported as weight percent on a total sediment basis (solid diamonds) and as a percentage of the noncarbonate fraction (open squares).

general region of the carbonate minimum, between ~360 and 510 mbsf, and then decrease with scatter in an upcore direction to about 170 mbsf. Above 170 mbsf, essentially null levels are maintained to the top of the core. Furthermore, TOC values show a general decrease below the carbonate minimum (>~510 mbsf) (Table 6).

The pattern for TOC is similar to that observed for mass accumulation rates for the noncarbonate sediment fraction (see "Sedimentation and Mass Accumulation Rates" section, this chapter). This apparent coupling between the fluxes of terrigenous sediment and organic carbon persists when the TOC data are normalized to a noncarbonate basis (compare wt% calcium carbonate vs. TOC as expressed on a carbonate-free basis), indicating that the effects of carbonate dilution are not a factor (Fig. 27). A dominant terrigenous source of organic matter (i.e., terrestrial organic matter) is consistent with the results from Rock-Eval pyrolysis discussed below.

Concentrations of total sulfur (S_T), although still low, are generally higher than those observed at Sites 999 and 998 (Fig. 28). In the absence of detailed speciation results, the data for S_T are assumed to represent pyrite-S, a reasonable conclusion given the likely absence of significant acid-volatile sulfide, intermediate sulfur species, organic S, and solid-phase sulfates. Despite the likelihood of carbon-limited pyrite formation, the concentrations of pyrite-S in the upper ~500 mbsf at Site 1000 are decoupled from the reservoir of TOC (r^2 = 0.002 when evaluated on a carbonate-free basis to preclude the effects of carbonate dilution). Although not likely a factor at Site 1000, shore-based studies will address the possible role of Fe limitation during iron sulfide precipitation in these carbonate-rich sediments. Figure 28 highlights the largely scattered nature of the distribution of pyrite in the Hole 1000A sediments. Visual evaluations revealed megascopic evidence for significant, but heterogeneous, concentrations of pyrite in these sediments (see "Lithostratigraphy" section, this chapter). The mottled to nodular aspect of the iron sulfide enrichments in these sediments suggest burrow-controlled mineralization. Sulfur concentrations below ~500 mbsf (Hole 1000B) are uniformly low (Table 6).

Volatile Hydrocarbons

Unlike the sediment at Sites 998 and 999, analyses of headspace gases at Site 1000 revealed enrichments in volatile hydrocarbons. Samples from Hole 1000A yielded methane concentrations at or near trace levels to a depth of ~400 mbsf. However, beginning at ~404 mbsf and extending to a depth of ~520 mbsf, C_1 through C_{6+} hydrocarbons were present in the headspace gases at concentrations ranging from trace levels to several tens of ppm. This zone of volatile enrichment is summarized in Figure 29. At greater depths (i.e., in Hole 1000B), headspace methane was present at levels ranging from ~6 to 16 ppm, with one elevated value of 35 ppm at the base of the hole. Additional hydrocarbon gases were not observed. The zone of "hydrocarbon enrichment" was viewed with great interest. As discussed below, the enriched zone is dominated by the accumulation of thermogenic gases that migrated to their present site of accumulation. In situ production is unlikely despite the associated elevated levels of TOC.

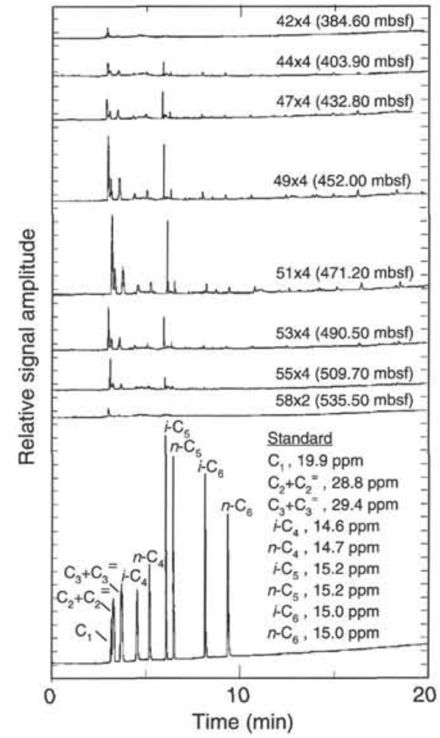

Figure 29. Chromatogram composite from the zone of volatile hydrocarbon enrichment. Data from over- and underlying hydrocarbon-depleted zones have been included for comparison. Approximate concentrations can be inferred by comparing signal amplitudes (peak heights) of the sample intervals to those of the standard. Vertical scales are constant, and a linear correspondence between the unknowns and the standard can be assumed for a given hydrocarbon.

Rock-Eval Pyrolysis

In general, detailed interpretations of Rock-Eval data are unreliable for samples containing less than 0.5% TOC (Peters, 1986; see also Tissot and Welte, 1984). However, comparative pyrolysis was performed on a suite of samples with TOC concentrations ranging from 0.00 to 0.76 wt% (Table 7). In part, the goal was to estimate the distribution of bitumen or, more specifically, of solvent-extractable liquid hydrocarbons that are readily volatized below 300°C. Interestingly, TOC concentrations of only 0.3 wt% are considered the lower limit for carbonate-type source beds (Gehman, 1962; Tissot and Welte, 1984).

Concentrations of readily volatized hydrocarbons (the S_1 pyrolysis peak) occur at low levels, even within the zone of enriched headspace gases. Clearly, oil accumulations are not a likelihood in these sediments. The S_2 peak is an indication of the quantity of hydrocarbon-type compounds that are produced by the cracking of kerogen as the temperature of pyrolysis is increased to 550°C. This parameter is a measure of the quantity of hydrocarbon that could be produced with continued burial and thermal maturation. Given the overall low values for TOC, the levels of S_2 are predictably low.

The amount of CO_2 produced during pyrolysis of a given sample at temperatures up to 390°C is expressed as S_3. Specifically, S_3 is a measure of the amount of oxygen in the kerogen. This parameter, however, may be compromised in samples containing less than 0.5% TOC. Abundant carbonate phases within the sample present an additional complication. High concentrations of carbonate minerals, particularly high-Mg calcite and proto-dolomites, can break down at temperatures as low as 390°C (Krom and Berner, 1983). The persistence of metastable carbonate phases to depth at Site 1000 suggest that carbonate contributions to the S_3 peak may be a factor (see "Lithostratigraphy" section, this chapter). This concern is corroborated by the presence of a significant S_3 peak, in association with the TOC-deficient sample from Core 165-1000A-59X (Table 7). Even with the contribution from the breakdown of carbonate, however, the organic matter at Site 1000 appears to be comparatively enriched in oxygen relative to hydrogen. This characteristic is diagnostic of terrestrially derived organic matter (type III kerogen). Despite the caveats associated with the generally low values of TOC, an overall oxygen-rich (terrestrial) nature of the organic matter is suggested by the ratio of S_2 to S_3 and by comparisons between the hydrogen index (HI; $100 \times S_2/TOC$) and the oxygen index (OI; $100 \times S_3/TOC$) (Table 7; see Tissot and Welte, 1984, for further details).

Finally, T_{max} is the temperature at which the maximum release of hydrocarbons occurs as a result of kerogen cracking during pyrolysis (i.e., the S_2 maximum). The low values observed for Site 1000 suggest that the kerogen is immature with regard to the production of both oil and gas by way of thermal degradation (Table 7). This conclusion is further supported by the generally low values reported in Table 7 for the productivity index (PI), which is expressed simply as $S_1/(S_1 + S_2)$. Despite the stratigraphic correspondence between the elevated levels of TOC and the zone of enriched hydrocarbons, there is not a direct genetic link. The shallow burial and the absence of an anomalously high thermal gradient (see "Downhole Measurements" section, this chapter), in combination with the combined proxies for thermal maturity, argue against indigenous gas enrichments and favor migration to the site of present accumulation. Specifically, updip and upsection migration from the adjacent thick stratigraphic sequence found to the southeast (south of Pedro Bank) is a reasonable explanation, including the possibility of upward movement along high-angle faults. Lithologies that are comparatively enriched in TOC, but contain low levels of methane as the only volatile hydrocarbon, are found immediately adjacent to the hydrocarbon zone de-

Table 7. Rock-Eval pyrolysis data for a selected group of samples from Hole 1000A.

Core, section, interval (cm)	Depth (mbsf)	T_{max} (°C)	S_1 (mg HC/g rock)	S_2 (mg HC/g rock)	S_3 (mg CO_2/g rock)	PI	S_2/S_3	TOC (wt%)	TOC* (wt%)	HI	OI
165-1000A-											
23H-3, 32–33	206.12	416	0.06	0.11	1.40	0.37	0.07	0.24	0.13	46	583
33H-3, 58–59	301.38	418	0.01	0.02	0.93	0.50	0.02	0.19	0.23	11	489
35X-3, 27–28	316.17	408	0.03	0.21	1.27	0.12	0.16	0.34	0.16	62	374
37X-3, 29–30	335.39	418	0.02	0.31	1.36	0.06	0.22	0.44	0.31	70	309
39X-3, 31–32	354.61	388	0.10	0.19	1.56	0.36	0.12	0.23	0.04	83	678
40X-1, 31–32	361.21	423	0.05	0.52	1.28	0.09	0.40	0.53	0.31	98	242
42X-3, 29–30	383.39	394	0.04	0.13	1.59	0.25	0.08	0.51	0.32	25	312
44X-3, 108–109	403.48	422	0.07	1.02	1.56	0.06	0.65	0.75	0.76	136	208
46X-3, 31–32	421.91	423	0.05	1.01	1.46	0.05	0.69	0.64	0.55	158	228
49X-1, 27–28	447.77	402	0.09	0.38	1.57	0.20	0.24	0.31	0.19	123	506
52X-4, 31–32	481.11	410	0.03	0.39	1.40	0.07	0.27	0.45	0.43	87	311
54X-3, 31–32	498.91	422	0.06	0.48	1.03	0.11	0.46	0.35	0.44	137	294
55X-1, 28–29	505.48	414	0.06	0.87	1.75	0.07	0.49	0.76	0.52	114	230
56X-5, 31–32	521.11	353	0.04	0.07	1.05	0.40	0.06	0.14	0.13	50	750
59X-1, 33–34	544.03	ND	0.01	0.00	0.72	ND	0.00	0.00	0.00	ND	ND

Notes: Emphasis has been placed on samples with comparatively high TOC concentrations and from the general region of the hydrocarbon-enriched zone (see Fig. 29). Details regarding the method and the various parameters are available in the text and are discussed in the "Organic Geochemistry" section of the "Explanatory Notes" (this volume). PI = production index, HI = hydrogen index, and OI = oxygen index. ND = no data.

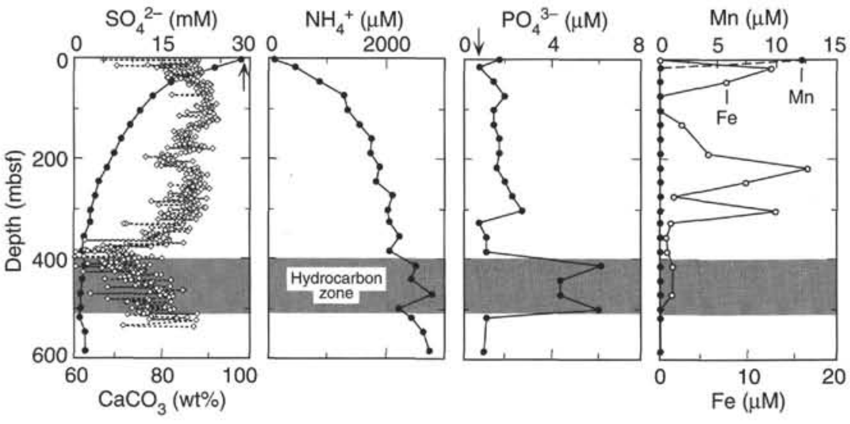

Figure 30. Downcore distributions of dissolved sulfate, ammonium, phosphate, manganese, and iron for Hole 1000A. Concentrations of calcium carbonate over the same interval and the stratigraphic position of the hydrocarbon-enriched zone have been included for comparison. Arrows indicate mean ocean-bottom-water compositions taken from Millero and Sohn (1992).

picted in Figures 27 and 29. This relationship argues against in situ generation of thermogenic gases and favors an interpretation of migration and trapping. Sulfate occurs at near-zero concentrations within the hydrocarbon zone, suggesting that bacterial methanogenesis may be a factor (Martens and Berner, 1974); however, thermogenesis must be invoked to explain the presence of C_{2+} hydrocarbons.

Redox Pathways

The downcore distributions of sulfate, ammonium, phosphate, Mn, and Fe are summarized in Figure 30. Given the strong link with regard to the ambient, organically mediated redox conditions, it is most effective to discuss these species within the context of organic geochemistry. Sulfate shows a remarkably smooth, systematic decrease to asymptotic values that approach zero by approximately 350–400 mbsf. This decrease in dissolved sulfate is more pronounced than those observed at Sites 998 and 999, which is consistent with the generally more reducing conditions at Site 1000. The overall reaction for dissimilatory sulfate reduction can be expressed as follows:

$$1/53(CH_2O)_{106}(NH_3)_{16}(H_3PO_4) + SO_4^{2-}\ 2HCO_3^-$$

$$+ HS^- + 16/53NH_3 + 1/53H_3PO_4 + H^+,$$

where the stoichiometry of sedimentary organic matter is simplified by assuming a Redfield C:N:P relationship.

As predicted from the above reaction, ammonium increases systematically downcore, showing a maximum where sulfate approaches null levels (Fig. 30). The high values of ammonium are consistent with the more reducing conditions at Site 1000, and the systematic downcore increase reflects an absence of the strong silicate-related overprint that characterized the ash-rich intervals at Sites 998 and 999. Ammonium concentrations increase slightly within the zone of volatile hydrocarbons, which likely reflects enhanced organic degradation.

Concentrations of dissolved phosphate are maintained at low levels by adsorption of phosphate onto surfaces of the abundant calcium carbonate within the host sediment (Walter and Burton, 1986). The phosphate maximum within the hydrocarbon zone may result from enhanced microbial oxidation of organic compounds, from slightly lower calcium carbonate concentrations within this region and, perhaps, from release from ferric oxides under conditions of elevated Fe reduction. Ferric oxides have a strong capacity to scavenge phosphate (Ruttenberg, 1992; Krom and Berner, 1980).

The vertical separation between the surficial maxima in dissolved Mn and Fe is consistent with the hierarchy of redox reactions often observed in suboxic deep-marine sediments (Froelich et al., 1979). The downcore decrease in Mn can be attributed to adsorption onto the carbonate host sediment. The observed decease in Fe is likely related to the precipitation of iron sulfides. The downcore maxima for dissolved Fe corresponds in a general way with enrichments in TOC and very subtle decreases in carbonate content, reflecting perhaps zones of slightly enhanced Fe reduction or the greater availability of detrital Fe oxides (oxyhydroxides).

Table 8. Interstitial water composition, Site 1000.

Core no.	Depth (mbsf)	pH	Alkalinity (mM)	Salinity (g/kg)	Cl^- (mM)	Na^+ (mM)	Mg^{2+} (mM)	Ca^{2+} (mM)	SO_4^{2-} (mM)	PO_4^{3-} (µM)	NH_4^+ (µM)	$Si(OH)_4$ (µM)	K^+ (mM)	Fe (µM)	Mn (µM)
165-1000A-															
1H	1.5	7.72	3.31	35	561	472	52.5	10.3	28.4	1.55	81	206	11.6	BDL	12
3H	17.04	7.44	7.08	35	553	493	50.4	7.81	23.8	0.62	438	240	11.6	12.62	BDL
6H	45.8	7.71	9.14	34	553	501	40.9	8.22	16.4	1.32	853	440	11.6	7.48	BDL
9H	74.3	7.15	10.41	34	559	487	37.0	9.08	13.3	1.78	1273	569	11.1	BDL	BDL
12H	102.8	7.58	10.86	34	565	524	34.6	9.4	11.2	1.32	1332	384	10.9	BDL	BDL
15H	131.3	7.00	10.56	34	562	521	33.9	10.5	9.54	1.32	1532	508	11.1	2.50	BDL
18H	159.8	6.99	11.97	33	564	506	31.9	10.7	7.93	1.55	1736	714	11.1	BDL	BDL
21H	188.3	7.04	11.38	33	561	484	29.0	10.4	6.67	1.55	1716	686	11.1	5.42	BDL
24H	216.8	7.25	11.18	33	557	511	27.8	10.5	5.51	1.43	1882	636	11.1	16.65	BDL
27H	245.3	7.55	12.13	33	569	488	26.2	11.0	4.11	1.78	1819	847	11.1	9.67	BDL
30H	273.8	6.97	10.41	33	587	488	24.7	10.8	3.51	2.13	2094	1099	10.9	1.57	BDL
33H	302.5	6.89	11.72	33	572	490	23.7	11.1	2.71	2.59	2009	980	10.3	13.08	BDL
36X	327.0	7.13	10.95	33	576	491	23.8	10.5	2.73	0.62	2051	532	10.1	1.27	BDL
39X	355.8	7.11	10.20	33	583	496	23.1	10.5	1.63	0.97	2224	490	10.1	0.76	BDL
42X	384.6	7.18	9.03	33	573	494	21.9	10.9	1.29	0.97	2051	490	9.68	0.80	BDL
45X	413.5	7.33	7.95	33	582	491	21.6	11.4	1.81	6.18	2488	712	9.51	1.47	BDL
48X	442.4	7.42	6.69	33	585	498	21.2	11.4	1.26	4.33	2421	753	9.57	BDL	BDL
51X	471.2	7.57	6.15	34	592	507	19.3	11.1	0.91	4.33	2781	606	10.2	1.35	BDL
54X	500.1	7.35	5.13	33.5	597	512	17.1	9.40	0.97	6.06	2202	593	10.3	BDL	BDL
165-1000B-															
4R	517.7	7.4	5.73	BDL	586	509	16.3	9.89	0.77	0.97	2421	634	11.0	BDL	BDL
7R	546.4	7.38	4.37	BDL	594	516	14.9	9.84	1.82	BDL	2622	636	11.5	BDL	
11R	584.9	7.58	4.11	BDL	596	524	12.7	8.75	1.74	0.85	2735	495	10.8	BDL	BDL

Notes: BDL = below detection limit. This entire table also appears on CD-ROM (back pocket).

Preliminary Model

The diagenetic pathways at Site 1000 are complex and not completely discernible within the context of shipboard analyses. Although details are lacking, the following empirical relationships speak profoundly to potential controls and mechanisms: (1) the near-zero asymptotic concentration of sulfate occurs precisely at the top of the carbonate minimum and roughly coincident with the top of the hydrocarbon zone (which is also characterized by increased concentrations in phosphate), (2) the hydrocarbon-enriched interval corresponds closely with the carbonate minimum, and (3) the base of the hydrocarbon zone and the approximate base of the carbonate minimum are coincident with the dramatic downcore transition from chalk to well-lithified limestone (see "Lithostratigraphy" section, this chapter). This lithologic transition is characterized by a sudden decrease in porosity (see "Physical Properties" section, this chapter).

The current working model, although conjectural, is based on the stratigraphic distribution of the features described above. First, it appears that diagenetic redox pathways are ostensibly decoupled from the inputs of TOC, which is consistent with an organic reservoir dominated by refractory, terrestrial (continental) organic matter. Second, it is reasonable that the volatile hydrocarbons are concentrated within the interval of minimum $CaCO_3$ concentrations as the increased clay content may act as a permeability seal that impedes further upward migration (the upper boundary of the carbonate minimum is not marked by a change in porosity; see "Physical Properties" section, this chapter). Furthermore, the stratigraphic correspondence between the sulfate minimum, the ammonium maximum, and the zone of hydrocarbon enrichment may record an interval of enhanced anaerobic respiration (e.g., sulfate reduction and methanogenesis). The resulting sulfate profile would reflect diffusional smoothing between the overlying seawater source and the reductive sink deep within the sediment column. Undoubtedly, sulfate reduction is also occurring within the upper portions of the section.

If the zone of hydrocarbons dominates the reductive pathways within the sediment, the concomitant production of alkalinity could facilitate the precipitation of carbonate cements as manifested in the transition from chalk to limestone. Shore-based petrographic and carbon isotopic studies will address this issue. If cementation is driven by bicarbonate production during oxidation of organic matter, the ^{13}C-depleted signal should be obvious. The model calls for an increase in alkalinity that drives carbonate supersaturation to levels in excess of those required to overcome the kinetic obstacles of nucleation. Once overcome, growth proceeds rapidly and likely gives rise to the Ca, Sr, and alkalinity profiles presented in the "Inorganic Geochemistry" section of this chapter. Ultimately, the lower portions of these profiles are dominated by precipitation and diffusion. The presence of well-cemented lithologies below, rather than within, the carbonate minimum are expected for substrate reasons—precipitation is favored by the absence of detrital contamination.

Clearly, details regarding the timing and mechanistic aspects of the model are lacking, but the striking correspondence of multiple geochemical and lithologic features is compelling. Remaining questions include those regarding the distribution of pyrite higher in the section. Might migration of hydrocarbons beyond the carbonate minimum have provided the electron donor for sulfate reduction in these regions? If so, does this explain the apparent relationship between pyritization and infaunal activity (i.e., a burrow-related permeability link)? Might the associated production of alkalinity favor the observed preservation of metastable carbonate phases (aragonite and Mg-calcite) to unusually great depths (see "Lithostratigraphy" section, this chapter)? Is the hydrocarbon zone truly a region of enhanced anaerobic respiration and, if so, why are enrichments in pyrite-S absent? To what degree do existing conditions, including the distribution of carbonate cements, reflect the long-term integrated redox history of the critical interval, as well as the entire sediment column? It is expected that a broad range of shore-based analyses will further constrain this model.

INORGANIC GEOCHEMISTRY

Interstitial Water Chemistry

Introduction

Twenty-two interstitial water samples were collected at Site 1000 at depths from 1 to 593 mbsf (Table 8). Analytical methods are detailed in the "Inorganic Geochemistry" section of the "Explanatory Notes" chapter (this volume). Samples were analyzed for pH, salinity, chlorinity, alkalinity, sulfate, phosphate, ammonium, silica, Na^+, Fe, Mn, Mg^{2+}, Ca^{2+}, K, Sr, Rb, and Li. Concentrations were not normalized to Cl^- concentration because of the small (~9% relative) variation in Cl^- abundance and the uncertainty concerning the conservative behavior of Cl^- throughout the section. Data for volcanic ash

Table 8 (continued).

Core no.	Depth (mbsf)	Sr (μM)	Rb (μM)	Li (μM)
165-1000A-				
1H	1.5	158	2.61	28
3H	17.04	615	2.29	38
6H	45.8	1191	2.38	50
9H	74.3	1340	2.45	61
12H	102.8	1509	2.71	93
15H	131.3	1771	2.93	125
18H	159.8	1986	3.18	162
21H	188.3	2239	3.39	200
24H	216.8	2005	3.54	238
27H	245.3	2029	3.76	270
30H	273.8	3203	4.22	308
33H	302.5	3428	4.12	343
36X	327.0	3399	3.79	348
39X	355.8	3250	3.90	370
42X	384.6	2960	3.95	395
45X	413.5	2819	3.98	407
48X	442.4	2520	4.35	398
51X	471.2	2510	5.48	396
54X	500.1	2370	5.79	369
165-1000B-				
4R	517.7	2407	6.12	346
7R	546.4	2192	6.52	287
11R	584.9	2014	6.99	223

thickness, degree of alteration, mineralogy, and frequency (see "Igneous Petrology and Volcanology" section, this chapter) are used to evaluate the relationship between ash distributions and downcore geochemical trends in both pore waters and sediments. Reference seawater values are plotted as arrows on the axes of the various diagrams; these values are derived from mean ocean-bottom-water compositions (Millero and Sohn, 1992).

pH, Salinity, Sodium, and Chlorinity

Values of pH range from 7.72 to 6.89, initially decreasing with increasing depth to a minimum at ~300 mbsf and then increasing again. Considerable variability that does not correlate with other parameters is superimposed on these gross trends. Salinity values closely resemble seawater over much of the profile, and perhaps show a slight overall decrease with depth (Table 8). Chloride concentrations show an overall increase with depth from values similar to those of bottom water, to 595 mM (Fig. 31). The cause of the various fluctuations is not presently clear, although a pronounced decrease at 510 mbsf (the transition from chalk to limestone) mirrors variations observed in other chemical profiles. Sodium appears decoupled from Cl^- in the upper 300 m of the section (Fig. 31), but it begins to follow the variations in Cl^- in the lower part of the profile. The variability of Na^+ in the upper part of the profile is not reflected by variations in other cations at this site.

Sulfate, Ammonium, Iron, Manganese, and Phosphate

The behavior of dissolved sulfate, ammonium, Fe, Mn, and phosphate is discussed in relation to the accumulation and degradation of reactive organic matter in the "Organic Geochemistry" section (this chapter).

Alkalinity

Alkalinity shows a pronounced, asymmetrically convex profile characterized by a rapid increase in the upper 70–100 m of the section, an inflection at ~120–130 mbsf, and then a marked decrease from 300 mbsf downward (Fig. 32). The profile approaches an apparent steady-state concentration at its base of ~4 mM. Different aspects of the morphology of this profile can be attributed largely to the effects of carbonate equilibria in the upper and lower parts of the section. Although the initial rapid alkalinity increase in the upper parts of the section may be driven partially by degradation of reactive organic matter, other likely responses to this process (e.g., sulfate reduction and ammonium generation) do not exhibit marked inflections at the 120- to 130-m depth interval. We surmise that much of the initial increase in alkalinity at high stratigraphic levels is governed by dissolution of a carbonate phase, possibly aragonite and, to a lesser extent, high-Mg^{2+} calcite. This hypothesis is strengthened by the observed inflection of the alkalinity trend, coinciding precisely with the interval over which aragonite disappears from the solid phase (Fig. 32; see "Lithostratigraphy" section, this chapter). A similar inflection is seen in the Ca^{2+} profile (Fig. 33), indicating that the disappearance of aragonite stifles the generation of alkalinity and dissolved Ca^{2+}.

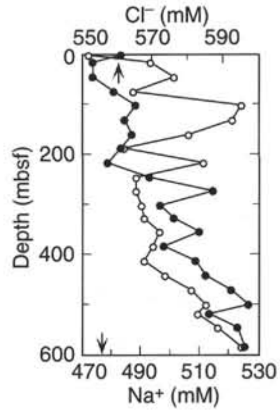

Figure 31. Depth profiles of Na^+ (open circles) and Cl^- (solid circles) in Site 1000 interstitial waters. Arrows indicate mean ocean-bottom-water composition taken from Millero and Sohn (1992).

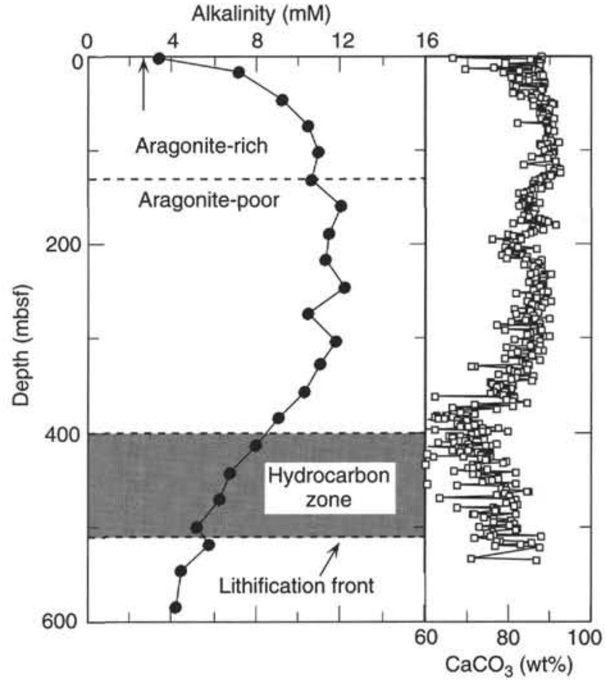

Figure 32. Alkalinity in Hole 1000A interstitial waters compared to bulk calcium carbonate contents of sediment (from Table 6). Arrow indicates mean ocean-bottom-water sulfate composition taken from Millero and Sohn (1992).

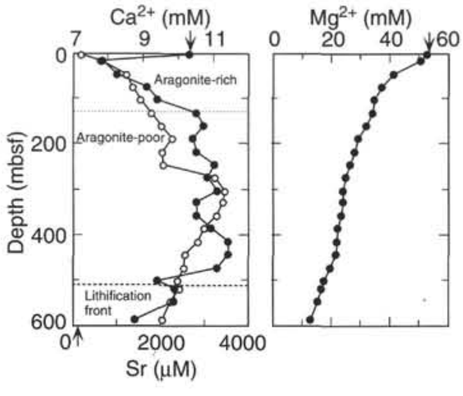

Figure 33. Depth profiles of Ca^{2+} (solid circles), Sr (open circles), and Mg^{2+} in Site 1000 interstitial waters. Arrows indicate mean ocean-bottom-water composition taken from Millero and Sohn (1992).

The systematic decrease of alkalinity with increasing depth below 200 mbsf is related to the pronounced lithification horizon at 510 mbsf (see "Lithostratigraphy" section, this chapter), marking the transition from chalk to limestone, which coincides abruptly with the alkalinity levels becoming asymptotic (Fig. 32). Carbonate precipitation and cementation at this lithification horizon is most likely responsible for the lower alkalinity. The shape of the profile below 200 mbsf is smoothed by diffusion driven by this sink. As noted in the "Organic Geochemistry" section (this chapter), the lithification horizon coincides with the base of a zone of enhanced hydrocarbon accumulation. We hypothesize that carbonate precipitation that was associated with lithification was induced by an initial alkalinity increase associated with degradation of the organic matter. Once initiated, carbonate precipitation proceeded to consume alkalinity and, together with the time-integrated effects of diffusion, reduced levels to those observed now. The low levels of organic matter presently available for bacteriogenic metabolism in the hydrocarbon horizon (<20 ppm) are unlikely to produce a detectable effect on the observed alkalinity profile. Thus, although the overall alkalinity profile is dominated by carbonate equilibria, we invoke an integral genetic role for hydrocarbons in governing lithification and carbon speciation at depth.

Magnesium, Calcium, and Strontium

Magnesium concentrations decline steadily from those characteristic of seawater at the top of the section to ~12 mM in the lower part of the section (Fig. 33). Because igneous basement may lie at considerable depth beneath the putative carbonate platform, it appears likely that the decline in pore-water Mg^{2+} reflects the effects of dolomite precipitation throughout the section (as observed from XRD studies), combined with Mg-rich smectite formation associated with ash alteration.

Calcium and Sr profiles are more complex (Fig. 33). A sharp initial decrease in pore-water Ca^{2+} in the first 20 m of the section (Fig. 33) is probably a response to carbonate precipitation. This is also reflected in a dramatic decrease in Mn concentrations (see "Organic Geochemistry" section, this chapter) due to adsorption and crystal chemical effects. Ca^{2+} then sharply increases once more, probably because of the effects of carbonate dissolution. The sharp inflection in the Ca^{2+} profile at ~130–150 mbsf coincides with the disappearance of aragonite from the solid phase. Dolomite also disappears at this point and may thus influence the pore-water Ca^{2+} profile. Calcium levels remain slightly enriched over seawater values to ~500 mbsf, with minor variations perhaps reflecting the sporadic appearance of various carbonate phases downsection. The marked decrease in Ca^{2+} concentration at 500 mbsf is coincident with the diagenetic transition of chalk to limestone and likely reflects the carbonate precipitation invoked to explain the alkalinity profile.

A source-and-sink effect may also explain the Sr pore-water profile at Site 1000. Sr increases dramatically from the sediment-water interface to ~300 mbsf, the very high levels (>3000 µM) being consistent with the dissolution of Sr-rich aragonite. Sr enrichment continues to 300 mbsf, with the minor fluctuations being out of phase with Ca^{2+} variations. This may indicate that Ca^{2+} is more sensitive to the effects of high-Mg^{2+} calcite, aragonite, and dolomite solution equilibria, whereas Sr is dominated by the effects of aragonite (which tends to be greatly enriched in Sr compared to coexisting carbonates). The decrease in Sr from 300 mbsf toward the base of the sequence may be driven by carbonate cementation at depth and the reappearance of aragonite and dolomite in the solid phase, creating a Sr sink (see "Lithostratigraphy" section, this chapter).

Silica

Dissolved silica concentrations at Site 1000 increase from 200 µM at the sediment-water interface to >1100 µM at 300 mbsf (Fig. 34). The peak silica enrichment is coincident with the first major occurrence of ashes between 250 and 350 mbsf and declines sharply below that interval. This coincidence implicates weathering of reactive Si-rich volcanic glass and silicates as the dominant source of dissolved silica at these levels. We cannot resolve, however, whether there is an additional biogenic silica source whose dissolution itself may be inhibited by the elevated ash content of the sediment. Detrital quartz is too chemically inert to play any role in the dissolved silica budget. Minor fluctuations in the dissolved silica profile in the upper 350 m of the section are correlated with the effects of dispersed ash in the sediment, and both dispersed ash and discrete silicic ash layers may contribute to the dissolved silica budget. Below 400 mbsf, dissolved silica becomes largely decoupled from the effects of ash, and the concentration of dissolved silica actually decreases through the major Miocene ash interval at 500 mbsf. This decrease is caused by the appearance of opal-CT, which is a sink for pore-water silica, at 500 mbsf.

Rubidium, Potassium, and Lithium

The behavior of Rb in Site 1000 pore waters can be directly linked to the presence of siliceous, incompatible-element enriched ash layers (Fig. 35). Pore-water Rb concentrations most closely mirror the distribution of discrete ash layers rather than dispersed ash. Rb concentrations continue to increase through the interval of major Miocene ash deposition, indicating that any precipitation reactions associated with weathering mostly exclude Rb at this stratigraphic level in the profile.

In contrast to Rb, pore-water K concentrations appear largely independent of the distribution of ash in the upper 400 m of the section. Potassium concentrations decrease steadily in this upper region of the section, plateauing intermittently where significant dispersed ash appears between 150 and 300 mbsf. The K decrease may reflect ash-related weathering reactions not releasing as much K into solution as at other sites, or it may reflect the presence of a significant K sink at 350 to 400 mbsf that is not evident from observation or XRD analysis. Below 450 mbsf, dissolved K increases dramatically, presumably in response to the appearance of significant levels of ash in the sediment column.

Lithium variations in the pore waters of Site 1000 are distinct from those of the other alkali cations. Li concentrations increase monotonically from those characteristic of bottom water and reach more than ten times the enrichment at 450 mbsf. Concentrations then decrease downhole again. The overall profile is smoothly varying, perhaps betraying the effects of diffusion, and does not exhibit any of the localized responses evident in the K and Rb profiles. Dissolution of biogenic opal-A has been suggested as a significant source for dissolved Li in pore waters (Gieskes, 1983), and several studies have found close correspondence between dissolved Li and silica. No such

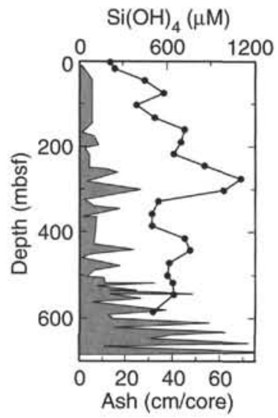

Figure 34. Depth profile of dissolved silica in Site 1000 interstitial waters. The thickness of ash layers (gray area) is also plotted.

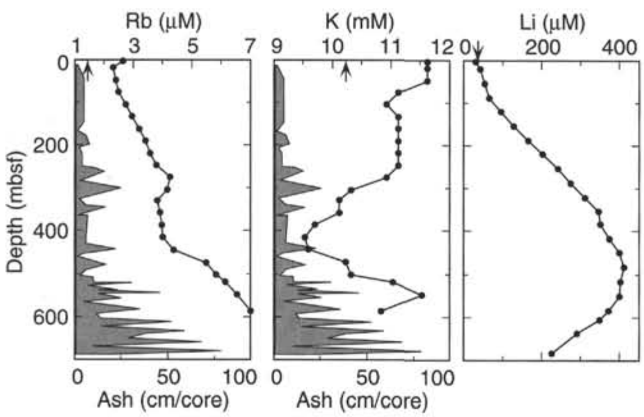

Figure 35. Depth profiles of Rb, K, and Li in Site 1000 interstitial waters. The thickness of ash layers (gray area) is also plotted. Arrows indicate mean ocean-bottom-water composition taken from Millero and Sohn (1992).

correlation is observed at Site 1000, or previous sites on this leg, indicating either that opal-A dissolution is unlikely to exert a dominant influence on dissolved Li in this environment or that diffusional and diagenetic reactions destroy any original relationship. Surprisingly, given the likely substitution of Li for K in biotite, Li does not respond more obviously to volcanogenic input from ash weathering. The smoothly varying Li profile indicates diffusionally smoothed source-sink behavior. It is possible that the Li profile is a time-integrated response to total dissolution of opal-A and possible Li uptake by a mineralogical sink. Partitioning of Li into clays produced by weathered ash at depth may sequester Li from solution (Steiness et al., 1972) and hence be a sink in this section.

Summary

At Site 1000, carbonate solution equilibria appear to dominate the pore-water chemistry, specifically, dissolution and precipitation reactions involving aragonite, high-Mg^{2+} calcite, and dolomite. The pore-water chemistry in the upper parts of the section are dominated by dissolution, which enhances alkalinity, Ca^{2+}, and Sr concentrations. Aqueous Sr concentrations are highly elevated, consistent with the solution of Sr-rich aragonite. A pronounced lithification horizon at 510 mbsf, manifest as the transition from chalk to limestone, appears to act as a sink for diffusive transfer of carbonate-related solutes. Alkali metals are less consistently dominated by the effects of silicic ash weathering compared with Sites 998 and 999.

Sediment Chemistry

Introduction

At Site 1000, the shipboard sediment chemistry program sampled sediment at a rate of one sample per every third core, and analyzed sediment through the entire recovered sequence. We targeted analysis of the interstitial water squeeze-cakes, which served to speed up the acquisition time because we did not have to wait for the cores to reach the sampling table before starting the sample preparation procedure. In several instances, we took additional discrete 10-cm^3 samples from particular intervals that visually appeared representative and had no obvious marker beds (i.e., discrete ash layers, turbidites, and other rapid/unusual events were avoided). The samples were analyzed as described in the "Explanatory Notes" chapter of this volume. A total of 27 sediment samples were analyzed. Sedimentary chemical data are presented in Tables 9 and 10.

Quantifying Sedimentary Components (Terrigenous Material and Dispersed Ash)

As at previous sites, the bulk sediment chemistry was used to quantify the relative amounts of terrigenous material and ash distributed through the sediment column. Although the frequency of ash layer occurrence has been described elsewhere (see "Igneous Petrology and Volcanology" section, this chapter), quantifying the amount of dispersed ash is particularly important to constrain diagenetic reactions, evaluate pore-water profiles, and define the sedimentologic nature of the recovered sequence.

We again quantified the terrigenous component by a normative calculation based on the concentration of Cr in a given sample and compared that to the concentration of Cr in average shale, according to:

$$(\%\text{Terrigenous})_{\text{sample}} = 100 \times (\text{Cr}_{\text{sample}}) / (\text{Cr})_{\text{avg shale}}.$$

We chose Cr as the reference element for the reasons outlined in the discussion of Site 999. As before, with the analytical detection limit of 3 ppm for Cr, the detection limit of the terrigenous calculation itself is slightly better than 3% (i.e., 3 ppm/110 ppm); this value also defines the amount of "noise" in the calculations and will prove critical in the discussion below.

The calculation of terrigenous material indicates that terrigenous matter accounts for ~5% of the bulk sediment from the seafloor to ~350 mbsf (Fig. 36). Below the carbonate minimum from 370 to 400 mbsf, the concentration of the terrigenous component increases to ~10%–15%. This increase in terrigenous matter is similar to the pattern observed at Site 999. Deeper in the hole, the terrigenous matter decreases to values <5% of the bulk.

At previous sites, we attributed the entire remaining component (i.e., noncarbonate and nonterrigenous) as reflecting the amount of dispersed ash; however, at Site 1000 we took a slightly more discriminating approach. Given the above calculation of the concentration of terrigenous material based on the Cr abundances, the remaining material—termed "residual"—was calculated by difference, according to:

$$(\%\text{Residual})_{\text{sample}} = 100 - \%\text{CaCO}_3 - \%\text{Terrigenous}.$$

Referring to the remaining material as "residual" is a nongenetic terminology. Plotting the downcore change in this residual fraction indicates minimum values of ~3% of the bulk sediment (Fig. 37), which as described above is the lowest resolution these calculations can provide. Therefore, we attribute the difference between the 3% noise concentration and the total residual as the result of dispersed ash (Fig. 37). As discussed for Site 999, this calculation still yields a maximum estimate for the amount of dispersed ash in a given sample, because of the potential inclusion of oxide and biogenic silica

Table 9. Major element chemistry of bulk sediment, Site 1000.

Core, section, interval (cm)	Depth (mbsf)	Ca (ppm)	Fe (ppm)	Mn (ppm)	P (ppm)	Ti (ppm)
165-1000A-						
1H-1, 145–150	1.45	351210	12184	1527	358	1047
3H-3, 145–150	16.99	382137	7133	472	310	526
6H-3, 145–150	45.75	382812	5767	294	333	556
9H-3, 145–150	74.25	386518	3975	187	246	381
12H-3, 145–150	102.75	390143	3702	203	369	370
15H-3, 145–150	131.25	381558	4963	250	328	430
18H-3, 145–150	159.75	372014	5788	290	396	529
21H-3, 145–150	188.25	362076	8254	336	419	795
24H-3, 145–150	216.75	369963	9530	272	354	680
27H-3, 145–150	245.25	380803	4522	327	383	443
30H-3, 145–150	273.75	361775	7922	285	355	732
33H-3, 145–150	302.25	375965	5523	183	278	453
36X-3, 145–150	326.95	378154	5449	231	277	432
39X-3, 145–150	355.75	371780	8544	385	281	683
42X-3, 145–150	384.55	349699	13663	237	375	1284
45X-3, 145–150	413.45	339349	12046	154	332	1158
48X-3, 145–150	442.35	356114	9139	276	279	672
51X-3, 145–150	471.15	366485	7534	113	291	723
54X-3, 145–150	500.05	357564	8885	110	329	943
165-1000B-						
4R-3, 145–150	517.65	349324	9599	156	224	975
7R-3, 145–150	546.35	367395	6576	265	303	624
11R-3, 145–150	584.85	351840	6910	207	286	786
14R-4, 88–90	614.13	349473	4365	84	252	581
17R-4, 98–100	643.03	384806	4303	229	232	350
18R-4, 98–100	653.28	376759	4647	256	227	433
21R-4, 100–102	682.10	341686	4850	81	316	668
22R-4, 98–100	691.68	356187	6854	85	308	999

Notes: Data overspecified for calculation purposes. This entire table also appears on CD-ROM (back pocket).

components in the noncarbonate, nonterrigenous fraction. However, because these other phases are present in only minimal concentrations (see "Lithostratigraphy" section, this chapter), assigning the balance entirely to ash is most likely quantitatively accurate.

Results of these calculations indicate that the dispersed ash component accounts for <5% of the bulk sediment for the upper 150 mbsf, and increases to ~5% of the bulk sediment from 150 to 350 mbsf (Fig. 37). This increase through the 150–350 mbsf interval closely follows an increase in the discrete ash layers, as quantified by the total thickness of discrete ash (Fig. 37; see "Lithostratigraphy" section, this chapter). From 350 to 430 mbsf, the dispersed ash component increases to ~10% of the bulk sediment, before again decreasing to a relative minimum value of 5% at ~470 mbsf.

This relatively short episode of dispersed ash is not paralleled by an increase in the discrete ash layers, which are absent through this interval (Fig. 37). This depth interval corresponds with lithologic Subunit IC, which is distinguished from the neighboring units on the basis of a higher clay content (see "Lithostratigraphy" section, this chapter) and the upper portions that include the carbonate minimum. Our calculations indicate that this clay is composed of both terrigenous material and altered ash. As at previous sites, although much of the dispersed ash component undoubtedly has been altered to clay (analogous to the alteration of discrete ash layers; see "Igneous Petrology and Volcanology" section, this chapter), the nature of our calculation of dispersed ash still accounts for this altered material because alteration of dispersed ash will not affect the overall elemental abundances within the bulk. At this preliminary point of interpretation, we cannot discern whether the lack of correspondence between the discrete ash layers and dispersed ash through this short interval is a result of bioturbation that has destroyed discrete layering or some other process (such as the redeposition of older ash deposits eroded from land). It is clear, however, that the clay material that defines lithologic Subunit IC reflects an increase in both altered ash and terrigenous material. Throughout the rest of the entire stratigraphic section, the patterns of dispersed ash and the discrete ash closely follow each other (Fig. 37).

Below 450 mbsf, the amount of dispersed ash increases to 15%–20% of the bulk sediment. Although this value is high in the absolute sense, it is consistent with the observations at previous sites, which also had very high concentrations of dispersed ash. Deepest in the section, the dispersed ash component shows an essentially monotonic increase, with one notable exception for a short interval at 650 mbsf. Higher resolution post-cruise research will further address this question.

The distributions of the terrigenous and dispersed ash components can be presented as the integrated cumulative percentage of each component (Fig. 38). This shows the continually summed fraction of the total sediment pile that is composed of each of these two components. The value plotted at the surface is the total percentage of the entire sediment column composed of terrigenous material (10%) and dispersed ash (7%). These values are lower than those observed at Sites 998 and 999 because at Site 1000 we did not recover the deeper portions of the sequence that are most concentrated in ash (either dispersed ash or discrete layers). Moving from the bottom of the section upward indicates that, although there are no intervals where either component greatly increases, the amount of terrigenous material is continually increasing upsection, whereas the concentration of dispersed ash does not increase significantly above 350 mbsf. Although these calculations are affected by both compositional dilution and arithmetic closure, it is clear that the terrigenous and ash components are behaving independently, as at the previous Leg 165 sites.

Calculating the accumulation rates of the terrigenous component and the dispersed ash components (see "Sedimentation and Mass Accumulation Rates" section, this chapter) allows more direct quantification of the ash flux to the seafloor, because the accumulation rate is unaffected by compositional dilution of the terrigenous material by the carbonate and ash (and vice versa). Even though the concentration of the terrigenous component is increasing upsection, as described above, the accumulation of terrigenous matter has waned since the middle Miocene (i.e., above 400 mbsf; Fig. 39). We cannot determine at this point whether this waning in terrigenous flux reflects a source change or a depositional environmental change.

The accumulation of the dispersed ash component (Fig. 39) delineates the same general pattern of ash deposition as does the concentration of the dispersed ash (Fig. 37). Most interestingly, comparing the pattern and absolute magnitude of the dispersed ash accumulation at Site 1000 to that at Site 999 (Fig. 39) indicates that the two sites record the same broad general pattern of low dispersed ash accumulation in the upper reaches of the sections with higher values lower in the sections. Within the tolerances of the different age models, the short-lived increase in accumulation from 11 to 13 Ma at each site is clearly defined and appears contemporaneous (Fig. 39). In contrast to the patterns of discrete ash layer accumulation at the two sites, which show greater accumulation of discrete ash at Site 999 (see "Igneous Petrology and Volcanology" section, this chapter), the dispersed ash at Site 1000 accumulated at essentially the same rate as it did at Site 999 (Fig. 39). Note that the two sharp maxima at 17 and 19 Ma are defined by very few data points and may not be representative. Regardless, the accumulation of dispersed ash at Site 1000 is on the same scale as the accumulation of dispersed ash at Site 999, unlike the patterns of discrete ash layers.

Definitive resolution of the dichotomy between observing a contrast in discrete layer frequency at Sites 999 and 1000, which simultaneously document similar patterns of dispersed ash accumulation, will potentially be achieved during post-cruise studies. One explanation is that there is greater atmospheric filtering of the discrete layers at Site 1000. Because only relatively large ash events are recorded by the discrete layers at either site, and because Site 1000 is farther from the Central American sources, the discrete layers at Site 1000 may be slightly less abundant for paleogeographic reasons (see "Igneous Petrology and Volcanology" section, this chapter). Another potential explanation involves the relative intensity of bioturbation at the two sites: if Site 1000 has a greater degree of bioturbation throughout several key stratigraphic horizons, then the smaller accumulation rate of discrete layers at Site 1000 than at Site 999 may record their greater

Table 10. Trace element chemistry of bulk sediment, Site 1000.

Core, section, interval (cm)	Depth (mbsf)	Nb (ppm)	Zr (ppm)	Y (ppm)	Sr (ppm)	Rb (ppm)	Zn (ppm)	Cu (ppm)	Ni (ppm)	Cr (ppm)	V (ppm)	Ba (ppm)
165-1000A-												
1H-1, 145–150	1.45	1.1	47	7	1705	12	39	28	29	14	30	160
3H-3, 145–150	16.99	<0.5	53	3	2737	5	26	24	19	9	16	197
6H-3, 145–150	45.75	<0.5	52	3	2630	7	28	24	15	8	18	164
9H-3, 145–150	74.25	<0.5	53	3	2697	4	23	22	16	7	11	160
12H-3, 145–150	102.75	<0.5	48	3	2602	5	20	23	10	5	14	143
15H-3, 145–150	131.25	0.6	32	4	1619	7	21	22	13	8	15	214
18H-3, 145–150	159.75	<0.5	28	3	1439	10	23	21	14	9	18	244
21H-3, 145–150	188.25	<0.5	33	3	1526	13	31	26	19	13	22	240
24H-3, 145–150	216.75	<0.5	38	4	1731	11	39	27	23	12	20	258
27H-3, 145–150	245.25	<0.5	33	3	1802	8	25	23	14	7	14	193
30H-3, 145–150	273.75	0.6	37	5	1557	13	37	26	22	13	20	357
33H-3, 145–150	302.25	<0.5	30	3	1622	8	27	23	20	8	17	328
36X-3, 145–150	326.95	<0.5	31	3	1683	9	24	22	18	9	16	311
39X-3, 145–150	355.75	<0.5	45	5	1951	12	29	24	23	14	25	298
42X-3, 145–150	384.55	0.8	59	8	1970	18	48	31	29	17	31	543
45X-3, 145–150	413.45	1.1	67	7	2250	19	56	30	27	20	34	311
48X-3, 145–150	442.35	0.8	38	4	1681	10	37	22	18	10	18	294
51X-3, 145–150	471.15	<0.5	51	4	2403	11	45	26	24	14	23	351
54X-3, 145–150	500.05	<0.5	46	6	1742	18	54	26	24	17	25	563
165-1000B-												
4R-3, 145–150	517.65	1.2	45	6	1519	16	49	28	25	15	27	270
7R-3, 145–150	546.35	<0.5	34	3	1512	10	31	23	15	8	17	602
11R-3, 145–150	584.85	0.7	48	10	1476	17	57	23	15	8	19	522
14R-4, 88–90	614.13	<0.5	39	5	1397	13	27	24	22	9	20	632
17R-4, 98–100	643.03	<0.5	25	3	1468	6	26	19	11	4	6	357
18R-4, 98–100	653.28	<0.5	29	2	1444	7	26	19	7	5	7	521
21R-4, 100–102	682.10	<0.5	41	11	1510	11	41	28	16	12	19	622
22R-4, 98–100	691.68	0.7	52	11	1700	18	46	26	22	14	27	628

Notes: Data overspecified for calculation purposes. This entire table also appears on CD-ROM (back pocket).

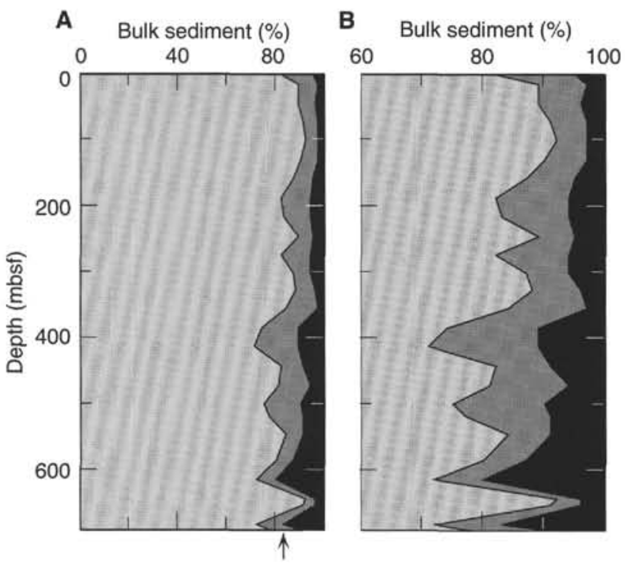

Figure 36. **A.** Depth profiles of the carbonate concentrations (light gray), terrigenous matter (dark gray), and "residual" component (black), in units of weight percent of the bulk sediment. **B.** Expanded x-axis, to highlight small-scale changes downhole.

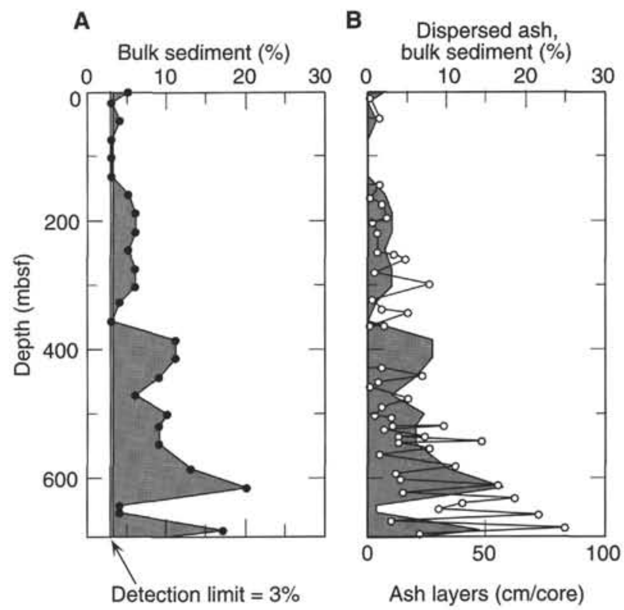

Figure 37. **A.** Depth profile of the "residual" component (solid circles; shaded above the 3% detection limit). The difference between the residual component and the detection limit of 3% is assigned to the dispersed ash component (shaded area). **B.** Depth profile of the dispersed ash component (shaded area) and the thickness of discrete ash layers (open circles).

destruction. Such bioturbation would not affect the amount of the dispersed component.

IGNEOUS PETROLOGY AND VOLCANOLOGY

Volcanic Ash Layers

The 695.9 m sedimentary succession cored at Site 1000 contains 161 megascopic volcanic ash layers. They total 826 cm in thickness and therefore represent over 1% of the sediment. Their mean thickness is 5.1 cm, but individual layers range up to 53 cm. The distribution of volcanic ash layers at Site 1000 is given in Appendix tables on CD-ROM (back pocket, this volume). Layers show variable degrees of bioturbation, with the upper part generally mixed extensively with the overlying sediment, and centimeter-sized burrows penetrating deep into some layers (Fig. 9). The highest frequency of layers per core is 13, and they constitute up to 83 cm of aggregate thickness in a single core (Core 165-1000B-21R). The accumulation rate of ash layers per million years at Site 1000 shows a marked decrease after

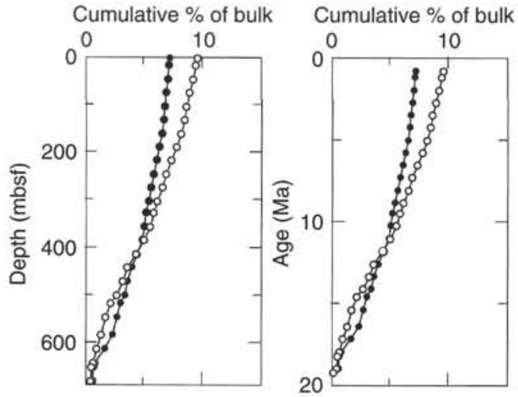

Figure 38. Cumulative percentages of terrigenous matter (open circles) and dispersed ash (solid circles) vs. depth and age. The cumulative percentage is calculated from the bottom upward; thus, values at zero depth (and zero age) represent the total percentage of the respective components at Site 1000.

the overall peak in the lower Miocene (Fig. 40). The age distribution of ash fallout at this site corresponds very closely to the timing of the Miocene episode of explosive volcanism that was observed at Site 999 on the Kogi Rise some 450 km to the south. At Site 1000, the drilling was terminated at the ~20 Ma level, near the peak of ash fallout. At 19 Ma the ash accumulation rate is 225 cm/m.y., only somewhat lower than observed at Site 999 (275 cm/m.y.). Overall, the pattern of ash accumulation at the two sites is very similar throughout the Neogene, but it is clear that Site 1000 has received less ash accumulation, either because of the greater distance from the source, or because of its position with respect to the direction of the main fallout axis from this episode. Also shown in Figure 40 is the ash layer accumulation rate at Site 998 on the Cayman Rise, 500 km to the northwest. Ash fallout during the Miocene episode generally is lower at this site, with the exception of a local peak caused by the occurrence of a single 96-cm ash layer. Thus, the pattern of fallout at these three sites supports a main ash fallout axis of the Miocene volcanic episode near the Kogi Rise or perhaps in the region between the Kogi Rise and the location of Site 1000. This is fully consistent with west-to-east atmospheric dispersal from the major volcanic centers that were active in the Miocene on the Chortis Block in Central America (Reynolds, 1980).

The volcanic ash layers are generally highly altered throughout the sediments cored at Site 1000, and the degree of alteration appears more extensive than at other sites drilled on Leg 165. Unaltered glass shards are principally colorless, platy or bubble-wall types, whereas ash layers with blocky shards are rare. The glass shards are often completely replaced by brown smectite, or they are cloudy and faintly birefringent because of the incipient replacement and crystallization of secondary minerals in the glass. Primary igneous phenocrysts are generally unaltered, however, and they include plagioclase, biotite, and more rarely hornblende, opaque minerals, and quartz. Phenocrysts are generally in the 100-µm range, but some layers contain plagioclase crystals up to 500 µm in diameter. Pyrite is an important secondary mineral in many of the layers, and its abundance has colored many layers dark gray or nearly black. The upper part of ash layers is typically bioturbated, and some thinner layers are nearly obliterated due to the extensive bioturbation characteristic of these relatively organic-rich sediments.

An unusual feature of this site is the occurrence of three exceptionally thick layers (31, 41, and 53 cm). They are either relatively massive or normally graded beds, which appear to represent single eruptions. Some of these layers show "dish" structures and other internal structures suggestive of fluid escape during compaction of the sediment. There is no evidence to indicate that they are over-thickened because of redeposition of the ash; most likely they indicate explosive eruptions of exceptional volume.

The solid-phase geochemistry of the Leg 165 sediments has quantified a dispersed ash component that is significantly larger than the mass of coexisting ash layers. As observed at other sites during Leg 165, dispersed ash is transported in large quantities to the Caribbean basin, either through tephra fallout or by fluvial transport processes. Thus, any estimates of total volcanic ash deposition must take into account this additional ash component.

Geochemistry

The chemical composition of seven representative and relatively unaltered volcanic ash layers recovered at Site 1000 was determined by XRF methods aboard ship. Table 11 gives the major element composition of the ashes, and the trace element concentration is given in Table 12. They range in age from 6 to 18 Ma and thus represent the Miocene episode. Although they are all silicic, these volcanic ash layers span a relatively compositional range from dacite to rhyolite. Overall, their major and trace element composition is closely comparable to Miocene tephra recovered at Sites 998 and 999.

PHYSICAL PROPERTIES

The physical properties program at Site 1000 included multisensor track (MST) and thermal conductivity measurements of whole-round cores, and *P*-wave velocity, electrical resistivity, vane shear strength, and index properties measurements of split cores. Methods for these measurements are described in the "Physical Properties" section of the "Explanatory Notes" chapter (this volume).

Although the high recovery at Site 1000 allowed us to obtain a complete suite of physical properties data, the high recovery rate forced us to adopt a lower resolution sampling program than at Sites 998 and 999. MST *P*-wave velocity, magnetic susceptibility, and GRAPE data were recorded at 1-cm intervals for Cores 165-1000A-1H to 2H (down to a depth of about 12.8 mbsf). In all other cores, measurements were made at 5-cm intervals. MST *P*-wave velocity data were not recorded in the part of Hole 1000A cored with the XCB and the part of Hole 1000B cored with the RCB (deeper than 312.9 mbsf). MST natural gamma-ray measurements were made at 10-cm intervals for Cores 165-1000A-1H to 3H to a depth of about 22.3 mbsf, and at 20-cm intervals below this depth. Thermal conductivity was measured 30 cm from the top of Sections 1, 3, and 5 of each core in Hole 1000A to a depth at which induration prevented insertion of the needles (around 304 mbsf). We measured velocity, shear strength, and resistivity on all split cores (165-1000A-1H to 3H) to a depth of 22.3 mbsf; after that, measurements were taken only on Sections 1, 3, and 5 of all split cores. One measurement per section of electrical resistivity and vane shear strength was taken in Hole 1000A to a depth at which induration prevented insertion of the needles for electrical resistivity (around 326 mbsf) and the vane for shear strength (around 89 mbsf). Samples for index properties were taken at a sampling interval of one per section in Cores 165-1000A-1H through 39X (360.9 mbsf); below this depth, samples were not taken in the seventh section of Cores 165-1000A-40X to 165-1000B-22R. If possible, measurements and samples were taken 30 cm from the top of each section.

Multisensor Track

Data from the MST measurements are presented in Figure 41 and Tables 13 through 16. The magnetic susceptibility (Fig. 41) shows a very low background signal compared with results obtained at Sites 998 and 999; the base level is about 10×10^{-6} cgs units from the seafloor to a depth of about 18 mbsf. The susceptibility rapidly drops to

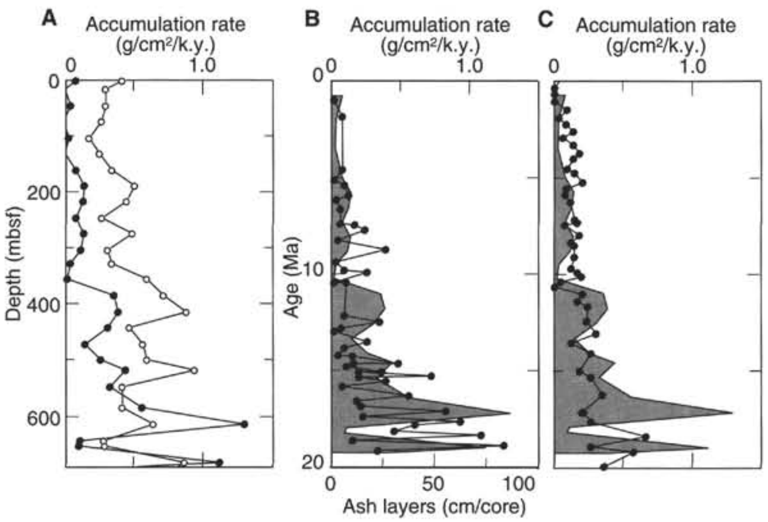

Figure 39. **A.** Accumulation rate of the terrigenous (open circles) and dispersed ash (solid circles) components at Site 1000. **B.** Accumulation rate of dispersed ash (shaded area) vs. total thickness of ash layers per core (solid circles). **C.** Accumulation rates of dispersed ash at Sites 999 (solid circles) and 1000 (shaded area).

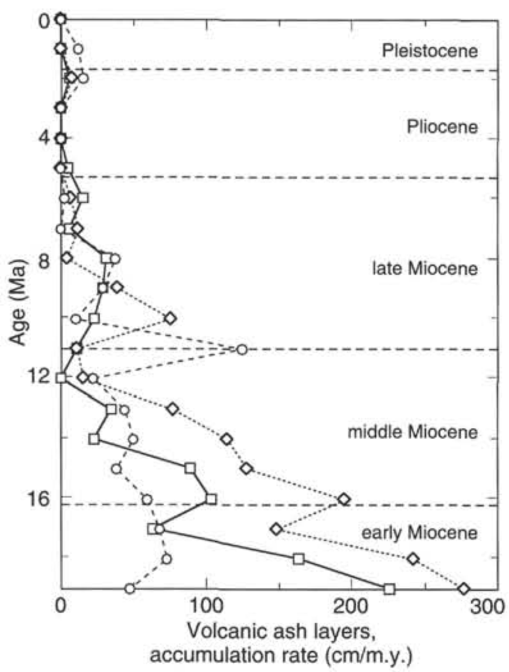

Figure 40. Volcanic ash layer accumulation rate (cm/m.y.) at Site 1000 (open squares). Also shown are the ash layer accumulation rates for Sites 998 (open circles) and 999 (open diamonds). The ash layer distribution of Site 1000 for the Miocene episode is remarkably similar to that at Site 999, although systematically shifted to lower values. These results indicate that the principal fallout axis of the Miocene explosive volcanic episode lies south of Site 1000, possibly between this site and Site 999, or across the latitude of the latter site. This constrains the latitude of the central source region to about 13°–14°N, which coincides with the central part of the Chortis Block in the Central American volcanic arc.

~0 cgs units by ~30 mbsf and maintains this low profile for most of the record. The low susceptibility values may be a result of reduction diagenesis (see "Paleomagnetism" section, this chapter). Two zones of slightly elevated susceptibility are evident in the section. The first zone, from 180 to 230 mbsf, has a high of about 3×10^{-6} cgs units and appears to correlate with a zone of lower carbonate content (see "Lithostratigraphy" section, this chapter). The second, from 370 to 430 mbsf, has a high of about 4×10^{-6} cgs units and appears to correlate with the carbonate crash (see "Lithostratigraphy" section, this chapter). Narrow peaks in the susceptibility profile ($5–15 \times 10^{-6}$ cgs units) generally correlate with distinct ash layers.

The GRAPE densities are close to those determined from index properties (Fig. 41) in the interval of Hole 1000A cored with the APC (to a depth of 312.9 mbsf). GRAPE densities are shifted to lower values relative to index properties data for the portion of Hole 1000A cored with the XCB and for all of Hole 1000B. This is to be expected because the XCB cores from Hole 1000A and the RCB cores of Hole 1000B do not fill the liner, and the GRAPE processing assumes a core diameter corresponding to a filled liner. The Boyce correction is included in the processing of all GRAPE data at Site 1000. Density variations at Site 1000 are described in the "Index Properties" section (this chapter).

Although high variability is present in the measured values, MST *P*-wave logger (PWL) velocity data generally agree with the data collected on the split cores (see below). The high variability possibly is caused by poor contact between the PWL transducers and the core liner, and the high-velocity spikes should not be interpreted as true velocities without extreme caution. MST *P*-wave measurements were not collected for the XCB-cored portion of Hole 1000A or the RCB-cored Hole 1000B because valid *P*-wave measurements require that the core liner be filled.

The natural gamma radiation is generally low and shows no strong correlation with any of the other physical properties measurements. It does, however, show a slightly elevated interval from about 370 to about 540 mbsf, which appears to coincide with a zone of minor hydrocarbon shows (see "Organic Geochemistry" section, this chapter).

Thermal Conductivity

Thermal conductivity (Table 17; Fig. 42) increases from around 1.1 W/(m·K) near the seafloor, where porosities are about 70%, to around 1.3 W/(m·K) at 300 mbsf, where porosities have fallen to about 60%.

P-wave Velocity

P-wave velocity measurements from split cores were made along the axis of the core (DSV1) as well as perpendicular to the axis (DSV2) by the Digital Sonic Velocimeter (Table 18; Fig. 43) down to a depth of around 65 mbsf. Examination of the DSV1 velocities (perpendicular to bedding) vs. DSV2 velocities (parallel to bedding) shows no anisotropy data for the uppermost 65 m of Hole 1000A. The

Table 11. Major oxide composition of volcanic ash layers.

Core, section, interval (cm)	Depth (mbsf)	SiO_2	TiO_2	Al_2O_3	Fe_2O_3	MnO	MgO	CaO	Na_2O	K_2O	P_2O_5	Total	LOI
165-1000A-													
22H-2, 57–60	195	70.7	0.33	16.0	3.50	0.06	1.94	0.95	3.33	3.79	0.04	100.6	6.85
56X-CC, 18–21	523	73.2	0.20	14.4	2.51	0.04	1.05	1.26	3.11	4.36	0.03	100.2	6.14
58X-2, 47–50	536	62.6	0.44	19.7	6.13	0.01	3.77	3.21	2.83	1.10	0.05	99.8	6.62
165-1000B-													
6R-4, 143–145	537	65.8	0.56	17.9	4.40	0.04	3.27	2.72	3.17	1.60	0.06	99.5	7.26
11R-1, 142–145	582	66.2	0.36	18.0	4.43	0.02	3.80	1.50	3.06	1.95	0.05	99.4	7.06
19R-2, 88–91	660	66.3	0.20	17.9	4.39	0.02	4.96	0.94	3.25	2.12	0.04	100.1	7.02
21R-4, 43–46	681												9.36

Notes: Shipboard XRF data in weight percent. Total iron reported as Fe_2O_3. LOI = loss on ignition. This entire table also appears on CD-ROM (back pocket).

Table 12. Trace element composition of volcanic ash layers.

Core, section, interval (cm)	Nb	Zr	Y	Sr	Rb	Zn	Cu	Ni	Cr	V	Ba
165-1000A-											
22H-2, 57–60	7.9	236	17	497	80	50	4	14	<3	12	657
56X-CC, 18–21	8.8	176	21	322	123	45	4	7	<3	7	729
58X-2, 47–50	2.5	256	<1	1074	27	26	25	45	<3	27	250
165-1000B-											
6R-4, 143–144	5.4	142	11	793	22	49	20	153	<3	39	496
11R-1, 142–145	8.4	245	7	896	61	26	7	6	<3	19	215
19R-2, 88–91	14.5	277	7	1667	43	46	5	6	<3	14	251
21R-4, 43–46	18.0	204	17	1988	48	44	5	3	<3	10	287

Notes: Shipboard XRF data in parts per million (ppm). This entire table also appears on CD-ROM (back pocket).

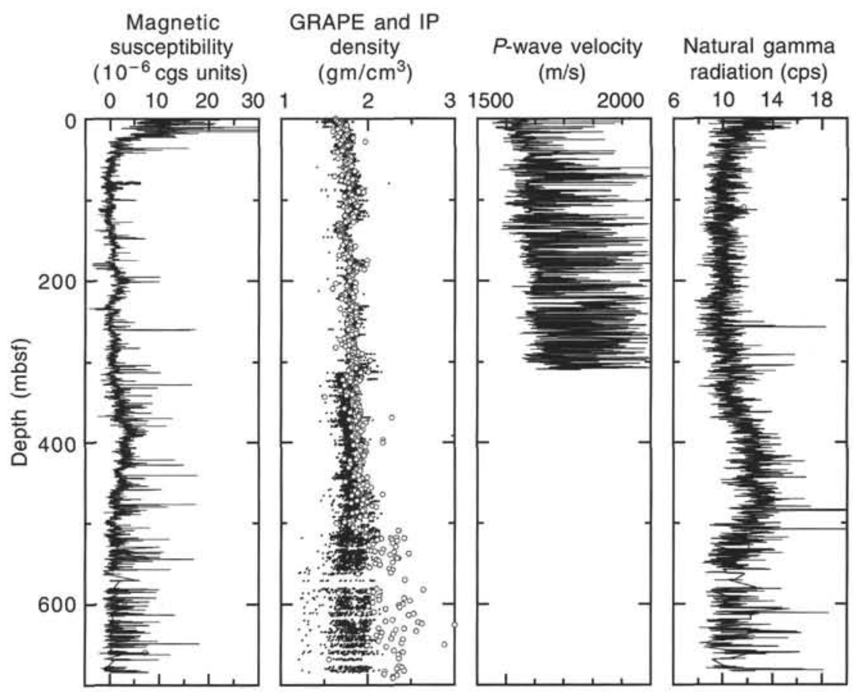

Figure 41. Multisensor track data showing magnetic susceptibility, GRAPE (with index properties density for comparison, open circles), *P*-wave velocity, and natural gamma radiation vs. depth.

isotropic nature for this interval may be due to a relatively low clay content. Below 65 mbsf, the sediments exhibited varying degrees of induration, which forced us to measure *P*-wave velocities on half cores parallel to bedding using the Hamilton Frame. This change of measuring device seems to have had no affect on the continuity of the data.

The laboratory data were corrected to in situ stress (Table 18; Fig. 43) using the empirical relation derived by Urmos et al. (1993; see "Physical Properties" section, "Site 998" chapter, this volume). The use of this correction, being derived for a pure carbonate lithology, appears to be valid for the dominantly pelagic carbonate sediments of Site 1000, as the Urmos depth-corrected velocities are in close agreement with the results from the sonic log (see "Downhole Measurements" section, this chapter).

A gradual increase in velocity with depth is evident from about 1.55 km/s at the seafloor to about 2.3 km/s at about 510 mbsf. Within this upper 510 m, there appear to be three intervals with different rates of increase in velocity with depth. The intervals from 0 to 120 mbsf and from 280 to 510 mbsf show slightly higher rates of velocity increase with depth than the interval from 120 to 280 mbsf. There are no visible shifts in velocities at the boundaries between these intervals.

Table 13. Magnetic susceptibility data for Site 1000.

Core, section, interval (cm)	Depth (mbsf)	Raw mean susc. (cgs)	SD susc.	Drift corr.	DAQ period (s)	Bkgd. corr.
165-1000A-						
1H-1, 3	0.03	6.2	2.121974	0	5	0.006
1H-1, 4	0.04	10	0	0	5	0.009
1H-1, 5	0.05	9.8	0.235775	0	5	0.012
1H-1, 6	0.06	10	0	0	5	0.015
1H-1, 7	0.07	9.6	0.326787	0	5	0.018
1H-1, 8	0.08	10.8	0.273924	0	5	0.021
1H-1, 9	0.09	11.4	0.326787	0	5	0.024
1H-1, 10	0.1	11.4	0.355295	0	5	0.026
1H-1, 11	0.11	11.4	0.349799	0	5	0.029
1H-1, 12	0.12	14	0	0	5	0.032

Notes: SD = standard deviation, DAQ = data acquisition. The data in this table differ from the raw data in that (1) all columns do not appear, (2) depths have been added, (3) columns have been labeled, (4) unsuccessful measurements have been deleted, and (5) magnetic susceptibility has been averaged.

Only part of this table is produced here. The entire table appears on CD-ROM (back pocket).

Table 14. Gamma-ray attenuation porosity evaluator (GRAPE) data for Site 1000.

Core, section, interval (cm)	Depth (mbsf)	Raw counts	DAQ period (s)	Density (g/cm^3)	Boyce corr. density (g/cm^3)
165-1000A-					
1H-1, 3	0.03	20,690	5	1.719	1.64933
1H-1, 3	0.03	20,690	5	1.719	1.64933
1H-1, 4	0.04	20,603	5	1.727	1.65789
1H-1, 5	0.05	20,600	5	1.728	1.65896
1H-1, 6	0.06	20,584	5	1.729	1.66003
1H-1, 7	0.07	20,283	5	1.757	1.68999
1H-1, 8	0.08	20,265	5	1.759	1.69213
1H-1, 9	0.09	20,230	5	1.762	1.69534
1H-1, 10	0.1	20,205	5	1.764	1.69748
1H-1, 11	0.11	20,342	5	1.752	1.68464

Notes: DAQ = data acquisition. Density = bulk density. Corr. = correction. The data in this table differ from the raw data in that (1) all columns do not appear, (2) depths have been added, (3) columns have been labeled, and (4) unsuccessful measurements have been deleted.

Only part of this table is produced here. The entire table appears on CD-ROM (back pocket).

Table 15. Multisensor track *P*-wave data for Site 1000.

Core, section, interval (cm)	Depth (mbsf)	*P*-wave velocity (m/s)	Raw mean time	Raw SD time	Raw mean displ.	Raw SD displ.	Mean signal level	DAQ period (s)
165-1000A-								
1H-1, 10	0.1	1557.3	50	0.0245	54	0	1385	
1H-1, 11	0.11	1555.2	50.1	0.02	54	0	163	5
1H-1, 12	0.12	1553.4	50.1	0.02	54	0	172	5
1H-1, 13	0.13	1554.1	50.1	0.0245	54	0	1735	
1H-1, 14	0.14	1553.7	50.1	0.0245	54	0	1435	
1H-1, 15	0.15	1550	50.1	0.02	52	0	173	5
1H-1, 16	0.16	1538.6	50.1	0.0245	47	0	1795	
1H-1, 17	0.17	1538.9	50.1	0.02	47	0	177	5
1H-1, 18	0.18	1538.2	50.1	0.0245	47	0	1755	
1H-1, 19	0.19	1541	50	0	47	0	180	5

Notes: SD = standard deviation, displ. = displacement, DAQ = data acquisition. The data in this table differ from the raw data in that (1) all columns do not appear, (2) depths have been added, (3) columns have been labeled, and (4) unsuccessful measurements have been deleted.

Only part of this table is produced here. The entire table appears on CD-ROM (back pocket).

Below these intervals, the velocity data show a dramatic increase in velocity from 2.3 km/s above 510 mbsf to 2.8 km/s below 510 mbsf. There is also a greater variability in velocity measurements below 510 mbsf, with values ranging from about 2.7 to 4.1 km/s. The change at 510 mbsf correlates with the boundary of lithologic Units I and II (see "Lithostratigraphy" section, this chapter), seismic stratigraphic Units A and B (see "Seismic Stratigraphy" section, this chapter), logging Units B and C (see "Downhole Measurements" section, this chapter), and major changes in index properties (see below).

Index Properties

Index properties data were determined from wet and dry weights and wet and dry volumes, and used to calculate wet-bulk density, grain density, water content, porosity, and dry-bulk density (Table 19; Fig. 44; see "Explanatory Notes" chapter, this volume). Because of the high rate of recovery at Site 1000, we were forced to measure dry volumes on only Sections 1 and 4 of all cores after Core 8H (below a depth of 69.9 mbsf). Thus, calculations of grain density are limited to Sections 1 and 4 for Cores 9H to 59X for Hole 1000A, and all of Hole 1000B.

Bulk densities increase from about 1.6 g/cm^3 at the seafloor to about 2.3 g/cm^3 at around 700 mbsf, water content decreases from about 48% at the seafloor to around 14% at about 700 mbsf, and porosity decreases from about 70% near the seafloor to around 30% at a depth of 700 mbsf (Fig. 44).

The major feature evident in Figure 44 is a significant shift in all index properties at about 510 mbsf. Bulk densities increase from about 1.9 g/cm^3 above to around 2.2 g/cm^3 below 510 mbsf; water content decreases from about 30% above to around 20% below 510 mbsf; and porosity decreases from about 55% above to around 40% below 510 mbsf. There is also a higher variability in measured values below 510 mbsf compared with the shallower part of the hole. This shift correlates with the boundary between lithologic Units I and II (see "Lithostratigraphy" section, this chapter) and seismic stratigraphic Units A and B (see "Seismic Stratigraphy" section, this chapter), and an increase in DSV velocity measurements (see above).

A small interval characterized by higher porosity, higher water content, and lower density is evident between 120 and 160 mbsf; it appears to correlate with a zone of slightly lower carbonate content (see "Lithostratigraphy" section, this chapter). The zone of enriched hydrocarbons (see "Organic Geochemistry" section, this chapter) between 380 and 535 mbsf suggests that this interval may be a migration pathway; however, porosity values are no higher than in the adjacent lithologies.

Electrical Resistivity

Electrical resistivity data (Table 20; Fig. 45) were collected at the same locations where the velocity measurements were made. The electrical resistivity increases from around 0.5 Ωm near the seafloor to around 1.1 Ωm at 310 mbsf. The formation factor, *F*, was calculated from $F = R_o/R_w$, where R_o is the resistivity of the sediment and R_w is the resistivity of the pore water. The pore-water resistivity was assumed to be that of seawater at 20°C (0.206 Ωm). The porosity, Ø, was calculated from the formation factor by Archie's equation

$$Ø = (a/F)^{1/m},$$

where *F* = formation factor, and *a* and *m* are lithology-dependent constants. The relationship of porosity to formation factor results in Archie coefficients of 1.2 and 2.33 for *a* and *m*, respectively. The resulting porosity data, when compared with index properties–derived porosities, indicate minor differences in the upper 100 m of Hole 1000A, whereas with resistivity-derived porosities, the porosity data is about 10% lower than index properties–derived porosities. Below 100 mbsf, there is excellent agreement between the two data sets (Fig. 45).

Vane Shear Strength

The ODP motorized minivane was used to measure undrained shear strength in split-core sections (Table 21; Fig. 46). The measurements were made at the same depths used for *P*-wave velocity deter-

Table 16. Natural gamma-ray (NGR) data for Site 1000.

Core, section, interval (cm)	Depth (mbsf)	GR (cps)	Win 1	Win 2	Win 3	Win 4	Win 5	DAQ period (s)
165-1000A-								
1H-1, 16	0.16	12.04	6.17	3.83	1.27	0.3	0.47	30
1H-1, 26	0.26	10.8	5.33	3.47	1.4	0.27	0.33	30
1H-1, 36	0.36	10.71	5.13	3.57	1.27	0.27	0.47	30
1H-1, 46	0.46	10.84	5.47	3.4	1.27	0.43	0.27	30
1H-1, 56	0.56	10.44	5.5	2.6	1.47	0.47	0.4	30
1H-1, 66	0.66	10.84	5.87	3.13	1.1	0.37	0.37	30
1H-1, 76	0.76	10.96	5.77	3.23	1.23	0.33	0.4	30
1H-1, 86	0.86	11.94	5.97	3.97	1.23	0.47	0.3	30
1H-1, 96	0.96	11.02	5.8	3.13	1.43	0.13	0.53	30
1H-1, 106	1.06	12.27	6.03	4	1.47	0.3	0.47	30

Notes: Win 1 through Win 5 = counts per second in each of five energy windows, corresponding to Schlumberger practice for spectral natural gamma-ray logs. DAQ = data acquisition. The data in the table differ from the raw data in that (1) all columns do not appear, (2) depths have been added, (3) columns have been labeled, and (4) unsuccessful measurements have been deleted.

Only part of this table is produced here. The entire table appears on CD-ROM (back pocket).

Table 17. Thermal conductivity measured on whole-round core sections for Site 1000.

Core, section, interval (cm)	Depth (mbsf)	Thermal conductivity (W/[m·K])
165-1000A-		
1H-1, 33–33.1	0.33	1.223
1H-3, 33–33.1	2.95	1.150
2H-1, 33–33.1	3.63	1.048
2H-3, 33–33.1	6.63	1.065
2H-5, 33–33.1	9.63	1.129
3H-1, 33–33.1	13.13	1.063
3H-3, 33–33.1	15.87	1.099
3H-5, 33–33.1	18.87	1.009
4H-1, 30–30.1	22.6	1.179
4H-3, 30–30.1	25.6	1.256

Only part of this table is produced here. The entire table appears on CD-ROM (back pocket).

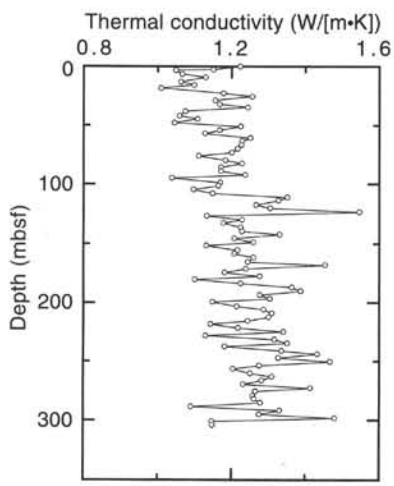

Figure 42. Thermal conductivity vs. depth measured on whole cores.

Table 18. DSV (DSV1 and DSV2) and Hamilton Frame (DSV3) velocities measured at discrete intervals for Site 1000.

Core, section, interval (cm)	Depth (mbsf)	Instrument	Velocity (km/s)	Urmos correction (km/s)	Corrected velocity (m/s)
165-1000A-					
1H-1, 33.1–33.2	0.33	DSV1	1.571	0.000	1571
1H-1, 33.0–33.1	0.33	DSV2	1.553	0.000	1553
1H-2, 33.0–33.1	1.83	DSV1	1.547	0.003	1550
1H-2, 33.1–33.2	1.83	DSV2	1.562	0.003	1565
1H-3, 33.0–33.1	2.95	DSV1	1.556	0.004	1560
1H-3, 33.0–33.1	2.95	DSV2	1.552	0.004	1556
2H-1, 33.1–33.2	3.63	DSV1	1.544	0.005	1549
2H-1, 33.0–33.1	3.63	DSV2	1.521	0.005	1526
2H-2, 33.1–33.2	5.13	DSV1	1.554	0.007	1561
2H-2, 33.1–33.2	5.13	DSV2	1.541	0.007	1548

Note: DSV = Dalhousie University/Bedford Institute of Oceanography Digital Sonic Velocimeter.

Only part of this table is produced here. The entire table appears on CD-ROM (back pocket).

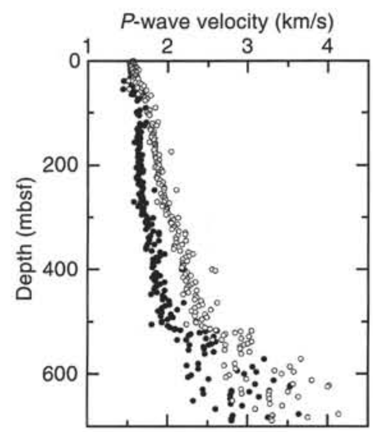

Figure 43. *P*-wave velocity vs. depth. Solid circles represent uncorrected DSV and Hamilton Frame measurements; open circles refer to Urmos depth-corrected values.

Table 19. Index properties measured at discrete intervals for Site 1000.

Core, section, interval (cm)	Depth (mbsf)	Water content (bulk wt%)	Bulk density (g/cm³)	Grain density (g/cm³)	Dry density (g/cm³)	Porosity (%)
165-1000A-						
1H-1, 32–34	0.32	43.88	1.63	2.86	0.91	69.78
1H-2, 32–34	1.82	43.49	1.63	2.77	0.92	69.00
1H-3, 32–34	2.94	44.67	1.65	2.83	0.91	71.94
2H-1, 32–34	3.62	41.15	1.69	2.79	0.99	67.80
2H-2, 32–34	5.12	42.10	1.68	2.88	0.97	68.99
2H-3, 32–34	6.62	42.53	1.67	2.77	0.96	69.46
2H-4, 32–34	8.12	39.34	1.75	2.86	1.06	67.26
2H-5, 32–34	9.62	41.37	1.69	2.83	0.99	68.17
2H-6, 32–34	11.12	40.64	1.67	2.74	0.99	66.34
2H-7, 32–34	12.62	39.38	1.73	2.83	1.05	66.61

Only part of this table is produced here. The entire table appears on CD-ROM (back pocket).

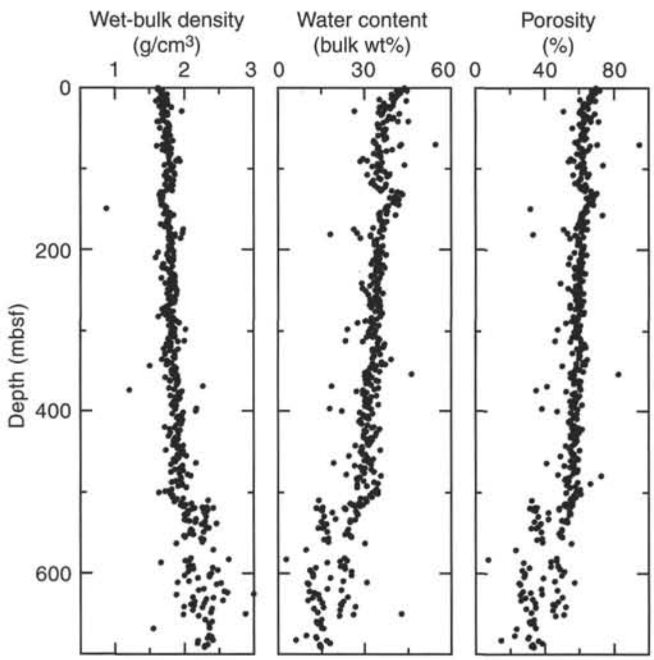

Figure 44. Index properties wet-bulk density, water content, and porosity vs. depth.

Table 20. Electrical resistivity measured at discrete intervals for Site 1000.

Core, section, interval (cm)	Depth (mbsf)	Resistivity (Ωm)
165-1000A-		
1H-1, 31–31.1	0.31	0.493
1H-2, 33–33.1	1.83	0.612
1H-3, 33–33.1	2.95	0.571
2H-1, 33–33.1	3.63	0.502
2H-2, 33–33.1	5.13	0.561
2H-3, 33–33.1	6.63	0.512
2H-4, 33–33.1	8.13	0.593
2H-5, 33–33.1	9.63	0.564
2H-6, 33–33.1	11.13	0.501
2H-7, 33–33.1	12.63	0.532

Only part of this table is produced here. The entire table appears on CD-ROM (back pocket).

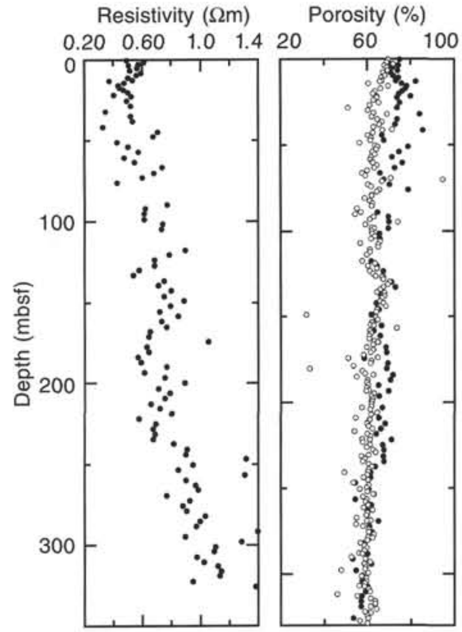

Figure 45. Plot of electrical resistivity vs. depth and a comparison of Archie porosity (open circles) and porosity from index properties (solid circles) vs. depth.

Table 21. Undrained and residual shear strength from miniature vane shear measurements for Site 1000.

Core, section, interval (cm)	Depth (mbsf)	Undrained shear strength (kPa)	Residual shear strength (kPa)
165-1000A-			
1H-1, 32–32.1	0.32	7.5	3.9
1H-2, 33–33.1	1.83	10.6	2.5
1H-3, 33–33.1	2.95	12.5	8.6
2H-1, 33–33.1	3.63	5.1	1.5
2H-2, 33–33.1	5.13	6.4	2.7
2H-3, 33–33.1	6.63	6.2	2.2
2H-4, 33–33.1	8.13	18.3	10.1
2H-5, 33–33.1	9.63	6.4	3.3
2H-6, 33–33.1	11.13	14.5	6.6
2H-7, 33–33.1	12.63	12	5.8

Only part of this table is produced here. The entire table appears on CD-ROM (back pocket).

mination. Overall, shear strength increases with depth from about 5 kPa at the seafloor to about 18 kPa at 23 mbsf, below which the shear strength varies widely between about 5 and 28 kPa.

DOWNHOLE MEASUREMENTS

Operations

After drilling to a total depth of 695.9 mbsf in Hole 1000B, the borehole and drilling equipment were prepared for wireline logging. Upon the completion of coring operations, a complete wiper trip was made to condition the borehole for logging. With the pipe set near the bottom of the hole, the bit was released and a pill of sepiolite mud was pumped down the drill pipe to sweep the hole of cuttings not removed by circulated seawater. As the drill pipe was raised to logging depth, a slug of barite mud was pumped down the drill pipe to sup-

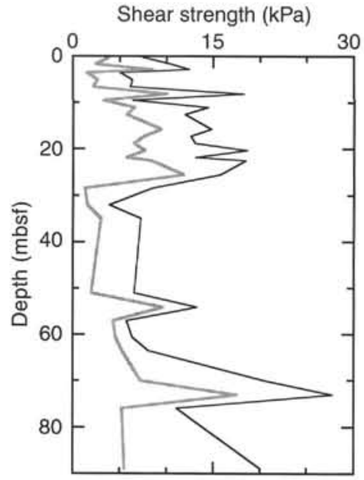

Figure 46. Undrained shear strength (solid line) and residual shear strength (shaded line) vs. depth.

press the hydraulic head of the drilling fluid and prevent seawater from flowing out of the pipe and onto the rig floor. The wireline heave compensator was malfunctioning and not available for use during logging operations at Hole 1000B. Fortunately, low heave conditions (~2.5-m swell) prevailed, and no obvious adverse affects occurred during data collection.

The first of three logging runs began in Hole 1000B at 0900 UTC on 31 January 1996. All logging operations were completed by 2230 UTC on 31 January, corresponding to a total logging time of 16.25 hr (Table 22). Each tool string was run to the bottom of the hole and then pulled at a rate of 200–600 m/hr upward to acquire high-resolution log data. During the upward logging run for each tool, the pipe was raised 27 m to a depth of 272.8 mbsf to provide more available open hole. A repeat section was also run with each tool string to provide data quality control.

The Quad combo (QC) tool string included, from top to bottom, the telemetry cartridge, natural gamma spectrometry, long-spaced sonic, compensated neutron, lithodensity, dual induction resistivity, and the Lamont temperature tools, creating a tool string 34 m long. The QC tools were run down to the bottom of the hole, to a depth of 688.8 mbsf, which was ~7 m above total drilling depth, as determined by wireline measurements. This depth discrepancy is likely to be the result of the tool string encountering debris, including the drill bit, that had filled the lower 7 m of the hole. During the first upward logging run, data were acquired at a speed of 300 m/hr from 688.8 mbsf up into pipe (at 272.8 mbsf) and concluding at 255 mbsf (Table 22). The final upward QC run was completed by acquiring data in a repeat section between 372.5 mbsf and logging through the drill pipe to 15.4 m above the seafloor.

The geological high-sensitivity magnetic tool (GHMT) string, including telemetry, natural gamma spectrometry, and GHMT sections, was the second tool string run in the hole. A total depth of 672.8 mbsf was reached, which was 23.1 m shallower than the depth drilled and 16.1 m shallower than the total depth measured by the QC. The bottom of the hole was rapidly filling with material from the upper portion of the borehole. Logging data were recorded from 672.8 to 313 mbsf as the tool string moved uphole at 600 m/hr (Table 22). A second upward run was made with the GHMT between 517.9 and 297.9 mbsf.

The Formation MicroScanner (FMS) included telemetry, natural gamma spectrometry, and FMS sections. To assist the tool in descending to total depth more quickly, downward pressure was applied to the tool by pumping seawater down the drill pipe. High-resolution data were collected with the FMS between 673.8 and 285.4 mbsf at a rate of 300 m/hr (Table 22). A repeat section from 673.8 to 271.4 mbsf was run for quality control.

Log Quality

In general, the data from all three tool strings are of high quality and do not appear to be degraded by borehole washouts. The bulk density and the PEF values are not valid above 302 mbsf, where the caliper arms were closed. It was necessary to adjust several data points where the HLDT tool had recorded erroneous density and PEF values. Only two unrealistically low sonic velocities were detected, and these were replaced with interpolated values. Additional processing of logging data, including depth shifting, was conducted on shore by the Borehole Research Group. The results are presented in Figures 47 and 48, in the compilation figures at the end of this chapter, and on CD-ROM (back pocket). Detailed information regarding shore-based log processing is given in the "Downhole Measurements" section of the "Explanatory Notes" chapter (this volume).

Logging Units

Four logging units were identified in Hole 1000B (Figs. 47, 48), based on log responses and analyses of recovered cores; these should not be confused, however, with the lithologic units defined earlier (see "Lithostratigraphy" section, this chapter). The boundaries between adjacent logging units were placed at significant inflection points resulting from simultaneous variations on several of the logs. These units display consistent log responses or distinct overall trends.

The lithologies for unrecovered intervals can be inferred from the logs based on the broad assumption that the logging tools respond to varying proportions of the primary constituents in samples actually recovered (e.g., carbonate, clay, volcanic ash, biogenic silica) and to their relative porosity.

Logging Unit 1 (277–378 mbsf)

Logging Unit 1 is characterized by higher amplitude variations in velocity, density, resistivity, and PEF relative to Unit 2. Unit 1 contains an interval between 298 and 320 mbsf in which distinct zones of alternating, relatively high-amplitude minima and maxima of sonic velocity (1.9–2.5 km/s), density (IDPH 1.7–2.0 g/cm^3), and PEF (4.5–6.0 barns/e) are observed (Fig. 47). Gamma-ray counts are relatively low throughout Unit 1, with higher amplitude minima-maxima between 298 and 320 mbsf, primarily because of increases in Th and K concentrations (Fig. 48). Several distinct Th/U peaks occur within this unit and correspond, interestingly, to intervals of higher velocity, density, resistivity, and PEF. Thorium concentrations in volcanic ash are typically high relative to U and K, and therefore increases in Th/U can be used to discriminate ash layers from nonvolcanogenic clays. Uranium, on the other hand, is more mobile than K or Th and can be concentrated in organic-rich layers. The SGR curve represents the total gamma-ray count from U, Th, and K, and the CGR curve represents gamma-ray counts for only Th and K. The difference in these two curves is a convenient way of indicating relative uranium concentrations (Fig. 48). Uranium concentrations, relative to Th and K, are generally elevated throughout the logged interval and are often two to three times the concentrations recorded at Sites 998, 999, and 1001. In Unit 1, however, the U concentrations are quite variable and low relative to logging Unit 2.

Logging Unit 1 corresponds to the base of lithologic Subunit IB (50.8–370.5 mbsf), which consists of micritic nannofossil ooze with foraminifers (see the "Lithostratigraphy" section, this chapter). The transition from ooze to micritic chalks in the lower portion of lithologic Subunit IB and variations in grain size (foraminifer sands), along with an increase in ash layers, may be responsible for larger variations in amplitude observed in the logs (e.g., two thick ash layers

Table 22. Time schedule (UTC) for logging operations at Hole 1000B, including a listing of the tools used during each logging run.

Time (UTC)	Activity
31 Jan. 1996	
Drillers' TD = 1623.07 mbrf (695.9 mbsf), WD = 927.2 mbrf	
0615	Make up cable. Quad combo assembled and prepared for logging.
0800	Run in hole with Quad combo (TLT/DIT/HLDT/CNT/SDT/NGT/TCC/LEH-Q).
0900	Begin logging first upward pass (688.8–255 mbsf). Pull pipe up 27 m to 272.8 mbsf. Log 117.9-m repeat section (372.9–255 mbsf).
1120	Quad combo pulled out of drill string.
1230	Quad combo disassembled and removed from rig floor.
0100	GHMT assembled and prepared for logging.
0115	GHMT lowered into the drill string.
0445	Touch bottom and begin first upward logging pass (672.8–313 mbsf). Pulled pipe up 27 m to 272.8 mbsf. Complete second logging run (517.9–297.9 mbsf).
1600	GHMT pulled out of drill string.
1630	GHMT disassembled and removed from rig floor.
1640	FMS assembled and prepared for logging.
1650	RIH with FMS.
1810	Touch bottom and begin logging first logging upward run (673.8–285.4 mbsf). Pull pipe up 27 m to 272.8 mbsf. Complete second logging run (673.8–271.4 mbsf).
2010	FMS pulled out of drill string.
2130	FMS disassembled and removed from rig floor.
2230	End logging operations.

at 301 and 304 mbsf; see "Igneous Petrology and Volcanology" section, this chapter). The boundary between logging Units 1 and 2 is not sharp and occurs over slightly different depths, depending on which logging data are used. For example, a minimum in gamma ray is observed at 365–370 mbsf, followed by an abrupt increase to values above 20 API, which is primarily due to an increase in uranium concentration, whereas an interval of high magnetic susceptibility occurs from 370 to 390 mbsf. The lower boundary of logging Unit 1 is also characterized by co-varying minima-maxima in velocity, density, resistivity, and PEF from 363 to 378 mbsf. The anomaly marking the lower boundary of logging Unit 1 straddles the lithologic Subunit IB/IC boundary (i.e., 370 mbsf), which is distinguished by an abrupt decrease in carbonate content as well as an absence of ash layers from 362 to 427 mbsf ("Lithostratigraphy" and "Igneous Petrology and Volcanology" sections, this chapter). The increase in gamma-ray counts at this boundary is primarily caused by an increase in potassium concentration and is consistent with a higher relative clay content within the middle/late Miocene carbonate crash. There also appear to be significant changes in physical properties of the sediment from 363 to 378 mbsf in an otherwise uniform background.

Logging Unit 2 (378–512 mbsf)

Logging Unit 2 is characterized by a variable but steadily increasing U concentration, matched by a variable but steadily decreasing K concentration, reaching maximum and minimum values, respectively, at 487 mbsf. The gamma-ray counts are elevated (>20 API) and the shape of the SGR curve is dominated by significant fluctuations in U concentration, which generally vary inversely with K. In addition, velocity increases uniformly (1.9 to >2.25 km/s) from 490 to 512 mbsf, whereas magnetic susceptibility is variable but decreases steadily. Density and resistivity values remain relatively constant (1.75 g/cm^3 and 1 Ωm, respectively). The steady co-varying increase and decrease in different logging values broadly correlates to the uniform increase in carbonate content from its low value at approximately 390 mbsf (see Fig. 27).

Logging Unit 2 contains one major change in log character and several notable anomalies. A distinct spike anomaly at 442 mbsf marks an abrupt increase in the amplitude of variation of the velocity, density, resistivity, and PEF curves. In addition, there is a subtle step increase in density (>1.75 g/cm^3) and resistivity (>1 Ωm) values. The anomaly at 442 mbsf is defined by isolated maxima in Th, U, and magnetic susceptibility, along with minima in velocity and sinusoidal variations in density and PEF, and an inflection point in resistivity. The FMS image reveals a distinct low-resistivity band that varies in thickness depending on azimuth in the borehole (~15 cm thick). Core photographs reveal a dark, heavily bioturbated ash at this depth (Section 165-1000A-48X-2; see core photos in Section 4), which lies just above a lithologic change to increasing micrite content ("Lithostratigraphy" section, this chapter).

Uranium concentrations become relatively elevated (but highly variable) from 365 to 510 mbsf and reach several broad (~10 m) maxima (2.5–3.5 ppm) within this depth range (Fig. 48). A nearly continuous interval of elevated U concentration from 458 to 490 mbsf contains two absolute maxima exceeding 3 ppm. Uranium is often associated with organic matter in carbonates, and the high U concentrations broadly correlate to the interval from 450 to 515 mbsf, where a hydrocarbon smell emanating from Cores 165-1000A-49X to 55X is reported ("Lithostratigraphy" section, this chapter). In addition, a zone of enriched volatile hydrocarbons is reported from 400 to 510 mbsf, coupled with elevated total organic carbon from approximately 360 to 510 mbsf (see Fig. 27).

Logging Unit 3 (512–582 mbsf)

Logging Unit 3 is defined by a step increase in velocity (2.25–2.50 km/s), density (1.75–1.90 g/cm^3), and resistivity (1.0–1.5 Ωm; the step in resistivity occurs at 520 mbsf). An abrupt increase in the frequency and amplitude of variations in these logging curves, as well as in PEF and magnetic susceptibility values, also define logging Unit 3. The total gamma-ray (SGR) response is somewhat more transitional and follows the U concentration, which reaches a large maximum at 487 mbsf and rapidly decreases from that level, exhibiting higher frequency variations throughout logging Units 3 and 4. Finally, an increase in isolated maxima in Th and K concentrations is observed beginning at 520 mbsf.

Logging Unit 3 corresponds to lithologic Subunit IIA, which is distinguished by an abrupt downcore increase in lithification, and consists of limestone with clay, foraminifers, and interbedded ash layers, which increase in frequency and thickness below 520 mbsf (see the "Lithostratigraphy" and "Igneous Petrology and Volcanology" sections, this chapter). The logging responses are consistent with a general increase in lithification (decrease in porosity and increased cementation) with significant variability in relative lithification. The variations in SGR, susceptibility, and PEF logs also indicate variability in relative proportions of sediment types or mineralogy. The changes in relative lithification are associated with lithology (i.e., low porosity limestone vs. higher porosity limestone with increasing clay, foraminifers, pelagic turbidites, and/or ash content).

A distinct logging response from 560 to 568 mbsf is defined by two closely spaced minima in resistivity, density, and velocity with high-amplitude variations in magnetic susceptibility. No distinct

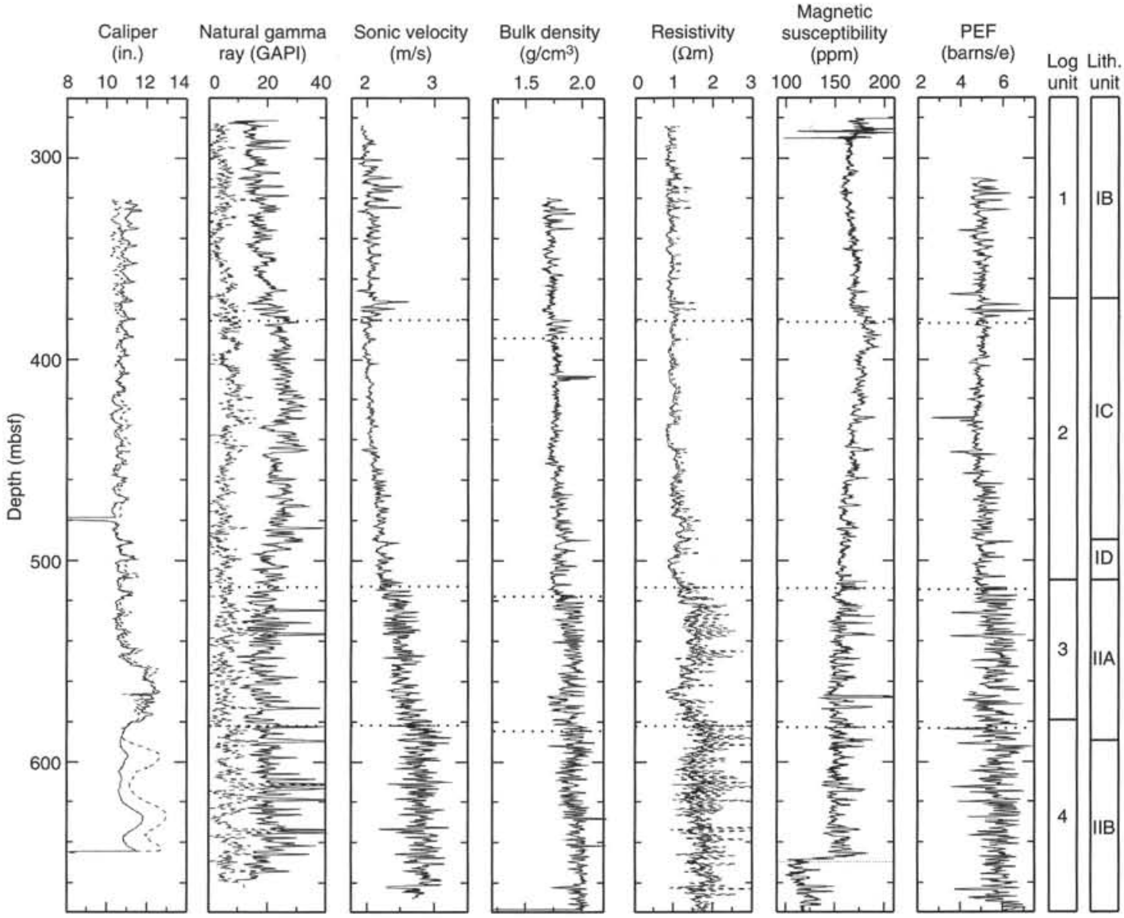

Figure 47. Selected downhole logs from Quad combo and FMS tool strings for the interval from 270 to 675 mbsf in Hole 1000B: calipers from the FMS (C1 perpendicular to C2), total natural gamma ray (SGR; solid line) and natural gamma-ray corrected for uranium content (CGR; dashed line), sonic velocity, bulk density, resistivity from the deep and spherically focused resistivity tools (solid and dashed lines, respectively), magnetic susceptibility from the GHMT, and photoelectric effect (PEF) from the Quad combo tool string. Depth intervals of logging units are marked by dotted lines. The lithologic units are defined in the "Lithostratigraphy" section (this chapter). Sonic velocity, resistivity, and density reflect the porosity of the formation and therefore the degree of lithification or cementation.

change in gamma-ray counts is observed. This anomaly correlates to Core 165-1001B-9R (~20% recovery), which consists of nannofossil micritic limestone with foraminifers. The logging data indicate that the majority of the cored interval consists of less lithified material that is not necessarily extremely high in ash and or clay content. XRD analysis reveals a much reduced concentration of opal-CT at this depth. A broader zone from 550 to 582 mbsf is characterized by generally lower resistivity and density and a steady increase in velocity.

Logging Unit 4 (582–675 mbsf)

Logging Unit 4 is characterized by a further increase in the amplitude of variation in velocity, density, and resistivity data, which all reach absolute maximum values in this interval. Isolated, extreme maxima in Th/U also become more frequent in logging Unit 4 (Fig. 48).

Logging Unit 4 corresponds to the bottom 10 m of lithologic Subunits IIA (590–695.5 mbsf) and IIB to the total depth of logging (~688 mbsf). Lithologic Subunit IIB is composed of limestone and is distinguished from Subunit IIA by an increase in turbidites with coarse-grained (silt/sand) bases composed of foraminifers, a decrease in clay content, and maximum abundance of relatively thick, coarse-grained volcanic ash layers (see the "Lithostratigraphy" and "Igneous Petrology and Volcanology" sections, this chapter). The logging response that defines Unit 4 is consistent with a generally more massive limestone with lower clay content, interbedded with volcanic ash and sandy layers (turbidites). One particularly distinct anomaly at 634 mbsf is marked by a closely spaced double peak in K and Th and a broad Th/U maximum, accompanied by co-varying double minima in velocity and resistivity and a single density minima. This interval falls within Core 165-1000B-16R, where two thick ash layers (31 and 14 cm) are separated by 1.48 m. The FMS image clearly shows two low-resistivity bands of comparable thickness and separation; however, four additional, distinct low-resistivity bands are revealed in the FMS image within a 2-m interval, which correlate well with much thinner ash layers (1–7 cm thick) apparent in the core photos (see Section 4 and the "Igneous Petrology and Volcanology" section, this chapter). The non-FMS logging tools appear capable of detecting the two thickest ash layers (31 and 14 cm) while the FMS image reveals all ash layers reported within this zone. Ash layers within the limestones at Site 1000 appear particularly distinctive on FMS images, although comparable thick ash layers within the turbidites cored at Site 998 were essentially indistinguishable with FMS.

Acoustic Velocities

Compressional velocity data derived from the sonic log, which extends from 275 to 666 mbsf, were merged with compressional ve-

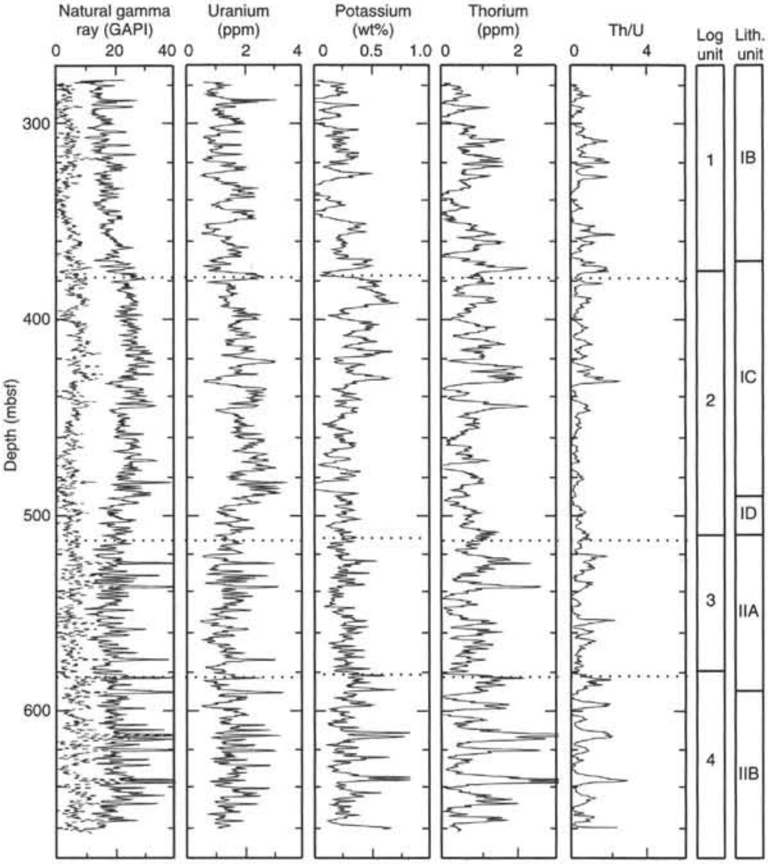

Figure 48. Downhole logs from the natural gamma-ray spectrometry tool on the Quad combo tool string for the interval from 275 to 660 mbsf in Hole 1000B: total gamma ray (SGR; solid line), gamma-ray counts for Th and K only (dashed line), uranium concentration, potassium (wt%), thorium concentration, and thorium/uranium ratio. Depth intervals of logging units are marked by dotted lines. Generally, maxima in the above elements and elemental ratios correlate with discrete ash fall layers. Intervals of elevated uranium concentration are associated with zones of enriched volatile hydrocarbons and total organic carbon.

locities measured on split cores by the DSV or with a Hamilton Frame apparatus from 0 to 275 mbsf and from 666 to 690 mbsf (see "Physical Properties" section, this chapter). The laboratory velocity data were corrected to in situ stress by the empirical relation derived by Urmos et al. (1993) (Table 18; Fig. 43). The merged velocities were integrated over the interval from 0 to 690 mbsf to produce a plot of two-way traveltime vs. depth (Fig. 49). The resultant traveltime vs. depth curve (Fig. 49) is used to tie the cored sequences at Site 1000 to the seismic reflection data over the site. A summary of these correlations is discussed in the "Summary and Conclusions" section (this chapter).

Geological High-Sensitivity Magnetic Tool

Total induction and magnetic susceptibility, respectively, were recorded by the scaler magnetometer (NMRS) and the susceptometer (SUMS). A detailed review of these sensors and principles of magnetic logging are provided in the "Explanatory Notes" chapter (this volume). During the time interval that the geological high-sensitivity magnetic tool (GHMT-A) recorded data, the measured total field and susceptibility logs can be affected by time-dependent factors such as transient variations in the Earth's field and temperature drift. A repeat pass of the GHMT-A tool permits analysis of the time-dependent components of the borehole magnetic environment that affect the measurement of magnetization of the surrounding formation. The time-invariant components of the measured field (magnetic mineral concentration, remanent magnetization) can then be examined. Postcruise data processing will further isolate and quantify both time-dependent and time-invariant factors, and may provide results on the orientation of the paleomagnetic field. We discuss the quality of magnetometer and susceptometer data in the following sections.

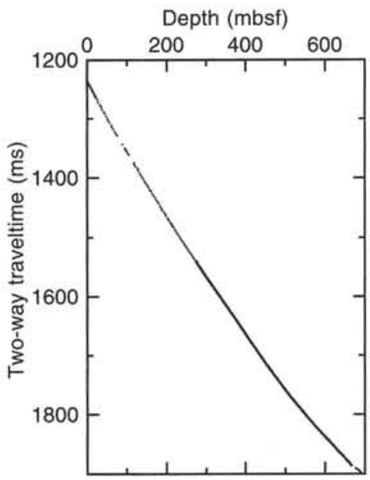

Figure 49. Two-way traveltime vs. depth calculated from merged compressional velocities derived from the sonic log (275–666 mbsf) and physical properties measurements (0–275 and 666–690 mbsf) corrected for in situ stress in Hole 1000B. The resultant traveltime vs. depth curve is used to tie the cored sequences at Site 1000 to seismic reflection data over the site (Fig. 53).

Total Induction Log

We removed the contribution of the Earth's magnetic field Br, using the IGRF value of 40585 nT, from the total field B measured by the magnetometer. Figure 50 shows the remaining "local" field for

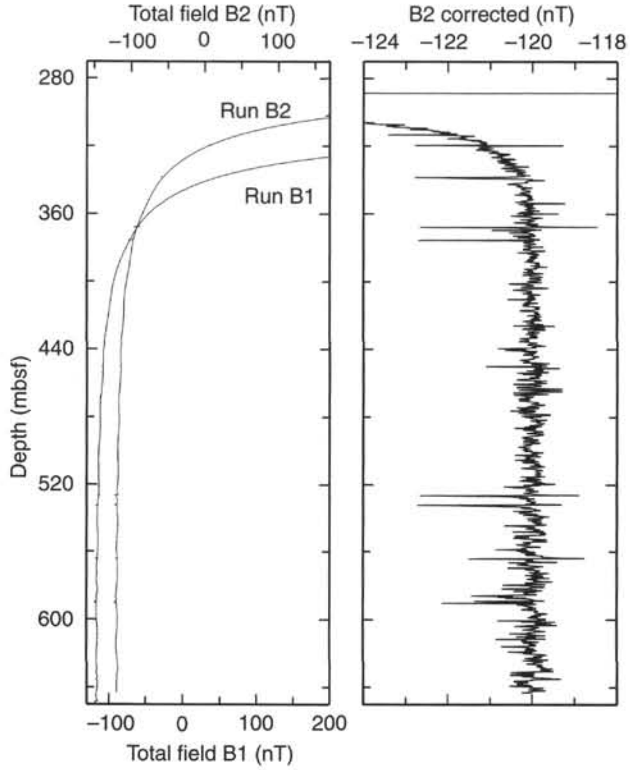

Figure 50. "Local" total magnetic induction for the two runs (B1 and B2) and the resulting induction after correction for pipe effect (B2 corrected). Part of the total induction has been obtained by correcting the total induction for the main dipolar field. Scale shift between runs is 30 nT.

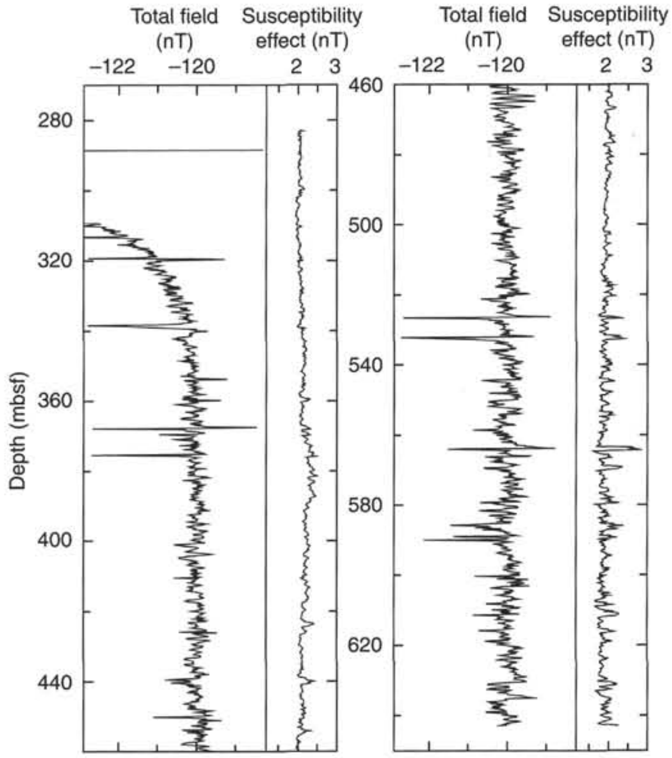

Figure 51. "Local" total induction, after correction for pipe effect (B2 corrected), and downhole induction due to the susceptibility effect (run B2). Correlations and anti-correlations of these logs indicate that magnetostratigraphy may be determined with further post-cruise processing.

the two runs (B1 and B2), containing only local effects, that is, $B1(z) = Bf(z) + Ba(z) + Bt1(z,t)$ and $B2(z) = Bf(z) + Ba(z) + Bt2(z,t)$.

There is a shift toward high values between 430 and 320 mbsf for the first run and between 400 and 300 mbsf for the second run, caused by the highly magnetic bottom-hole assembly (BHA). The depth shift of this deviation between both runs is caused by the deeper pipe during the first run. The data show very little magnetic variation, and the average values of the "local" fields B1 and B2 are slightly lower than zero. The true value of Bf, the magnetization component of the formation, can be obtained by evaluating the anomaly field Ba and the transient fields Bt1 and Bt2.

Analysis of the Components of the Magnetic Induction

Data from the two runs B1 and B2 are quite similar (Fig. 50), except for the effect caused by the different depths of the pipe, and indicate that there were no significant temporal changes in the external Earth's field. The remaining "local" B field for the second run after correction for pipe effect (B2 corrected) is shown on Figure 50. This drill-pipe perturbation can usually be removed, assuming a dipolar effect, and allows for data recovery up to about 10 m beneath the BHA. The very small variations observed on these data (compared with the results of Site 998, for example) can be due to the low latitude and mainly to the low susceptibility of the weakly magnetized rock formation. An overall negative value of the remaining "local" field (B2 corrected) was observed, and centered around −120 nT.

Analysis of Susceptibility Records

The magnetic susceptibility data in Hole 1000B appear to be of good quality (Fig. 51). There is a good correlation between the records, indicating there were few measurement errors and little thermal drift of the measurement coils, but both runs are shifted by about 20 ppm. The susceptibility log is presented in Figure 47 and is compared with other logging data in the logging unit portion of the "Downhole Measurements" section, this volume.

Comparison of Total Field and Susceptibility Logs

Figure 51 shows the comparison between the "local" B field, obtained from the second magnetometer run (B2 corrected), with the induced magnetization field (Bfi) calculated from the susceptibility recorded during the second run, using the following relation:

$$Bfi = Br \cdot k \cdot [1 - 3 \cdot \sin^2(I)]/2,$$

where k is the susceptibility, and Br and I are the intensity and the inclination of the actual Earth's field, respectively. Bfi corresponds to the susceptibility effect on the total field. These two logs show correlations and anticorrelations, which may indicate that these logs could be used to determine polarity reversals with further post-cruise processing, as indicated by the remanent magnetization measurements (see "Paleomagnetism" section, this chapter). Probable reduction diagenesis prevented the primary remanent magnetization from being preserved.

SUMMARY AND CONCLUSIONS

The one thousandth site of a combined DSDP/ODP was cored in the region of the Caribbean, on the NNR, where the first long core was recovered in 1963. The NNR extends from Honduras and Nicaragua to the island of Jamaica. A series of channels dissects the carbonate shelves and isolated carbonate banks that define the east-northeast-trending rise (Fig. 1). The deepest and widest of these passageways is Pedro Channel. Site 1000 is located in Pedro Channel on the eastern flank of Rosalind Bank, away from any obvious debris flow channels (Fig. 2). The NNR is bounded to the north by the Cayman Trough and to the southeast by the lower Nicaraguan Rise and the Hess Escarpment.

One of our principal objectives at Site 1000 was to reach the top of a carbonate platform and document the onset of the Caribbean Current. It has been proposed that the NNR was a large carbonate platform during much of the Paleogene, and that it ultimately became segmented as a result of tectonic activity along the northern Caribbean Plate boundary, including the opening of the Cayman Trough. The Pedro Channel represents one of the largest segments of the once contiguous megabank, originally thought to have foundered during middle Miocene time (e.g., Droxler et al., 1992). The carbonate platform proved to be deeper and older than predicted. The thick and continuous 20-m.y. record of pelagic sedimentation cored at Site 1000, however, provides many new insights into the history of Caribbean subthermocline (intermediate) water masses during the Neogene, the segmentation and subsidence history of the NNR, the seismic stratigraphy of the region, and a record of explosive volcanism during the Neogene (Figs. 52, 53).

Nearly 700 m of continuous lower Miocene–Holocene periplatform carbonates were recovered. The average sedimentation rate for the Neogene section at Site 1000 was 34.8 m/m.y. Estimates of the age of the sediments at the base of Hole 1000B is 20.0–20.3 Ma. Pelagic sedimentation of biogenic carbonate has dominated the Neogene history of sedimentation at this site, but other components, such as terrigenous clays and volcanic ash, also contribute to the character of the sediment in Pedro Channel. Terrigenous material accounts for about 10% of the section and dispersed ash about 7% (see "Inorganic Geochemistry" section, this chapter). What distinguishes these and other periplatform carbonates from other types of calcareous ooze and chalk is the contribution of bank-derived fine-grained aragonite and other carbonate particles (i.e., micrite). The upper 513 m of Site 1000 (lithologic Unit I) is characterized by nannofossil and micritic oozes with foraminifers to micritic nannofossil chalk with foraminifers. Interbedded ash layers occur in parts of Unit I, particularly in the intervals 0–40, 140–370, and 425–513 mbsf. Thin layers of graded foraminiferal sands (turbidites) are present in the middle part of Unit I (240–400 mbsf). An interval of micritic nannofossil chalk with clay to clayey nannofossil chalk (370.5–486.0 mbsf) correlates with the carbonate crash recognized at the two deeper water sites (998 and 999) of Leg 165.

Sedimentation and mass accumulation rates (MARs) in the upper Pliocene–Pleistocene interval (0.0–2.8 Ma) averaged 27.3 m/m.y. and 2.4–3.4 g/cm^2/k.y., respectively. This pattern of declining MARs through the Pleistocene has been a common feature of Sites 998, 999, and 1000. The upper Miocene to upper Pliocene interval (2.8–9.6 Ma) accumulated at relatively uniform rates of 37.2 m/m.y., or 3.5–5.0 g/cm^2/k.y. Another notable feature of the Pliocene is the abrupt increase in carbonate MARs at about 4.1–4.2 Ma. The observed pulse of enhanced carbonate MARs in the mid-Pliocene could be an expression of the closing of the Central American Seaway, resulting in increased circulation vigor of the Caribbean Current and enhanced carbonate productivity (topographic upwelling or island effect). Alternatively, changes in conveyor circulation or intermediate water sources may account for the observed changes in carbonate MARs.

Lithologic Subunits IC and ID are micritic nannofossil chalk and clayey nannofossil chalk. This interval (9.6–13.5 Ma) includes the carbonate crash in the middle/upper Miocene boundary interval and displays the highest sedimentation and accumulation rates of the section, averaging 47.0 m/m.y. (4.5–7.5 g/cm^2/k.y.). The most distinctive pattern in this part of the section is the peak in noncarbonate MARs associated with the carbonate crash, a trend also observed at Sites 998 and 999.

The carbonate crash interval, in the transition from the middle Miocene to the upper Miocene, is characterized by higher magnetic susceptibility, distinctly lower but highly variable carbonate contents, increased noncarbonate MARs, enrichments of up to 0.8% TOC (in the interval from ~360 to 510 mbsf), and relatively high concentrations of uranium (from downhole natural gamma measurements). The organic matter is primarily terrestrial in origin (see "Organic Geochemistry" section, this chapter). Sulfate reduction is more pronounced at Site 1000 when compared with Sites 998 and 999, with sulfate concentrations approaching zero by 350–400 mbsf (the top of the carbonate minimum and hydrocarbon enrichment zones). Indeed, paleomagnetic intensities indicate that all but the upper 22.5 m of the section have been severely affected by reduction diagenesis. There are also enrichments of volatile hydrocarbons in the interval from ~400 to 520 mbsf. Migration of hydrocarbons (updip and/or upsection) into the interval of the carbonate minimum is suspected due to the shallow burial and the absence of an anomalously high thermal gradient. The increased clay content in this interval may inhibit further upward migration by behaving somewhat as a permeability barrier. The relatively enriched TOC values in this zone are genetically unrelated to the enriched hydrocarbons, and can be ascribed to a terrigenous source associated with the greater abundance of detrital clays in this interval. In situ generation of thermogenic gases within the hydrocarbon zone is not supported, although bacterial methanogenesis may be a factor for the occurrence of C_1 in this zone given the absence of sulfate at this depth. Increased alkalinity associated with sulfate reduction in the carbonate minimum and hydrocarbon zone may be responsible for the precipitation of carbonate cements along a lithification front represented by the abrupt change from chalk to limestone at about 510 mbsf (lithologic Unit I/II boundary).

The interval from 513.4 to 695.9 mbsf corresponds to lithologic Unit II and is composed of calcareous limestone and nannofossil micritic limestone with clay and foraminifers (see "Lithostratigraphy" section, this chapter). Turbidites are common in the basal part of Unit II (591–696 mbsf). Many of the turbidites contain redeposited pelagic sediments, but some also contain material derived from the upper reaches or tops of the adjacent carbonate banks. For example, Sample 165-1000B-17R-5, 141–143 cm, comes from the coarse basal part of a turbidite that contains numerous specimens of carbonate platform benthic foraminifers (Fig. 17). Volcanic ashes increase in frequency and cumulative thickness in the lower part of the cored sequence at Site 1000, corresponding to the early Miocene to early middle Miocene peak of volcanism also recognized at Sites 998 and 999 (Fig. 40). The lower Miocene–lower middle Miocene interval represented by the limestones and interbedded ash layers and turbidites of lithologic Unit II (13.5–20.0 Ma) had an average sedimentation rate of 27.3 m/m.y. with widely varying bulk mass accumulation rates of 3.5–6.3 g/cm^2/k.y. The greatest variability occurs in the lower Miocene, presumably because of the presence of common volcanic ash layers and turbidites (lithologic Subunit IIB).

The accumulation rate and number of volcanic ash layers during the early to middle Miocene at Site 1000 exhibits a pattern that is remarkably close to that of Site 999, although the magnitude of these parameters are somewhat higher at the latter site. The combined evidence from Sites 998, 999, and 1000 shows that the Miocene explosive volcanic episode generated a principal fallout axis that trends east from the Central American arc, between Sites 999 and 1000, or very close to the latitude of Site 1000. This is consistent with derivation of the tephra from the ignimbrite-forming volcanism in the Tertiary Igneous Province of Central America.

REFERENCES

Austin, J.A., Jr., Schlager, W., et al., 1988. *Proc. ODP, Sci. Results,* 101: College Station, TX (Ocean Drilling Program).

Backman, J., and Shackleton, N.J., 1983. Quantitative biochronology of Pliocene and early Pleistocene calcareous nannofossils from the Atlantic, Indian and Pacific oceans. *Mar. Micropaleontol.,* 8:141–170.

Berggren, W.A., Kent, D.V., Swisher, C.C., III, and Aubry, M.-P., 1995. A revised Cenozoic geochronology and chronostratigraphy. *In* Berggren, W.A., Kent, D.V., Aubry, M.-P., and Hardenbol, J. (Eds.), *Geochronology, Time Scales and Global Stratigraphic Correlation.* Spec. Publ.—Soc. Econ. Paleontol. Mineral., 54:129–212.

Berggren, W.A., Kent, D.V., and Van Couvering, J.A., 1985. The Neogene, Part 2. Neogene geochronology and chronostratigraphy. *In* Snelling, N.J. (Ed.), *The Chronology of the Geological Record.* Geol. Soc. London Mem., 10:211–260.

Blow, W.H., 1969. Late middle Eocene to Recent planktonic foraminiferal biostratigraphy. *In* Brönnimann, P., and Renz, H.H. (Eds.), *Proc. First Int. Conf. Planktonic Microfossils, Geneva, 1967:* Leiden (E.J. Brill), 1:199–422.

Bolli, H.M., Boudreaux, J.E., Emiliani, C., Hay, W.W., Hurley, R.J., and Jones, J.I., 1968. Biostratigraphy and paleotemperatures of a section cored on the Nicaragua Rise, Caribbean Sea. *Geol. Soc. Am. Bull.,* 79:459–470.

Bryan, J.A., and Huddleston, P.F., 1991. Correlation and age of the Bridgeboro limestone, a coralgal limestone from southwestern Georgia. *J. Paleontol.,* 65:864–868.

Chaisson, W.P. and Pearson, P.N., in press. Planktonic foraminifer biostratigraphy at Site 925, western tropical Atlantic: the last 12 m.y. *In* Shackleton, N.J., Curry, W.B., Richter, C., and Bralower, T.J. (Eds.), *Proc. ODP, Sci. Results,* 154: College Station, TX (Ocean Drilling Program).

Channell, J.E.T., and Hawthorne, T., 1990. Progressive dissolution of titanomagnetites at ODP Site 653 (Tyrrhenian Sea). *Earth Planet. Sci. Lett.,* 96:469–480.

Cofer-Shabica, N.B., 1987. The late Pleistocene deep water history of the Venezuela Basin in the Eastern Caribbean Sea [M.S. thesis]. Univ. of Miami, Coral Gables, FL.

Cole, W.S., 1967. A review of American species of miogypsinids (larger foraminifera). *Contrib. Cushman Lab. Foraminiferal Res.,* 18:99–117.

Cunningham, A., Droxler, A.W., and Hine, A.C., 1995. Neogene/Quaternary evolution of Pedro Channel, Northern Nicaragua Rise: the strike-slip induced breakup of a carbonate megabank in a plate boundary zone. *AAPG Annual Meeting Abstracts,* A20. (Abstract)

Curry, W.B., Shackleton, N.J., Richter, C., et al., 1995. *Proc. ODP, Init. Repts.,* 154: College Station, TX (Ocean Drilling Program).

Dolan, P.B., 1972. Genesis and distribution of recent sediments on the Pedro Bank south of Jamaica [Ph.D. dissert.]. Univ. College, London.

Droxler, A.W., Cunningham, A., Hine, A.C., Hallock, P., Duncan, D., Rosencrantz, E., Buffler, R., and Robinson, E., 1992b. Late middle(?) Miocene segmentation of an Eocene–early Miocene carbonate megabank on the northern Nicaragua Rise tied to the tectonic activity at the North America/Caribbean plate boundary zone. *Eos,* (Suppl. 43), 73:299. (Abstract)

Droxler, A.W., Haddad, G.A., Mucciarone, D.A., and Cullen, J.L., 1990. Pliocene-Pleistocene aragonite cyclic variations in Holes 714A and 716B (The Maldives) compared with Hole 633A (The Bahamas): records of climate-induced $CaCO_3$ preservation at intermediate water depths. *In* Duncan, R.A., Backman, J., Peterson, L.C., et al., *Proc. ODP, Sci. Results,* 115: College Station, TX (Ocean Drilling Program), 539–577.

Droxler, A.W., Morse, J.W., Glaser, K.S., Haddad, G.A., and Baker, P.A., 1991. Surface sediment carbonate mineralogy and water column chemistry: Nicaragua Rise versus the Bahamas. *Mar. Geol.,* 100:277–289.

Droxler, A.W., Schlager, W., and Whallon, C.C., 1983. Quaternary aragonite cycles and oxygen isotope record in Bahamian carbonate ooze. *Geology,* 11:235–239.

Emiliani, C., 1981. A new global geology. *In* Emiliani, C. (Ed.), *The Sea* (Vol. 7)*: The Oceanic Lithosphere:* New York (Wiley), 1687–1728.

Froelich, P.N., Klinkhammer, G.P., Bender, M.L., Luedtke, N.A., Heath, G.R., Cullen, D., Dauphin, P., Hammond, D., Hartman, B., and Maynard, V., 1979. Early oxidation of organic matter in pelagic sediments of the eastern equatorial Atlantic: suboxic diagenesis. *Geochim. Cosmochim. Acta,* 43:1075–1090.

Gehman, H.M., Jr., 1962. Organic matter in limestones. *Geochim. Cosmochim. Acta,* 26:885–897.

Gieskes, J.M., 1983. The chemistry of interstitial waters of deep-sea sediments: interpretation of deep-sea drilling data. *In* Riley, J.P., and Chester, R. (Eds.), *Chemical Oceanography* (Vol. 8): London (Academic), 221–269.

Glaser, K.S., 1992. Quaternary periplatform sediments and environments on the northeastern Nicaragua Rise, Caribbean Sea [Ph.D. dissert.]. Rice Univ., Houston.

Glaser, K.S., and Droxler, A.W., 1991. High production and highstand shedding from deeply submerged carbonate banks, northern Nicaragua Rise. *J. Sediment. Petrol.,* 61:126–142.

————, 1993. Controls and development of late Quaternary periplatform carbonate stratigraphy in Walton Basin (northeastern Nicaragua Rise, Caribbean Sea). *Paleoceanography,* 8: 243–274.

Gomberg, D., 1974. Geology of the Portales Terrace. *Fl. Sci.,* 37 (Suppl. 1):15.

Haddad, G.A., 1994. Calcium carbonate dissolution patterns at intermediate water depths of the tropical oceans. [Ph.D. dissertation], Rice Univ., Houston.

Haddad, G.A., Droxler, A.W., Kroon, D., and Müller, D.W., 1993. Quaternary $CaCO_3$ input and preservation within Antarctic intermediate water: mineralogic and isotopic results from Holes 818B and 817A, Townsville Trough (northeastern Australia margin). *In* McKenzie, J.A., Davies, P.J., Palmer-Julson, A., et al., *Proc. ODP, Sci. Results,* 133: College Station, TX (Ocean Drilling Program), 203–233.

Hallock, P., Hine, A.C., Vargo, G.A., Elrod, J.A., and Jaap, W.C., 1988. Platforms of the Nicaragua Rise: examples of the sensitivity of carbonate sedimentation to excess trophic resources. *Geology,* 16:1104–1107.

Haq, B.U., Hardenbol, J., and Vail, P.R., 1987. Chronology of fluctuating sea levels since the Triassic. *Science,* 235:1156–1167.

Hine, A.C., Locker, S.D., Tedesco, L.P., Mullins, H.T., Hallock, P., Belknap, D.F., Gonzales. J.L., Neumann, A.C., and Neumann, S.W., 1992. Megabreccia shedding from modern, low-relief carbonate platforms, Nicaraguan Rise. *Geol. Soc. Am. Bull.,* 104:928–943.

JOIDES, 1965. Ocean drilling on the continental margin. *Science,* 150:709–716.

Kennett, J.P., and Srinivasan, M.S., 1983. *Neogene Planktonic Foraminifera: A Phylogenetic Atlas:* Stroudsburg, PA (Hutchinson Ross).

Krom, M.D., and Berner, R.A., 1980. Adsorption of phosphate in anoxic marine sediments. *Limnol. Oceanogr.,* 25:797–806.

————, 1983. A rapid method for the determination of organic and carbonate carbon in geological samples. *J. Sediment. Pet.,* 53:660–663.

Leslie, B.W., Hammond, D.E., Berelson, W.M., and Lund, S.P., 1990. Diagenesis in anoxic sediments from the California continental borderland and its influence on iron, sulfur, and magnetite behavior. *J. Geophys. Res.,* 95:4453–4470.

Liu, J.D. and Cotillon, P., 1989. Present and recent sedimentation in the Loyalty Basin along Thio-Lifou profile (New Caledonia, Southwest Pacific). *Mar. Geol.,* 78:109–123.

Lyle, M., Dadey, K.A., and Farrell, J.W., 1995. The late Miocene (11–8 Ma) eastern Pacific carbonate crash: evidence for reorganization of deepwater circulation by the closure of the Panama Gateway. *In* Pisias, N.G., Mayer, L.A., Janecek, T.R., Palmer-Julson, A., and van Andel, T.H. (Eds.), *Proc. ODP, Sci. Results,* 138: College Station, TX (Ocean Drilling Program), 821–838.

Martens, C.S., and Berner, R.A., 1974. Methane production in the interstitial waters of sulfate-depleted marine sediments. *Science,* 185:1167–1169.

Millero, F.J., and Sohn, M.L., 1992. *Chemical Oceanography:* Boca Raton (CRC Press).

Mullins, H.T., Gradulski, A.F., Hine, A.C., Melillo, A.J., Wise, S.W., Jr., and Applegate, J., 1988. Three-dimensional sedimentary framework of the carbonate ramp slope of central west Florida: a sequential seismic stratigraphic perspective. *Geol. Soc. Am. Bull.,* 100:514–533.

Mullins, H.T., Gardulski, A.F., Wise, S.W., and Applegate, J., 1987. Middle Miocene oceanographic event in the eastern Gulf of Mexico: implications for seismic stratigraphic succession and Loop Current/Gulf Stream circulation: *Geol. Soc. Am. Bull.,* 98:702–713.

Mullins, H.T., and Neumann, A.C., 1977. Miocene submarine erosion in the northern Straits of Florida. *Geol. Soc. Am.,* 9:170–171. (Abstract)

————, 1979. Geology of the Miami Terrace and its paleoceanographic implications. *Mar. Geol.,* 30:205–232.

Mullins, H.T., Neumann, A.C., Wilber, R.J., Hine, A.C., and Chinburg, S.J., 1980. Carbonate sediment drifts in the northern Straits of Florida. *AAPG Bull.,* 64:1701–1717.

Okada, H., and Bukry, D., 1980. Supplementary modification and introduction of code numbers to the low-latitude coccolith biostratigraphic zonation (Bukry, 1973; 1975). *Mar. Micropaleontol.,* 5:321–325.

Peters, K.E., 1986. Guidelines for evaluating petroleum source rock using programmed pyrolysis. *AAPG Bull.,* 70:318–329.
Popenoe, P., 1985. Cenozoic depositional and structural history of the North Carolina margin from seismic stratigraphic analyses. *In* Poag, C.W. (Ed.), *Geologic Evolution of the United States Atlantic Margin:* New York (Van Nostrand Reinhold), 125–187.
Prell, W.L., Gardner, J.V., et al., 1982. *Init. Repts. DSDP,* 68: Washington (U.S. Govt. Printing Office).
Raffi, I., Backman, J., Rio, D., and Shackleton, N.J., 1993. Plio-Pleistocene nannofossil biostratigraphy and calibration to oxygen isotopes stratigraphies from Deep Sea Drilling Project Site 607 and Ocean Drilling Program Site 677. *Paleoceanography,* 8:387–408.
Reid, R.P., Carey, S.N., and Ross, D.R., 1996. Late Quaternary sedimentation in the Lesser Antilles Island Arc. *Geol. Soc. Am. Bull.,* 108:78–100.
Reynolds, J.H., 1980. Late Tertiary volcanic stratigraphy of northern Central America. *Bull. Volcanol.,* 43:601–607.
Robinson, E., 1976. *Walton Basin and Pedro Bank bathymetric map,* Geol. Surv. Jamaica.
Robinson, E., 1994. Jamaica. *In* Donovan, S.K., and Jackson, T.A. (Eds.), *Caribbean Geology: an Introduction:* Kingston (UWIPA), 111–127.
Robinson, S.G., 1990. Applications for whole-core magnetic susceptibility measurements of deep-sea sediments: Leg 115 results. *In* Duncan, R.A., Backman, J., Peterson, L.C., et al., *Proc. ODP, Sci. Results,* 115: College Station, TX (Ocean Drilling Program), 737–771.
Ruttenberg, K.C., 1992. Development of a sequential extraction method for different forms of phosphorous in marine sediments. *Limnol. Oceanogr.,* 37:1460–1482.
Sato, T., Kameo, K., and Takayama, T., 1991. Coccolith biostratigraphy of the Arabian Sea. *In* Prell, W.L., Niitsuma, N., et al., *Proc. ODP, Sci. Results,* 117: College Station, TX (Ocean Drilling Program), 37–54.
Schlager, W., and James, N.P., 1978. Low-magnesian calcite limestones forming at the deep-sea floor, Tongue of the Ocean, Bahamas. *Sedimentology,* 25:675–702.
Schlager, W., Reijmer, J., and Droxler, A.W., 1994. Highstand shedding of carbonate platforms, *J. Sediment. Res.,* B64:270–281.
Schwartz, J.P., 1996. Late Quaternary periplatform sediments and paleoenvironmental analysis of Pedro Channel, northeastern Nicaraguan Rise, Caribbean Sea [M.S. thesis]. Rice Univ., Houston.
Steiness, E., Heier, K.S., and Billings, G.K., 1972. Lithium. *In* Wedepohl, K.H. (Ed.), *Handbook of Geochemistry* (Vol. 2): Berlin (Springer-Verlag).
Takayama, T., and Sato, T., 1987. Coccolith biostratigraphy of the North Atlantic Ocean, Deep Sea Drilling Project Leg 94. *In* Ruddiman, W.F., Kidd, R.B., Thomas, E., et al., *Init. Repts. DSDP,* 94 (Pt. 2): Washington (U.S. Govt. Printing Office), 651–702.
Tissot, B.P., and Welte, D.H., 1984. *Petroleum Formation and Occurrence* (2nd ed.): Heidelberg (Springer-Verlag).
Triffleman, N.J., Hallock, P., Hine, A.C., and Peebles, M., 1992. Morphology, sediments, and depositional environments of a small, partially drowned carbonate platform: Serranilla Bank, southwest Caribbean Sea. *J. Sediment. Petrol.,* 21:39–47.
Urmos, J., Wilkens, R.H., Bassinot, F., Lyle, M., Marsters, J.C., Mayer, L.A., and Mosher, D.C., 1993. Laboratory and well-log velocity and density measurements from the Ontong Java Plateau: new in-situ corrections to laboratory data for pelagic carbonates. *In* Berger, W.H., Kroenke, L.W., Mayer, L.A., et al., *Proc. ODP, Sci. Results,* 130: College Station, TX (Ocean Drilling Program), 607–622.
Walter, L.M., and Burton, E.A., 1986. The effect of orthophosphate on carbonate mineral dissolution rates in seawater. *Chem. Geol.,* 56:313–323.
Young, J.R., 1990. Size variation of Neogene *Reticulofenestra* coccoliths from Indian Ocean DSDP cores. *J. Micropaleontol.,* 9:71–85.
Zans, V.A., 1958. The Pedro Cays and Pedro Bank: report of survey of the cay (1955–1957). *Geol. Surv. Jamaica,* Kingston, Jamaica, 1–57.

Ms 165IR-105

NOTE: Core-description forms ("barrel sheets") and core photographs can be found in Section 4, beginning on page 403. Forms containing smear-slide data can be found in Section 5, beginning on page 821. Thin-section descriptions are given in Sections 6 and 7, beginning on page 851. See Table of Contents for material contained on CD-ROM.

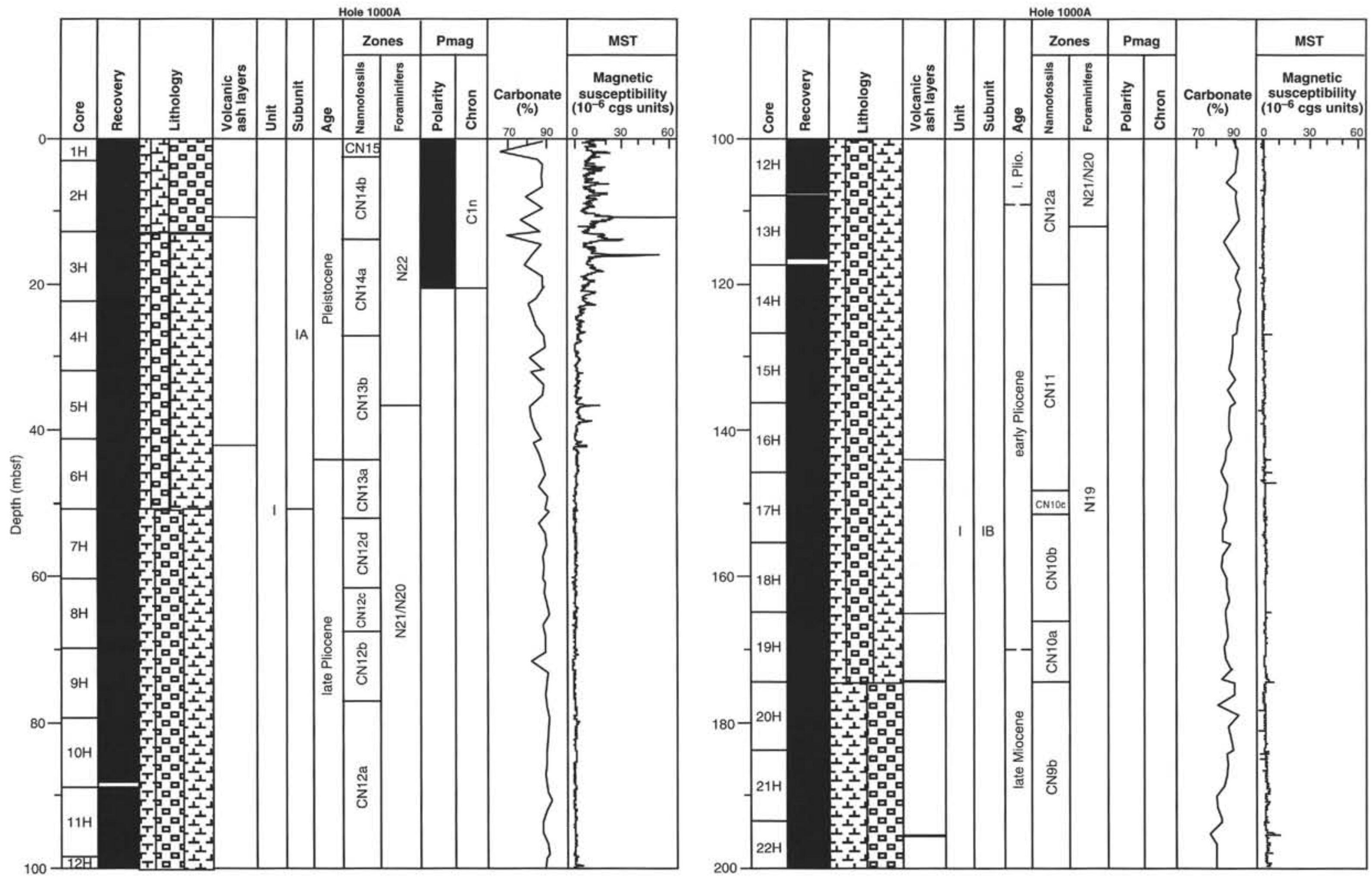

Figure 52. Site 1000 summary column for core recovery, lithology, volcanic ash layer occurrence, lithologic unit and subunit boundaries, ages, nannofossil and foraminiferal datum boundaries, magnetic reversal boundaries, carbonate percentages, MST magnetic susceptibilities, and, for Hole 1000B, *P*-wave velocities from downhole measurements.

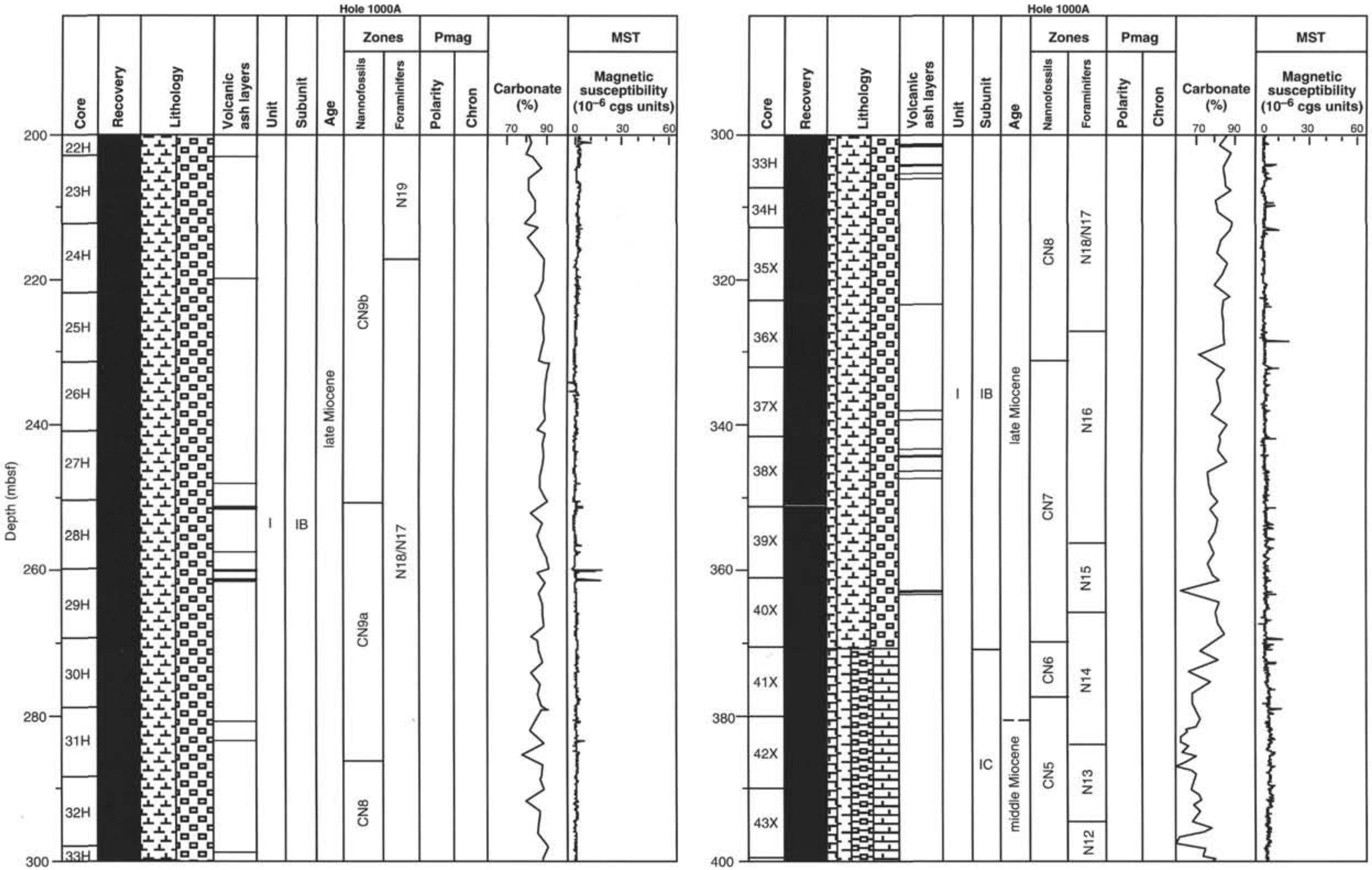

Figure 52 (continued).

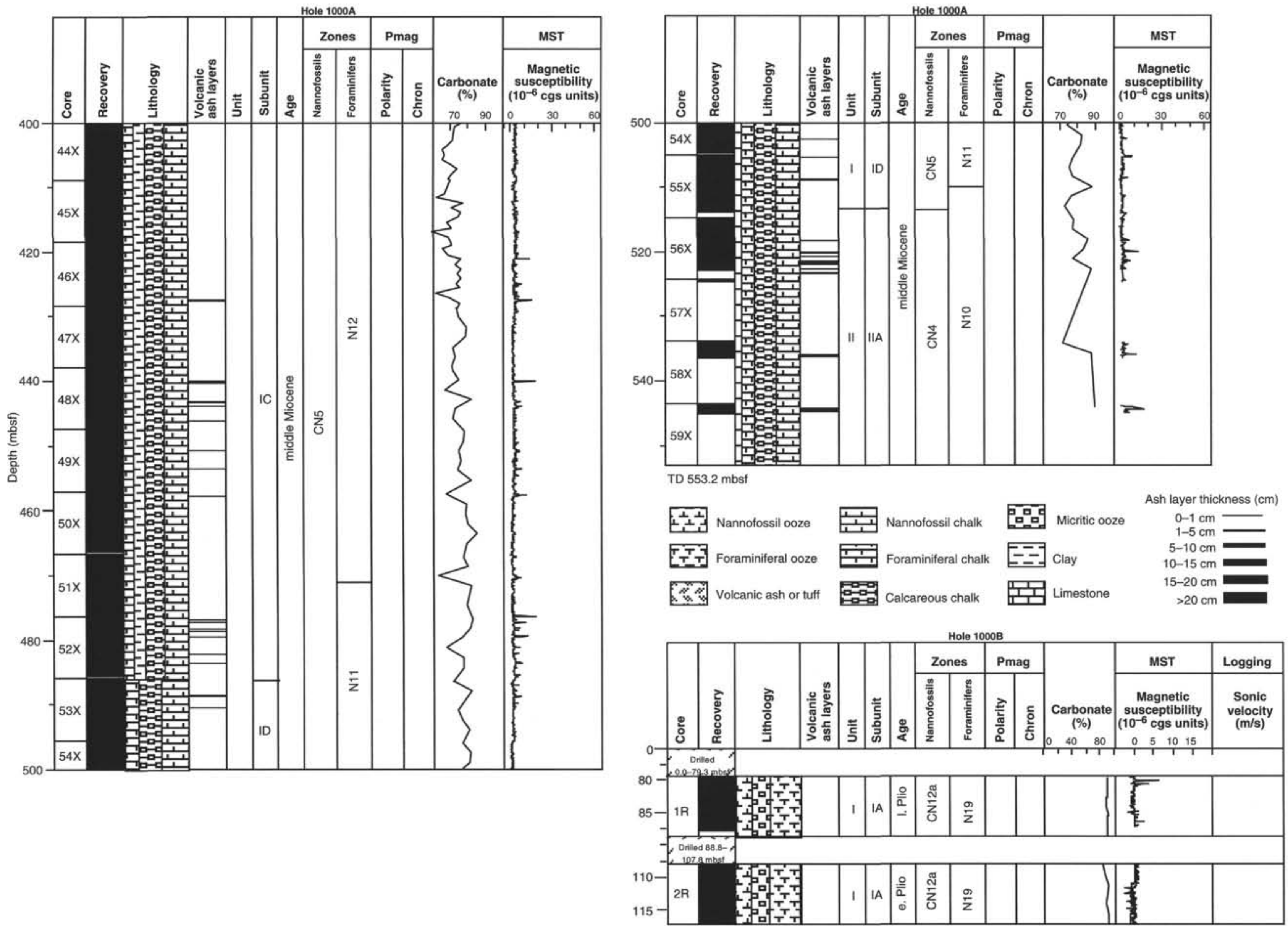

Figure 52 (continued).

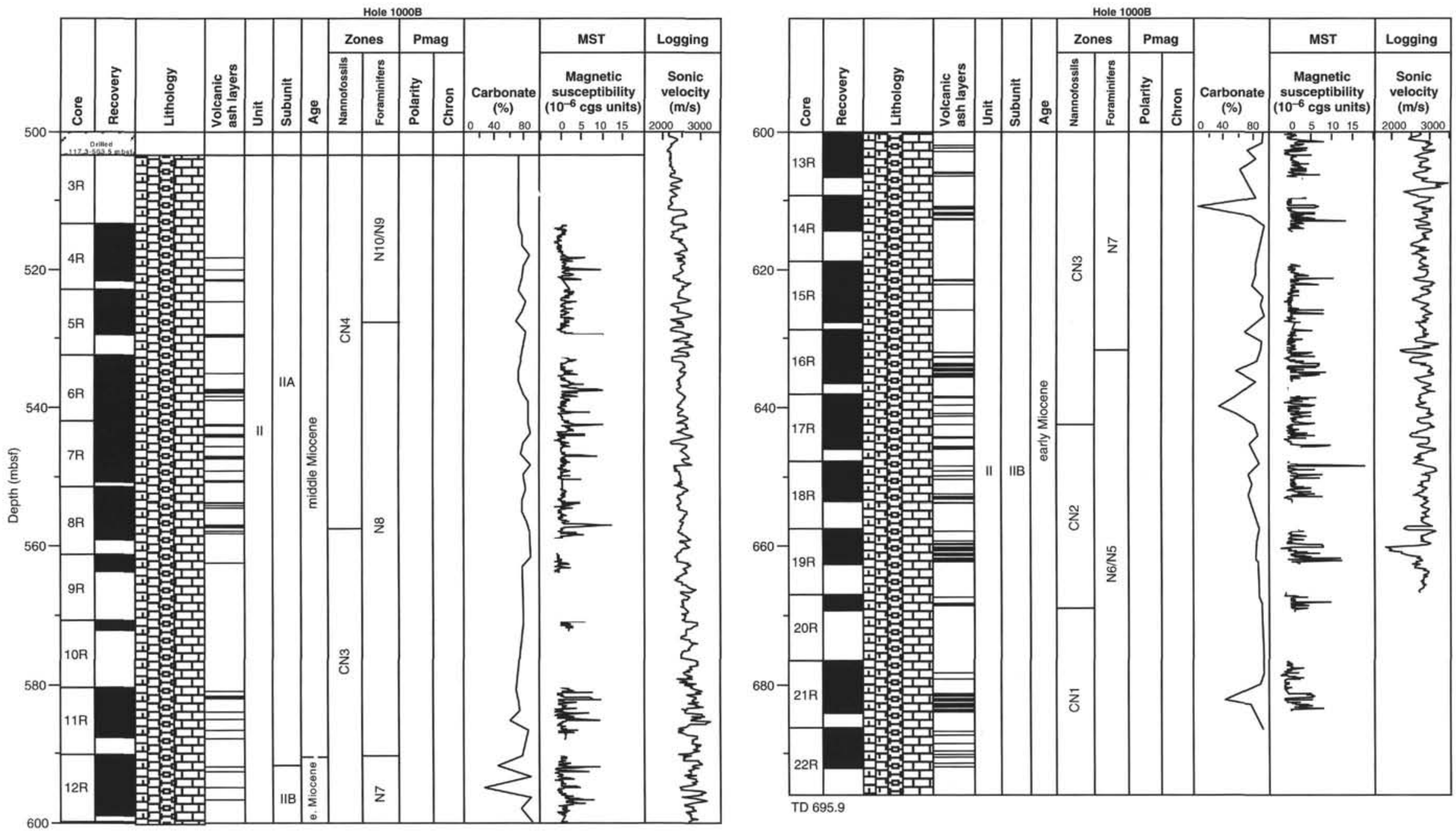

Figure 52 (continued).

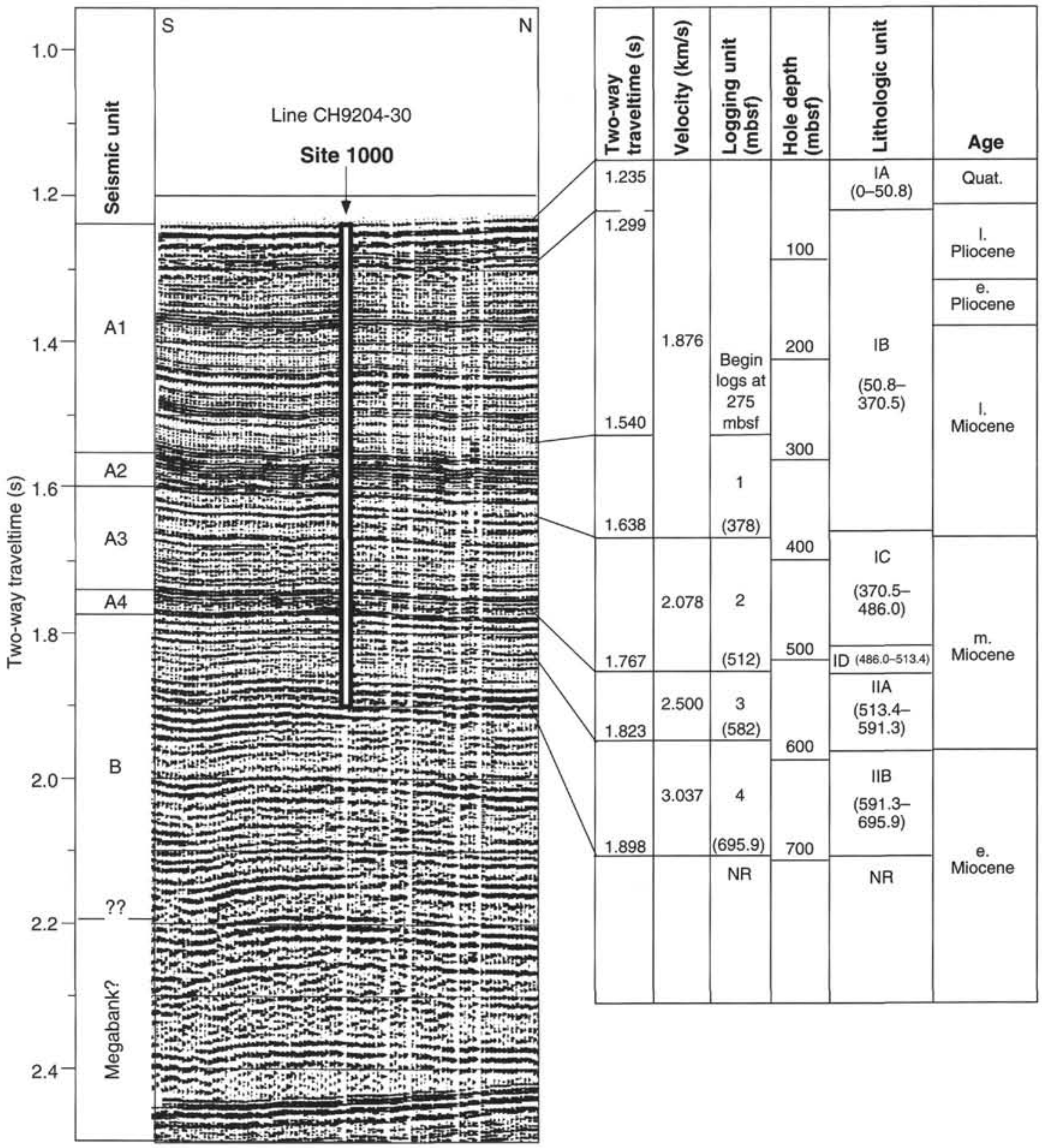

Figure 53. Summary of correlations between seismic stratigraphy, depths, logging units, lithologic units, and ages at Site 1000. Correlations with the reflection seismic record were constrained by calculations of two-way traveltime vs. depth derived from compressional velocities measured by downhole logging and laboratory instruments (see "Downhole Measurements" and "Seismic Stratigraphy" sections, this chapter). Velocities shown are averages derived from the downhole sonic tool within each major logging unit from 275 to 666 mbsf, and physical properties measurements from 0 to 275 and from 666 to 695.9 mbsf. Thus, the interval velocity from 0 to 378 mbsf and from 582 to 695.9 mbsf was derived using a combination of downhole logging and physical properties data. NR = no recovery.

SHORE-BASED LOG PROCESSING

HOLE 1000B

Bottom felt: 927.2 mbrf
Total penetration: 695.9 mbsf
Total core recovered: 142.97 m (67.6%)

Logging Runs

Logging string 1: DIT/SDT/HLDT/CNTG/NGT
Logging string 2: GHMT/NGT (2 passes)
Logging string 3: FMS/GPIT/NGT (2 passes)
Wireline heave compensator was not used due to a major system failure.

Bottom-Hole Assembly/Pipe

The following bottom-hole assembly and pipe depths are as they appear on the logs after differential depth shift (see "Depth shift" section) and depth shift to the seafloor. As such, there might be a discrepancy with the original depths given by the drillers on board. Possible reasons for depth discrepancies are ship heave and drill string and/or wireline stretch.

DIT/SDT/HLDT/CNTG/NGT: Bottom-hole assembly at ~273 mbsf
GHMT/NGT: Bottom-hole assembly at ~277 mbsf (pass 1)
GHMT/NGT: Did not reach bottom-hole assembly (pass 2)
FMS/GPIT/NGT: Did not reach bottom-hole assembly (both passes)
DIT/SDT/HLDT/CNTG/NGT: Pipe at ~165 mbsf

Processing

Depth shift: Original logs have been interactively depth shifted with reference to NGT from the DIT/SDT/HLDT/CNTG/NGT run and to the seafloor (–924 m). This value corresponds to the bottom of the seafloor as seen on the logs and is 3.2 m shallower than the "bottom felt" depth given by the drillers.

Gamma-ray processing: Data have been processed to correct for borehole size and type of drilling fluid.

Acoustic data processing: Because of the good quality of the acoustic logs, no processing has been performed.

Quality Control

The density data show a few spikes (397.5, 482.5, 563.5, 627.5, and 642 mbsf) because of instability of the long spacing detector possibly caused by borehole conditions.

Data recorded through the bottom-hole assembly, such as the neutron porosity and gamma-ray data above 273 mbsf should be used qualitatively only because of attenuation on the incoming signal.

Hole diameter was recorded by the hydraulic caliper on the HLDT tool (CALI) and the caliper on the FMS string (C1 and C2).

Details of standard shore-based processing procedures are found in the "Explanatory Notes" chapter (this volume). For further information about the logs, please contact:

Cristina Broglia
Phone: 914-365-8343
Fax: 914-365-3182
E-mail: chris@ldeo.columbia.edu

Zhiping Tu
Phone: 914-365-8336
Fax: 914-365-3182
E-mail: ztu@ldeo.columbia.edu

Hole 1000B: Natural Gamma Ray-Density-Porosity Logging Data

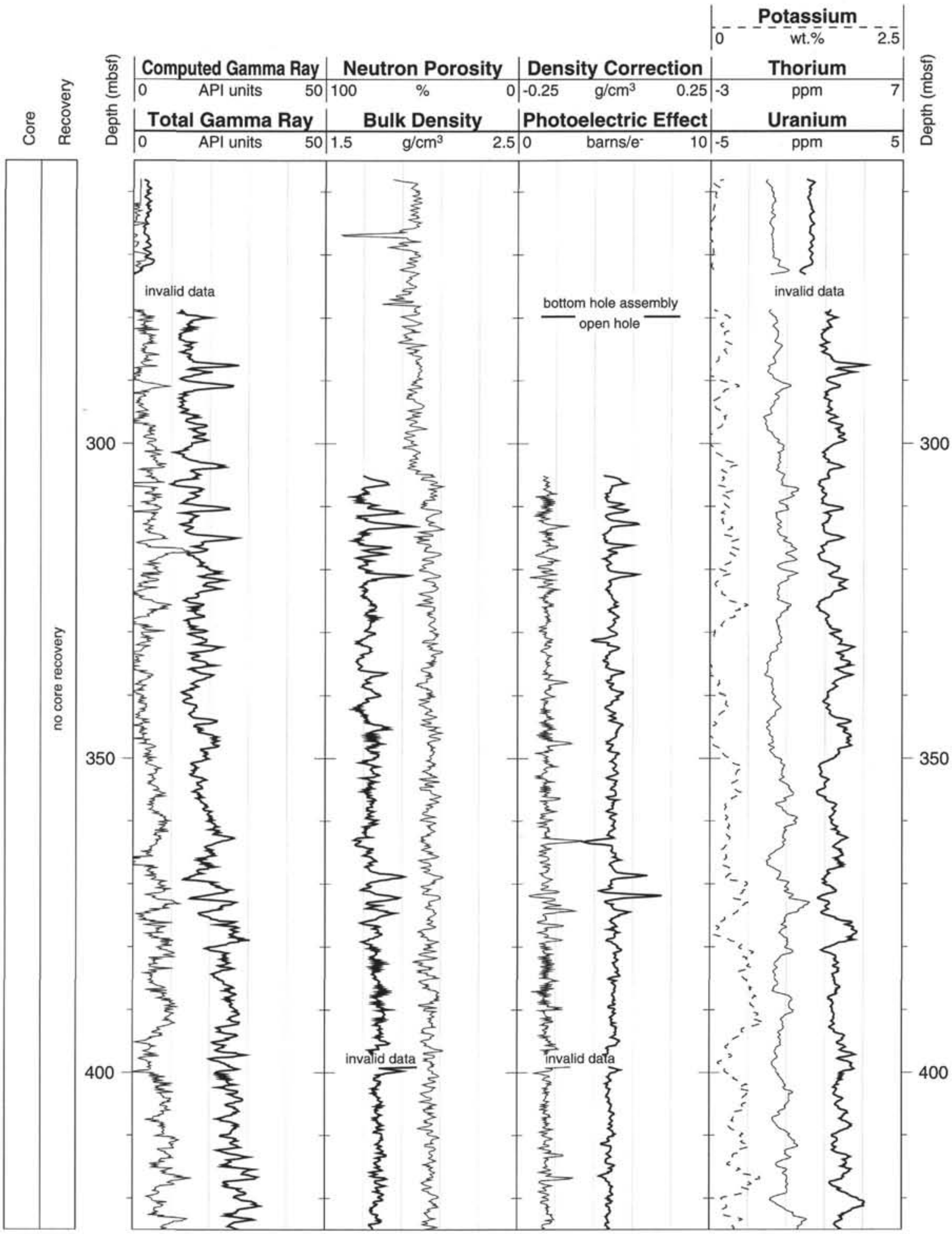

Hole 1000B: Natural Gamma Ray-Density-Porosity Logging Data (cont.)

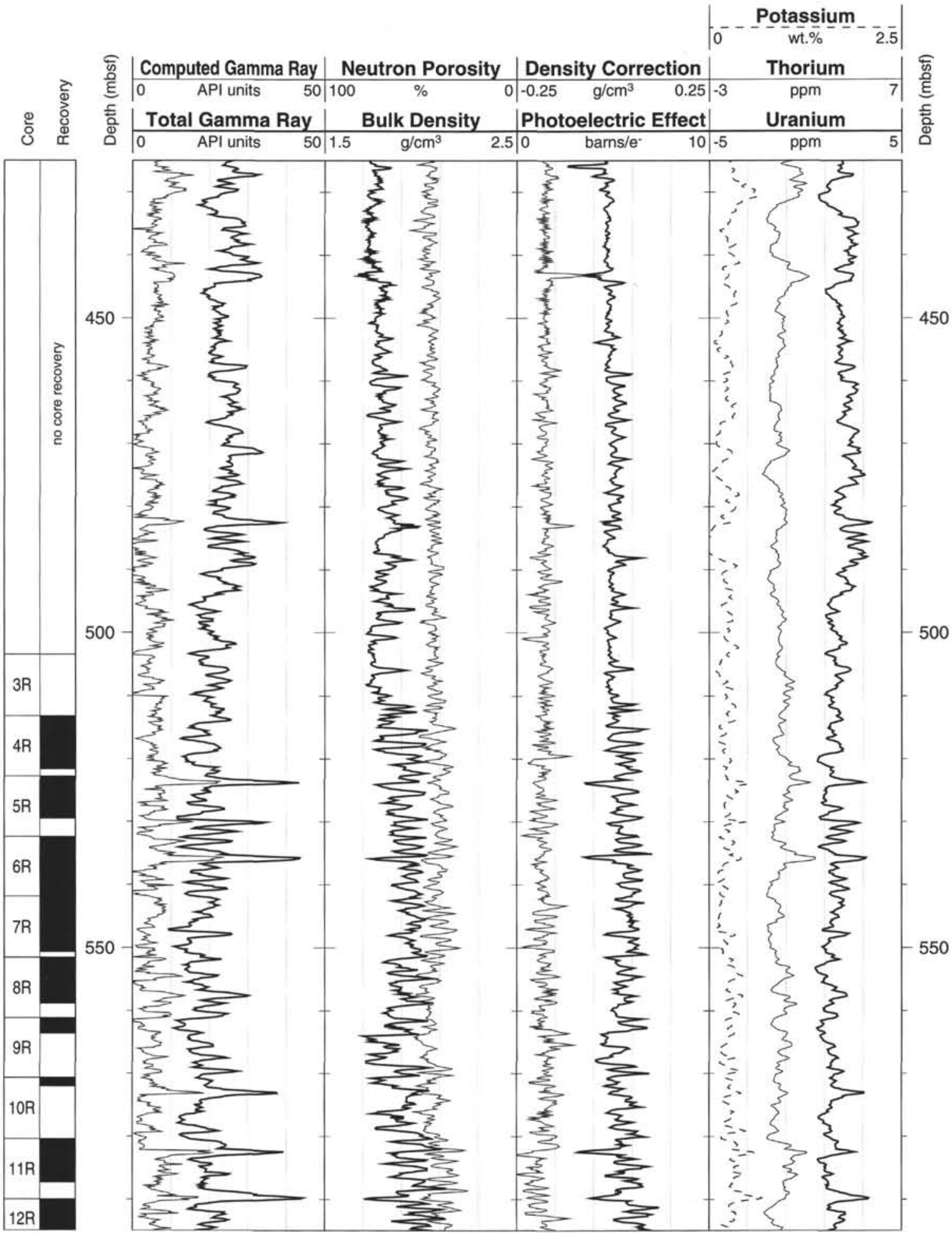

Hole 1000B: Natural Gamma Ray-Density-Porosity Logging Data (cont.)

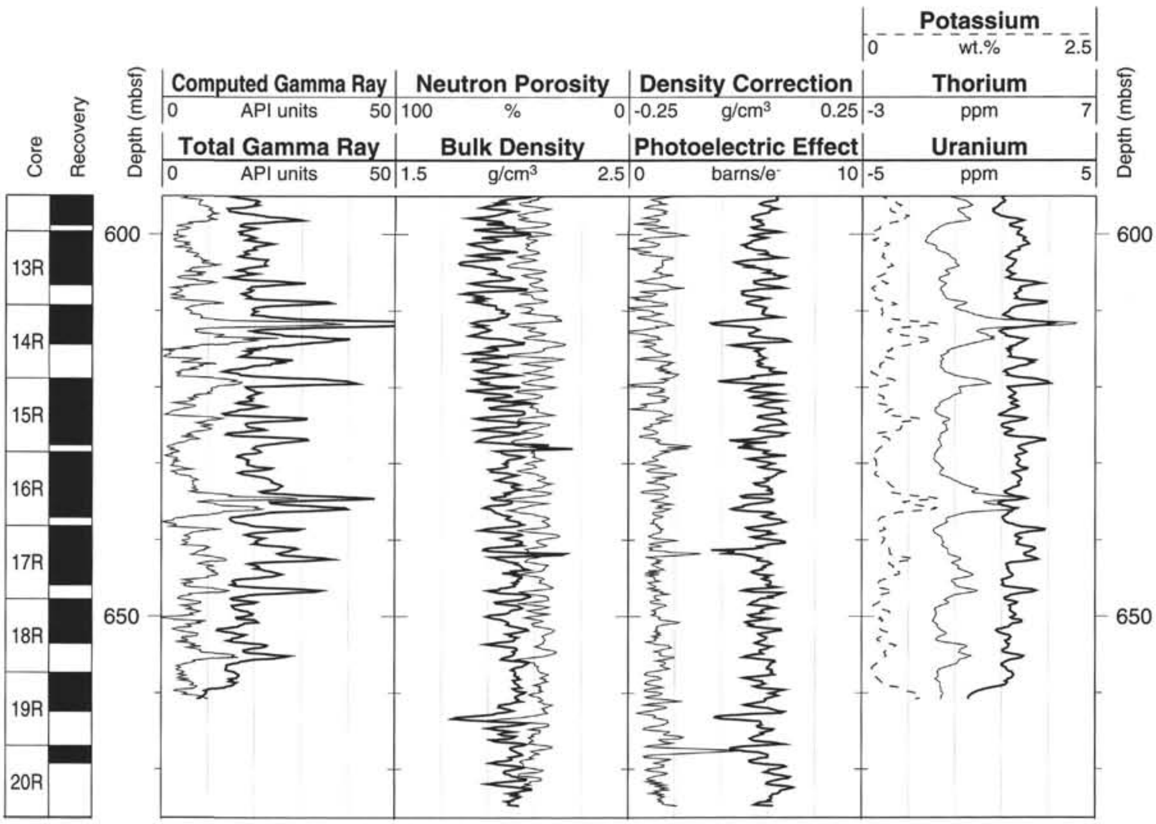

Hole 1000B: Natural Gamma Ray-Resistivity-Sonic Logging Data

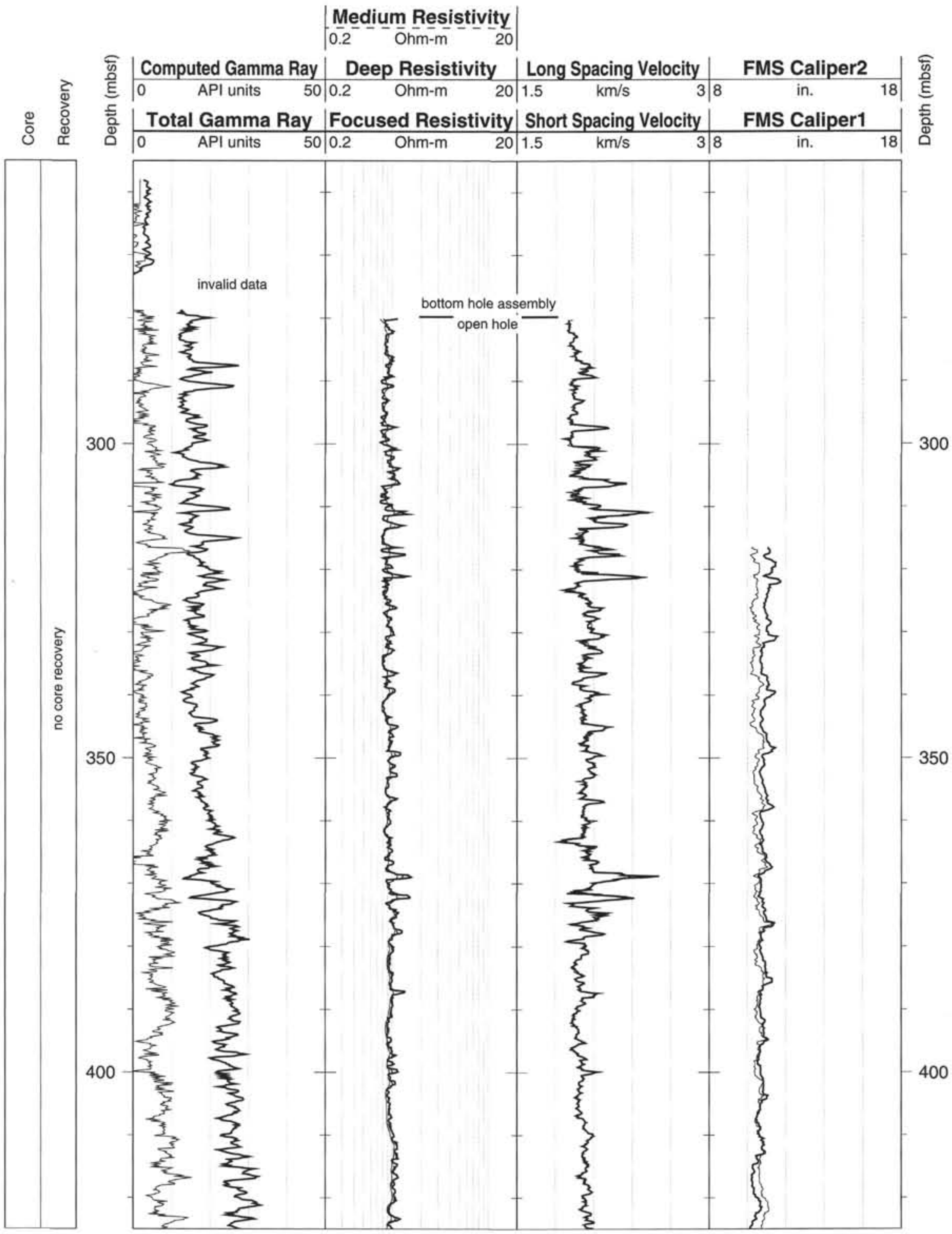

Hole 1000B: Natural Gamma Ray-Resistivity-Sonic Logging Data (cont.)

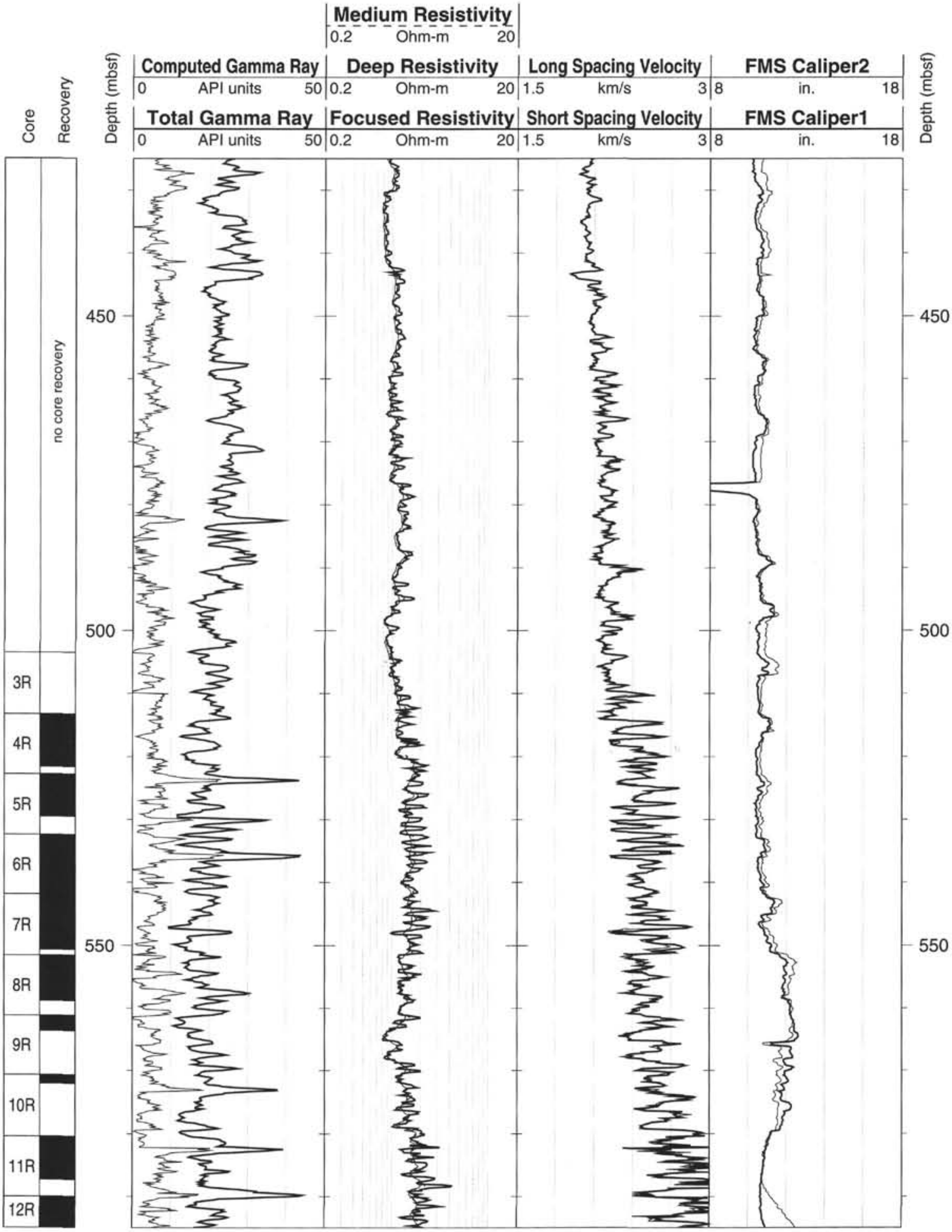

Hole 1000B: Natural Gamma Ray-Resistivity-Sonic Logging Data (cont.)